Fermilab Library
0 1160 0086037 3

The Pennsylvania State University

The Graduate School

College of Science

# HADRONIC PRODUCTION OF PIZERO PAIRS AND ASSOCIATED EVENT STRUCTURE AT 530 GEV

A Thesis in

Physics

by

Keith W. Hartman

Submitted in Partial Fulfillment
of the Requirements
for the Degree of

Doctor of Philosophy

1990

## Abstract

The production of high transverse momentum $\pi^0$ pairs and associated event structure at 530 GeV is studied. Data are presented from experiment 706 at Fermilab in Batavia, Illinois. The detector consisted of a charged particle spectrometer operating in conjunction with a large acceptance liquid argon calorimeter. The data were collected over the 1987–1988 Fermilab fixed target run using a dual, symmetric high transverse momentum electromagnetic trigger. A study of the behavior of this unique trigger and of the electromagnetic calorimeter has been made. The yield of high $p_T$ $\pi^o$ pairs in terms of the cross section $d\sigma/dM$ is found to be in good agreement with QCD predictions and with experiments at other values of $\sqrt{s}$. Detailed comparisions with QCD predictions are in excellent agreement and suggest that these events are induced by gluons in the beam hadrons. Results from the structure of charged particles produced in association with these $\pi^o$s are also discussed.

FERMILAB
LIBRARY



Thesis
Gift AAF-479a

# Contents

**List of Figures** viii

**List of Tables** xii

**Acknowledgements** xiii

**Chapter 1 QCD and High $p_T$ Phenomena** 1

1.1 High $p_T$ Hadronic Interactions . . . . . 1

1.1.1 Variables and Notation . . . . . 3

1.1.2 Early Results . . . . . 4

1.1.3 Scaling in the High $p_T$ Region . . . . . 6

1.2 Description of a QCD Monte Carlo . . . . . 14

1.2.1 The Subprocess Cross Sections . . . . . 14

1.2.2 Distribution and Fragmentation Functions Fits . . . 16

1.3 Symmetrically Triggered Events . . . . . 22

1.4 Goals of the Thesis . . . . . 23

**Chapter 2 The E706 Spectrometer** 24

2.1 Overall View . . . . . 24

2.2 The MWest Beam and Target . . . . . 29

2.2.1 The MW Beam . . . . . 30
2.2.2 The Target . . . . . 30
2.3 The Tracking System . . . . . 32
2.3.1 The Silicon Strip Detector (SSD) System . . . . . 34
2.3.2 The MW9AN Dipole Magnet . . . . . 35
2.3.3 The Proportional Wire Chamber (PWC) System . . 38
2.3.4 The Nanometrics Readout System . . . . . 56
2.4 The Liquid Argon Calorimeter . . . . . 58
2.4.1 The Electromagnetic Section . . . . . 58
2.4.2 The Hadronic Section . . . . . 61
2.5 The Forward Calorimeter . . . . . 62

**Chapter 3 Event Reconstruction** **63**
3.1 Data Acquisition . . . . . 63
3.1.1 Front Ends . . . . . 64
3.1.2 VAXONLINE . . . . . 64
3.2 First Pass Analysis . . . . . 66
3.2.1 MAGIC and Event Reconstruction . . . . . 66
3.2.2 Tracking . . . . . 67
3.2.3 PLREC Efficiency . . . . . 74
3.2.4 Electromagnetic Showers . . . . . 76
3.3 General Trigger Considerations . . . . . 77
3.3.1 Beam Determination . . . . . 79
3.3.2 Pre-Trigger . . . . . 83

3.3.3 Data Compression . . . . . 85

3.4 The TWO GAMMA Trigger . . . . . 86

3.4.1 Performance . . . . . 88

3.4.2 Efficiency . . . . . 88

3.4.3 Two-Gamma Trigger Acceptance Issues . . . . . 94

3.4.4 Selection of Single $\pi^o$s . . . . . 101

**Chapter 4 Electrons** **106**

4.1 Photon Conversions . . . . . 106

4.2 Definition of a Zero Mass Pair . . . . . 107

4.3 Properties of the ZMP Electrons . . . . . 115

4.4 E/P Studies . . . . . 122

4.4.1 E/P Distributions . . . . . 122

4.4.2 E/P vs P . . . . . 132

4.5 EMLAC Efficiency . . . . . 137

**Chapter 5 Analysis of the $\pi^o$ Pair Events** **140**

5.1 General Features of the $\pi^o$ Pair Events . . . . . 141

5.2 Event Structure . . . . . 145

5.2.1 Azimuthal Correlations . . . . . 147

5.2.2 Rapidity Correlations . . . . . 149

5.2.3 Y-$\phi$ Definition of Jets . . . . . 152

5.2.4 Charged Particle Multiplicity in the Jets . . . . . 156

5.3 $\pi^o$ Pairs . . . . . 159

5.3.1 Selection of $\pi^o$ Pair Events . . . . . 159

5.3.2 Background Subtraction . . . . . 159

5.3.3 Distributions in $\cos\theta^*$ . . . . . 161

5.3.4 Definition of the Cross Section . . . . . 161

5.3.5 Corrections to the Data . . . . . 166

5.3.6 $\pi^\circ\pi^\circ$ Mass Spectra . . . . . 168

5.3.7 Beam Ratio . . . . . 174

5.4 Conclusions . . . . . 183

**References and Notes** **188**

## List of Figures


1.1 $\langle p_T \rangle$ vs CM Energy in Hadronic Interactions . . . . . 2

1.2 ISR Single $\pi^\circ$ $p_T$ Spectrum . . . . . 5

1.3 Schematic Representation of Hadronic Interaction . . . . . 8

1.4 Evolution of the Gluon Density in a Proton . . . . . 13

1.5 Gluon Density in the Nucleon and Pion . . . . . 18

1.6 Valence Quark Density in the Nucleon and Pion . . . . . 20

1.7 Sea Quark Density in the Nucleon and Pion . . . . . 21

2.1 Plan View of the E706 Spectrometer . . . . . 26

2.2 Plan View of the SSD and Target Region . . . . . 27

2.3 Longitudinal (Z) Vertex Distribution . . . . . 37

2.4 Cathode-Anode Arrangement within a PWC Module. . . . . 40

2.5 Sample Wire Chamber Plateau Curve . . . . . 54

2.6 Perspective View of the EMLAC . . . . . 60

3.1 $\chi^2$ Per Degree Of Freedom for PWC Space Tracks . . . . . 69

3.2 Number of Points Used in PWC Space Tracks . . . . . 70

3.3 $\pi^+\pi^-$, $p\pi^-$ and $\bar{p}\pi^+$ Mass Distributions . . . . . 72

3.4 $\pi^\circ$s and $\eta$'s from Photon Conversions. . . . . 73

3.5 $e^+e^-$ Mass Distribution . . . . . 75

3.6 Allowable Orientation of the Two-Gamma Trigger . . . . . 87

3.7 Octant Activity in the Two-Gamma Trigger. . . . . 90

3.8 Octant (1–4) Frequency in the Two-Gamma Trigger. . . . . 91

3.9 Octant (5–8) Frequency in the Two-Gamma Trigger. . . . . 92

3.10 Fits to Uncorrected $p_T$ Spectra for Single $\pi^o$s. . . . . 96

3.11 Example of Two-Gamma Efficiency Curves . . . . . 99

3.12 $\gamma\gamma$ Effective Mass . . . . . 103

3.13 Two-Photon Asymmetry Distributions . . . . . 105

4.1 $\Delta X$, $\Delta Y$ and $\Delta R^2$ Distributions . . . . . 109

4.2 Z-X Intersection . . . . . 111

4.3 $\Delta S_Y$ Distributions . . . . . 112

4.4 $ZXI$ and $\Delta S_Y$ vs Momentum . . . . . 114

4.5 Momentum and Position Dependence of Track-Shower Matching . . . . . 116

4.6 Momentum and Energy Spectra of Electrons . . . . . 118

4.7 Position of ZMP Electrons at EMLAC . . . . . 119

4.8 $E_F/E$ Distributions . . . . . 121

4.9 Photon Asymmetry Distributions . . . . . 123

4.10 E/P for ZMP Electrons in the range: $P = 18 \pm 1GeV$. . . . 126

4.11 E/P for $9 \leq P \leq 11$ GeV . . . . . 129

4.12 E/P for $22.5 \leq P \leq 27.5$ GeV . . . . . 130

4.13 E/P for $60 \leq E \leq 70$ GeV . . . . . 131

4.14 E/P vs P . . . . . 134

4.15 E/P vs E . . . . . 136

4.16 E/P vs 1/P . . . . . 138

4.17 EMLAC Efficiency vs Momentum . . . . . 139

5.1 Raw Mass, $p_T$ and Rapidity Distributions for Observed $\pi^o$ Pair Events. . . . . 144

5.2 Raw $\cos\theta^*$ Distributions. . . . . 145

5.3 $\pi^o$ Pair Event and Associated Particles. . . . . 146

5.4 Azimuthal Correlations. . . . . 148

5.5 Rapidity Distributions for $\pi^o$s and Associated Particles. . . . 150

5.6 Rapidity Difference Correlations. . . . . 153

5.7 Rapidity Correlations. . . . . 154

5.8 $\langle Z(\pi^o)\rangle$ vs $p_T$ and $x_T$ . . . . . 157

5.9 $\langle n_{CH}\rangle$ vs $p_T(\pi^o)$. . . . . 158

5.10 $\gamma\gamma$ Mass Plots for the *Opposite* Octant of the TWO-GAMMA Trigger . . . . . 162

5.11 $\cos\theta^*$ Normalized to $\theta^* = 90^o$ . . . . . 163

5.12 QCD $\cos\theta^*$ in Expanded $\pi^o$ Rapidity Range. . . . . 164

5.13 $\pi^o$ Pair Mass from the Negative Beam . . . . . 169

5.14 $\pi^o$ Pair Mass from the Positive Beam . . . . . 170

5.15 ISR and E706 $\pi^o\pi^o$ Mass Spectra . . . . . 172

5.16 QCD Predictions for ISR and E706 Mass Spectra . . . . . 173

5.17 $\pi^o$ Pair Scaled Mass . . . . . 175

5.18 QCD Scaled Mass Spectra at ISR and E706 Energies . . . . 176

5.19 Cross Section Beam Ratio . . . . . 178

5.20 Beam $x$ vs Mass . . . . . 181

5.21 Beam $x$-Distributions . . . . . 182

5.22 Distribution Function Ratios . . . . . 184

5.23 Beam $x$-Distribution Ratio . . . . . 185

## List of Tables


1.1 Parton-Parton Two Body Cross Sections. . . . . 15

2.1 Breakdown of Spectrometer Channels . . . . . 25

2.2 Beam Content . . . . . 31

2.3 E706 Target Materials . . . . . 33

2.4 SSD Wafer Parameters . . . . . 36

2.5 Regions of Cathode Segmentation in PWC Modules . . . . . 42

2.6 PWC Anode Parameters . . . . . 43

2.7 PWC Cathode Garland Locations . . . . . 47

3.1 Possible Two-Gamma Trigger Combinations . . . . . 86

3.2 Run Statistics . . . . . 89

3.3 Fit Parameters to Azimuthally Averaged $\pi^\circ$ $p_T$ Spectra . . . 95

3.4 Fit Parameters to Single $\pi^\circ$ $p_T$ Spectra for Octants 1–4. . . . 97

3.5 Fit Parameters to Single $\pi^\circ$ $p_T$ Spectra for Octants 5–8. . . . 98

4.1 Number of ZMPs . . . . . 124

5.1 Number of Raw $\pi^\circ$ Pairs Distributed in Mass . . . . . 142

5.2 Number of Raw $\pi^\circ$ Pairs Distributed in $p_T$ . . . . . 143

5.3 Beam Ratio Fit Parameters . . . . . 177

## Acknowledgements

On the scale of things in general, this is a rather insignificant document. On a more personal level, it is somewhat more than that. Due to its rather chaotic, circuitous course many people have influenced me in the pursuit of this thesis, whether or not they were (or I was) aware of it. I wish to take this opportunity to thank some of them here.

First and foremost, I wish to thank my parents, Raymond and Esther Hartman, for encouraging me to do whatever caught my fancy – even if that meant going to college. Although I am not terribly good at science, I am very interested in it. I'd like to thank my brothers, Bruce and Craig, and my sister, Edie, for putting up with my often times excessive excitement.

My old high-school friend, Billy Goyette, I'd like to thank for showing me how far it is to the sun in units of book page thicknesses. Buick Motor Division and the United Auto Workers Union both deserve equal blame for pushing me back into college, although I occasionally miss punching a time-clock.

I would like to thank my undergraduate physics professor, Don Boys, for continually encouraging me to go to grad school. Thanks go to John Scofield for convincing me not only that I could go, but that I should go.

And also, thanks, John, for embarrassing me into the realization that there are things more important in life than bugs; otherwise I may have turned into an entomologist. Also, I am sorry that I was such a jerk in high school.

Many thanks go to John Miller of Argonne for his unending support and encouragement in my pursuit of an academic post-undergraduate life. I apologize for that unfortunate early morning house-sitting incident with your neighbors. And thanks, John, for not succeeding in turning me into a chemist, although I very much enjoyed glass-blowing and the table-top experiments.

Many thanks go to Jeri Ann Zitek, secretary of our high energy physics group, for all the running around she has done for me while I was at Fermilab. She was truly instrumental in circumventing the far too numerous bureaucratic obstacles placed in the path of a Penn State grad student. Our all-things mechanical and all-things electrical know-it-all, John Passeneau, was vital to the construction of our wire chambers. Thanks, John, for teaching me that these things were simple machines and that we could build them (although making them work was another story).

My advisor, Jim Whitmore, has been nothing less than inspiring. Although he may now question his decision to let me do whatever I wanted, it is for this that I thank him the most. He has provided many ideas for lines of analysis and nudged me in a few specific directions – every one of which has been worthwhile in one way or another. I would also like to thank him for understanding why my productivity decreased during the NBA playoffs over recent years.

Thanks go to George Ginther, the conscience of our experiment, for doing so much of the dirty work (and for the endless supply of frozen Oreos). Thanks go to Carl Bromberg for introducing me to the $J/\psi$ and a host of other things just within or just beyond the capabilities of our spectrometer (it would be too easy to have thanked Carl for our lively weekly meetings). I would like to thank our illustrious leader, Paul Slattery, for keeping the peace, on a weekly basis, between the various special interests which inevitably arise in any such large collection of people who think they are smarter than everybody else. Thank you Rob Roser, for taking my wife to that Pistons-Bulls playoff game while I was back in Pennsylvania defending this work.

Thanks to Joey Huston for taking an initial interest in the physics of $\pi^0$ pairs and for many early suggestions on the analysis. I also owe Joey a great debt for acting the middleman in acquiring Jeff Owens' QCD Monte Carlo code. And thanks to Jeff Owens for allowing this unknown person to abuse his work in the following pages. Thanks to Marek Zielinski for his very keen, persistent interest in electrons and for helping me with some of the conceptual aspects of my analysis. I promise that we will get to the bottom of those pesky ZMPs.

Thanks to Armando Lanaro for the honor of presiding over one of his wedding ceremonies, not that he had any choice. And, Armando, thanks for the years of warm friendship; in spirit, if not in deed, the *Scusi* deal in still on.

Thanks to Sudhindra Mani for the many late-night discussions, some

trailing off into the Village air well after the Users' Center closed. Thanks for trying to keep our tracking meetings at a respectable level, despite my pointer-breaking outburst at our ability to expand any topic into a three hour ordeal. Thanks also for the cowboy boots, and for being a great friend.

I save my most heartfelt thanks for my wife, Robin McCloskey. She has taught me that there are things more important in life than physics – like basketball. Thanks, Robin, for helping me through every single aspect of this project and for turning me into something of an armchair art-critic. Most of all, thank you for adding an entirely new layer of richness to my life.

This thesis is dedicated to the

memory of my mother,

Esther Irene Pieper Hartman

1926 – 1985

# Chapter 1

# QCD and High $p_T$ Phenomena

In this chapter we will present a brief history of high $p_T$ hadronic phenomena beginning with a short discussion of low $p_T$ particle production. Following a short interlude on notation, we will present the basic features of high $p_T$ single particle production from the perspective of quantum chromodynamics (QCD). We will discuss the confrontation of the initial theoretical expectations with early experimental results and how theory has evolved to accommodate the experiments. Within this context, we will discuss the contribution symmetric di-hadron studies may expect to provide.

## 1.1 High $p_T$ Hadronic Interactions

The average transverse momentum, $\langle p_T \rangle$, of particles produced in hadronic interactions is largely independent of collision energy with a value of $\langle p_T \rangle \sim$ 350 MeV[1] across a range of center of mass energies from $\sqrt{s} \simeq 5$ GeV to

[1]Throughout this thesis we will use a "natural" system of units which are somewhat more convenient than the standard MKS system. In this system, energy, mass and momentum will be given in units of GeV, unless otherwise indicated. In these units it is

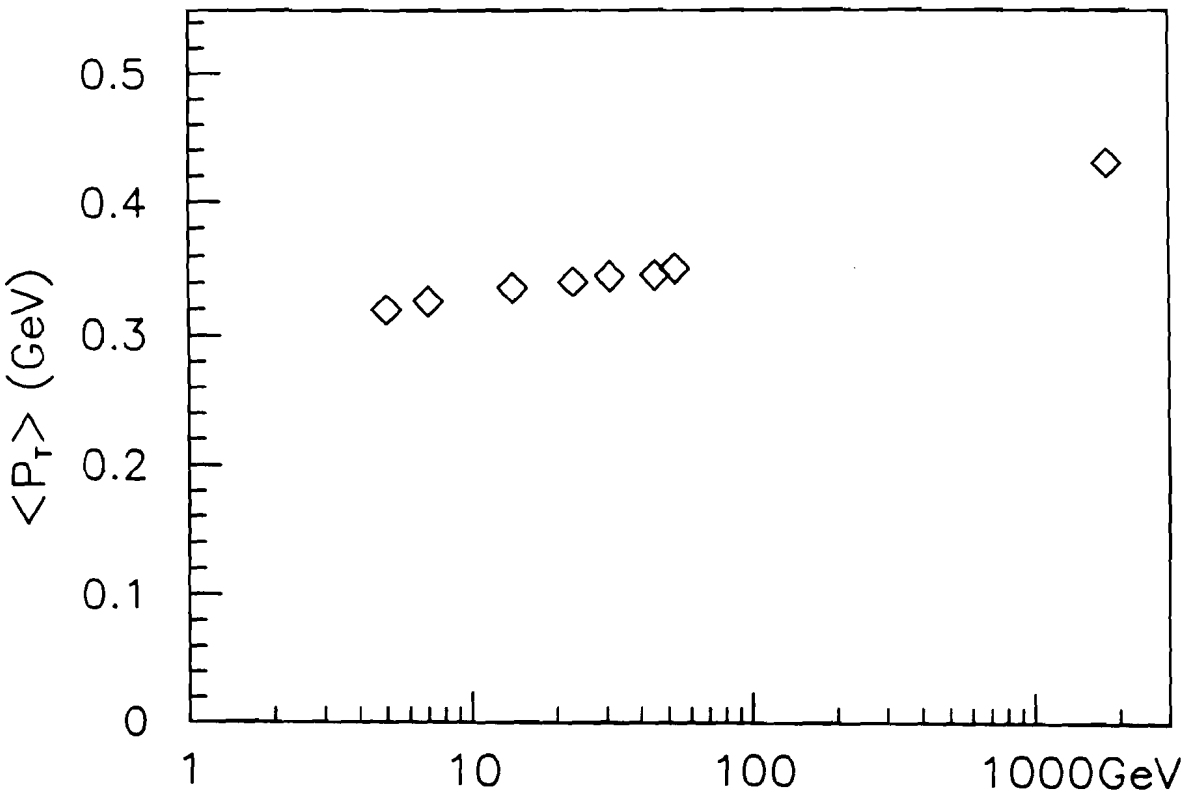


Figure 1.1: $\langle p_T \rangle$ vs CM Energy in Hadronic Interactions. These data were compiled from Rossi [38] and the CDF Collaboration [1].

$\sqrt{s} \simeq 1800$ GeV (see Figure 1.1). Note that the scale of the abscissa is *logarithmic*.

It is rather remarkable that this quantity remains nearly constant over such a large range of energy. This has been studied by a number of workers in terms of a hydrodynamical model [14] with the primary result being that

entirely unnecessary to write mass units in the cumbersome form $GeV/c^2$ and momentum units as $GeV/c$; the $c$'s will be implicit yet obvious from the context of their usage.

the $p_T$ spectrum is expected to fall exponentially with $p_T$. It is precisely this exponential behavior which is experimentally observed for the low $p_T$ particles [18]. This follows from the assumption that the scale of the interaction is determined by the size of hadrons. The proton size is $\sim$ 1 fm ($=10^{-15}$m) which corresponds to $\sim$ 200 MeV via the uncertainty principle.

In contrast to the mean $p_T$ with which most particles in high energy interactions are produced, the $\pi^0$s we will study in this thesis start with a $p_T \sim$ 2 GeV and extend up to about 7 or 8 GeV. Before we talk about these high $p_T$ particles, we must lay the notational groundwork which has evolved as the standard description of high $p_T$ phenomena.

### 1.1.1 Variables and Notation

For the study of a scattering process of the type

$$A + B \rightarrow h_1 + h_2 + X \tag{1.1}$$

where $A$ and $B$ are initial state hadrons and $h_1$ and $h_2$ are detected final state particles and $X$ corresponds to anything else,[2] a set of conventional variables has evolved. The hadronic initial and final state particles will be referred to by upper case letters while the underlying subprocess will be indicated by lower case letters:

$$a + b \rightarrow c + d. \tag{1.2}$$

[2] For the case of single particle production, $h_2$ would be contained in $X$.

We may write the Lorentz invariant Mandelstam variables for either Equation 1.1 or Equation 1.2:

$$s = (p_A - p_B)^2, \quad t = (p_A - p_C)^2, \quad u = (p_A - p_D)^2$$

$$\hat{s} = (p_a + p_b)^2, \quad \hat{t} = (p_a - p_c)^2, \quad \hat{u} = (p_a - p_d)^2$$

where the hat over the letter indicates the subprocess variable. The $p_I$ and the $p_i$ are the four vectors for the hadrons and partons, respectively. The Mandelstam variables are not independent since

$$\hat{s} + \hat{t} + \hat{u} = \sum_{i=a,b,c,d} m_i^2.$$

### 1.1.2 Early Results

In the middle to late seventies, experiments began to explore the higher $p_T$ region of single $\pi^0$ production. Not only were the $p_T$ spectra for $\pi^0$s with $p_T \geq 1$ GeV found to deviate from the exponential behavior; there was also an energy dependence of the rate of production as a function of $p_T$, see Figure 1.2.

This was direct indication that something new was happening. At the time, it was correctly believed that the deviation from exponential behavior was evidence for internal hadronic structure. In particular, the experiments were observing the scattering process between the constituents of the nucleons, i.e., parton-parton scattering. Although this is still the primary interpretation given to these results, it has become somewhat more sophisticated over the past ten years.

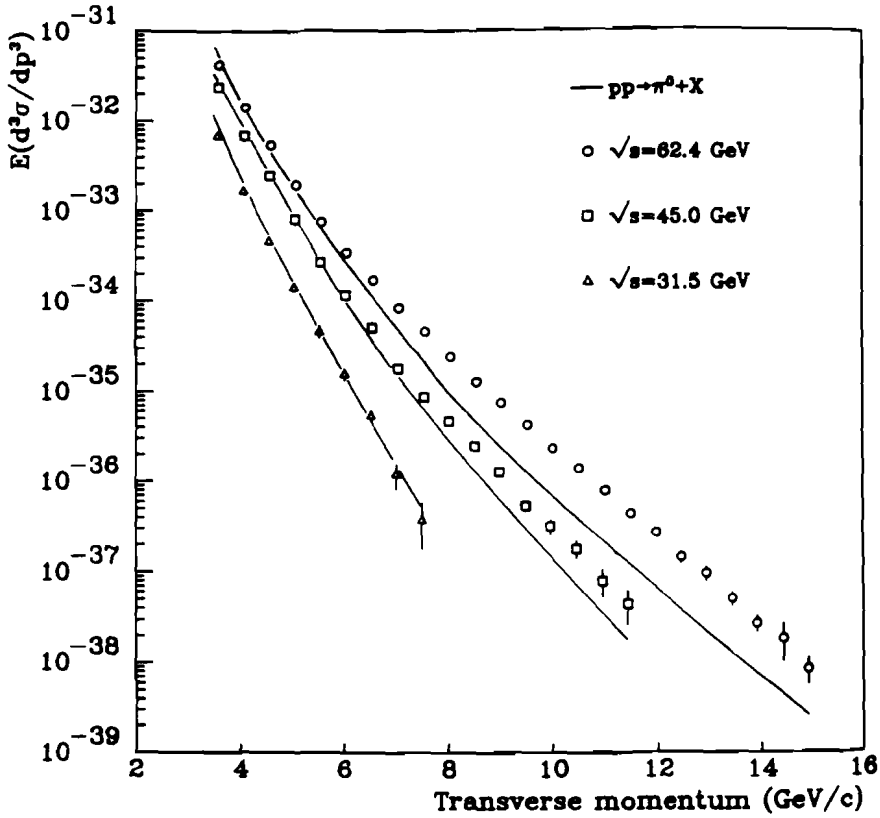


Figure 1.2: ISR Single $\pi^0$ $p_T$ Spectrum. This plot was first published by the CCOR Collaboration [4].

The theory which is most frequently called upon to describe these high $p_T$ (short distance) hadronic interactions is referred to as quantum chromodynamics (QCD). This field theory views the collisions between hadrons in terms of the interactions between the hadronic constituents – quarks and gluons (generically referred to as partons). We will discuss briefly the highlights of QCD and its implications for high $p_T$ particle production in the following sections and refer the reader to the more complete recent review of Owens ([33]).

### 1.1.3 Scaling in the High $p_T$ Region

The standard description of high $p_T$ hadronic interactions is represented schematically in Figure 1.3. It is evident from this diagram that the entire interaction, $A + B \rightarrow h_1 + h_2 + X$ may be partitioned into three distinct processes:

- The parton structure functions, $G_{a/A}(x_a)$ and $G_{b/B}(x_b)$, correspond to the distribution of a hadron's momentum amongst its constituent partons. For example, $G_{a/A}(x_a)$ is the probability that parton $a$ in hadron $A$ has a fraction $x_a$ of the momentum of $A$ (i.e. $x_a = p_a/p_A$). For the analysis in this thesis, particle A will correspond to the beam hadron and B the target hadron.

- The constituent subprocess

$$\frac{d\hat{\sigma}}{d\hat{t}}(a + b \rightarrow c + d) \tag{1.3}$$

contains the QCD scattering amplitudes for, ideally, all allowed parton-parton interactions.

- The fragmentation functions, $D_{h1/c}(z_c)$ and $D_{h2/d}(z_d)$, symbolize the distribution of a scattered parton's momentum amongst its resultant, materialized hadrons. To further illustrate, $D_{h/c}(z_c)$ is the probability that parton $c$ fragments into hadron $h$ carrying a fraction, $z_c$, of the parent parton's momentum. In this thesis, we will study interactions in which $\pi^o$s have emerged from each fragmentating parton carrying most of the parton momentum.

The cross section for the process under consideration is then calculated by summing up the contributions from all the lowest order diagrams (corresponding to all *two-body* constituent scattering subprocesses) weighted by the parton distribution and fragmentation functions. This prescription outlines the standard parton model. The distribution and fragmentation functions must be determined by experiment; they are not calculable using perturbation theory.

Implicit in the definition of the distribution and fragmentation functions above is a lowest order perturbation calculation. This is indicated by their scale-invariance; they do not depend on the scale of the interaction. To carry the calculation to higher orders, more complicated diagrams must be considered. When these higher order sub-processes are included, a variety of singularities arise which must be regulated by some consistent technique. The incoming and outgoing partons, when subject to radiative corrections

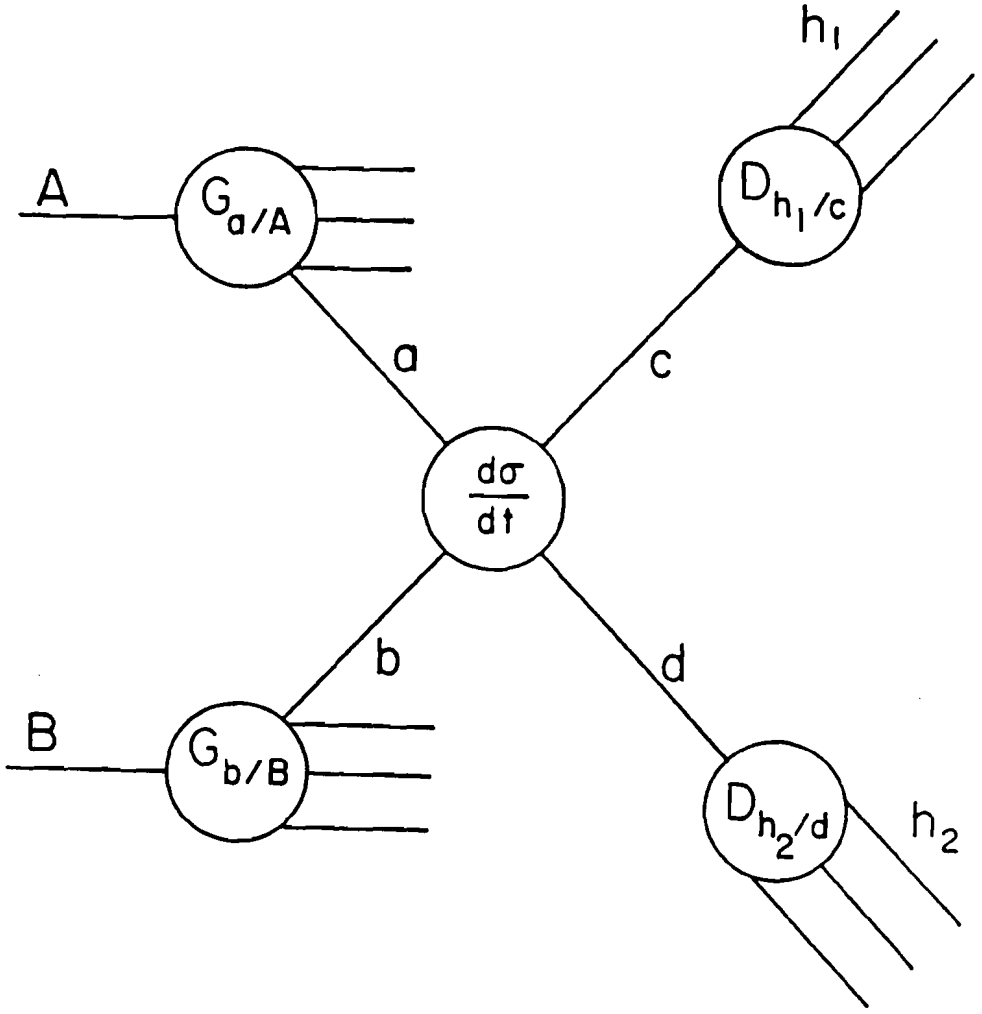


Figure 1.3: Schematic Representation of Hadronic Interaction.

(i.e., gluon emission), give rise to momentum dependent distribution and fragmentation functions. This is the source of scaling violation.

Once the distribution and fragmentation functions have been determined experimentally at some reference scale, they may be determined at other scales using the Altarelli-Parisi equation [2]. QCD predicts the breakdown of scaling and allows us to determine the explicit dependence of the these functions on the scale of the interaction.

Backing up to the simple parton model where the distribution and fragmentation functions are assumed to be scale-invariant, all observed scaling would then arise from the constituent subprocess. Any energy dependence observed in high $p_T$ particle production would directly reflect the energy dependence of the parton-parton interaction described by $d\hat{\sigma}/d\hat{t}$. Using this framework, the leading order contributions to single particle high $p_T$ particle production were calculated (see [33]) for the constituent subprocess reactions. The general form expected for the invariant single particle cross section for $A + B \rightarrow h + X$ is

$$\frac{Ed^3\sigma}{dp^3} = p_{\mathrm{T}}^n F(x_{\mathrm{T}}, \theta) \tag{1.4}$$

where $x_{\mathrm{T}} = 2p_T/\sqrt{s}$ is the transverse momentum scaled[3] by the center of mass energy $\sqrt{s}$; $\theta$ is the scattering angle measured relative to the beam direction. Since both $x_{\mathrm{T}}$ and $\theta$ are dimensionless, $F(x_{\mathrm{T}}, \theta)$ is also dimensionless and all other dimensional components are contained in the $p_T$ term.

[3] My apologies for using another definition of the word *scale*.

Since all the subprocess expressions have $1/\hat{s}^2$ terms multiplied by dimensionless components, one expects n = −4. Experimentally, this is not observed; in fact, for $p_T \geq$ 1–2 GeV, n $\simeq$ −8. Deviations from this simple behavior indicate scaling violations brought about by the higher-order processes mentioned above.

#### 1.1.3.1 The QCD Coupling Constant

The effective strong interaction coupling constant, $\alpha_S$, decreases with $Q^2$ where $Q$ is some characteristic momentum of the interaction under consideration. In the QCD leading log approximation[4], the strong coupling constant has the form

$$\alpha_S(Q^2) = \frac{\alpha_S(\mu^2)}{1 + (\alpha_S(\mu^2)/12\pi)(11n - 2f)ln(Q^2/\mu^2)} \tag{1.5}$$

where n = number of colors, f = number of quarks with mass less than the reference energy scale $\mu$ at which the perturbative expansion is calculated (it is a relic of the renormalization process). This expression for $\alpha_S$ is the first term of a series solution of a differential equation which when integrated gives rise to a constant of the integration, $\Lambda$. As such, $\Lambda$ is completely arbitrary and it is the single fundamental constant of QCD which must be determined by experiment. The convention is to define it as:

[4]The hard scattering subprocesses are calculated using perturbation theory and the term "leading log" refers to the lowest order calculation. Higher order calculations are referred to as either "next to leading order" or "next to leading log" calculations.

$$ln(\Lambda^2) = ln(\mu^2) - \frac{12\pi}{(11n - 2f)\alpha_S(\mu^2)} \tag{1.6}$$

which simplifies the expression for $\alpha_S$:

$$\begin{aligned} \alpha_S(Q^2) &= \frac{12\pi}{(11n - 2f)ln(Q^2/\Lambda^2)} \\ &= \frac{12\pi}{25\ ln(Q^2/\Lambda^2)} \end{aligned} \tag{1.7}$$

where we have made the substitutions: $n = 3$ and $f = 4$. Although at our $\sqrt{s} = 32$ GeV, we are kinematically above the bottom quark threshold, the vast majority of our data are not, hence $f = 4$. Embodied in the form of Equation 1.7 is the well-known effect of the strong interaction in which the coupling decreases with increasing $Q^2$; at short distances, the strong force becomes weaker. This is in contrast to the analogous coupling constant used in quantum electrodynamics where the effective coupling increases with $Q^2$.

#### 1.1.3.2 Distribution and Fragmentation Functions

Previously, it was mentioned that the structure[5] function, $G_{a/A}(x_a)$, is the probability that parton $a$ in hadron $A$ has a fraction, $x_a$, of hadron $A$'s momentum and that these functions actually depend on the $Q^2$ of the interaction. As previously mentioned, it is not yet possible to calculate the structure functions entirely on theoretical grounds, although it is possible to

[5]Since *distribution* and *structure* functions refer to the same thing we will use these terms interchangeably. Although we will not use it here, the term *dressing* function is occasionally used in the literature as a synonym of *fragmentation* function.

determine their $Q^2$ evolution [2] once they have been obtained experimentally at some reference $Q_0^2$. The change in the gluon density at two different values of $Q^2$ is shown in Figure 1.4. Figure 1.4a displays the change in gluon density as a function of X, the fraction of the protons's momentum carried by the gluon at a $Q^2$ of 4 $GeV^2$. Figure 1.4b is the same distribution evolved to $Q^2 = 1000\ GeV^2$ using the Altarelli-Parisi equation. Set 1 (solid line) and Set 2 (dashed line) refer to fits of the gluon density distributions made by Duke and Owens [15] in which Set 1 corresponds to $\Lambda$=200 MeV and $\Lambda$=400 MeV for Set 2. We will discuss this more fully in Section 1.2. It is apparent from this figure that a softer (harder) gluon distribution results from a smaller (larger) value of $\Lambda$ and that lower $Q^2$ experiments are sensitive to the parameter $\Lambda$ in Equation 1.7.

#### 1.1.3.3 Intrinsic Parton Momentum

Since the partons within a hadron are confined to a region of space roughly the size of the hadron ($\simeq$ 0.5 fm), they have a momentum spread $\Delta k \simeq h/2\pi \times 0.5\text{fm} \simeq 400$ MeV. Often referred to as $k_T$ smearing, this intrinsic momentum may contribute to a parton's transverse momentum. This $k_T$ smearing is rather directly observable in double prompt photon production where the mean parton $k_T$ has been measured [11] to be $\langle k_T \rangle \simeq 950$ MeV.

It would be possible to measure the intrinsic $k_T$ in the $\pi^0$ pair system with the understanding that the result will be smeared by the misalignment of the outgoing $\pi^0$ relative to the fragmenting parton. For this reason, the

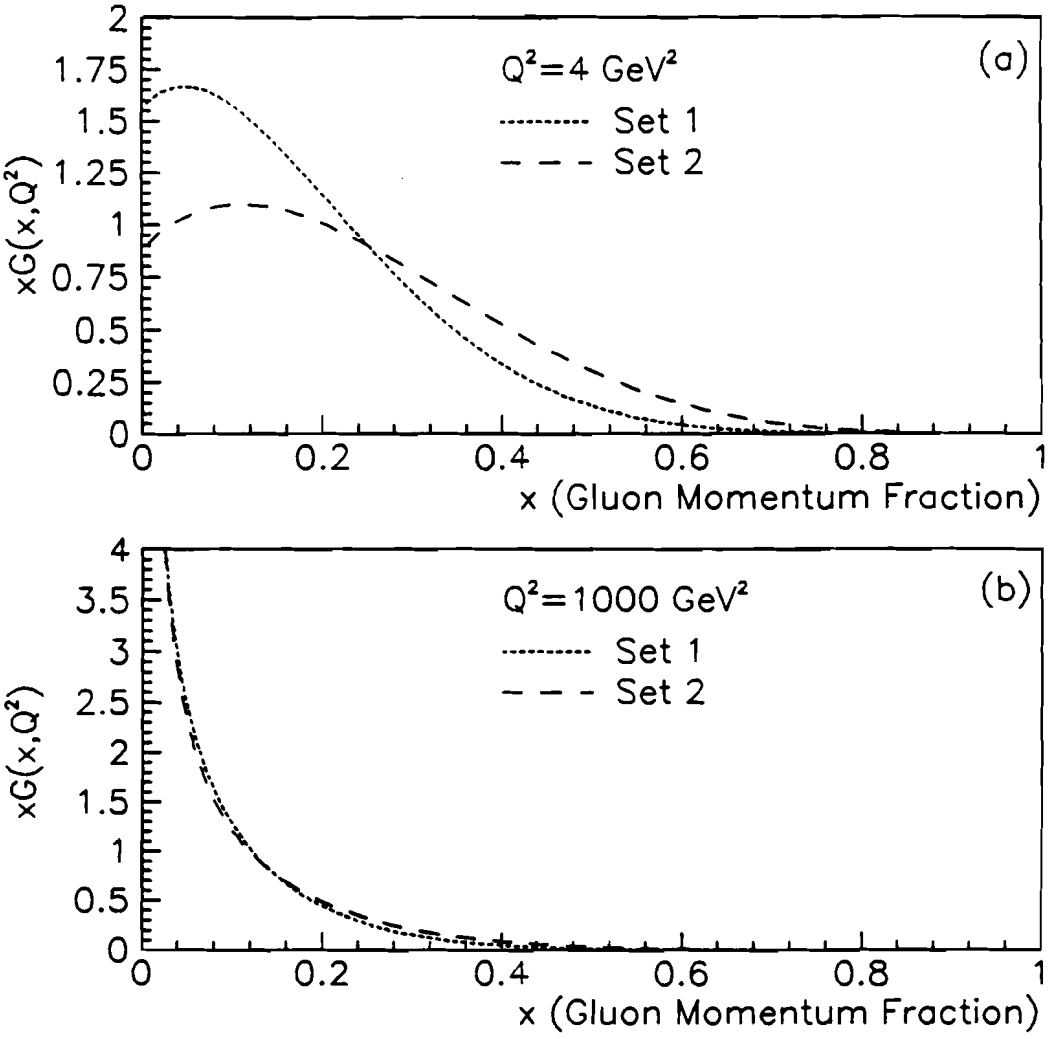


Figure 1.4: Evolution of the Gluon Density in a Proton. The gluon density is plotted as a function of X, the fraction of proton momentum carried by the gluon. (a) $Q^2 = 4\ GeV^2$ and (b) $Q^2 = 1000\ GeV^2$. Also shown is the influence of changing the scale parameter, $\Lambda$, in the definition of $\alpha_S$ where Set 1 corresponds to $\Lambda = 0.2\ GeV$ and Set 2 corresponds to $\Lambda = 0.4\ GeV$. These plots are made using the fit parameters of Duke and Owens [15].

double direct photon system provides the superior scheme with which the the intrinsic momentum may be measured.

## 1.2 Description of a QCD Monte Carlo

We will make extensive use of the leading-log QCD calculations (using software written by Owens [33]) throughout this thesis and as a result, we will describe the basic ideas used in his program here.

As a leading-logarithm calculation, contributions from subproceses with more than two final state partons were included in the cross section determination. This implies that the results are then incorporated into scale dependent distribution and fragmentation functions. We will begin with a short discussion of the subprocess cross sections and then follow that with the scheme used for calculating the parton distribution and fragmentation functions. Since we will be able to probe the structure of the beam partons, we will place more emphasis on the parton distributions than on the fragmentation functions.

### 1.2.1 The Subprocess Cross Sections

The total cross section for the process under consideration is built up from a sum of all possible constituent scattering diagrams each of which is weighted by the appropriate distribution and fragmentation functions; see Figure 1.3. The expressions for the two-body scattering cross sections are given in Table 1.1.

Table 1.1: Parton-Parton Two Body Cross Sections. Constant factors have been omitted and the Mandelstam variables are for the constituent processes.

| subprocess | cross section |
|---|---|
| $qq' \to qq'$ | $\frac{4}{9}\frac{s^2+u^2}{t^2}$ |
| $qq \to qq$ | $\frac{4}{9}\left(\frac{s^2+u^2}{t^2}+\frac{s^2+t^2}{u^2}\right)-\frac{8}{27}\frac{s^2}{tu}$ |
| $q\bar{q} \to q'\bar{q}'$ | $\frac{4}{9}\frac{t^2+u^2}{s^2}$ |
| $q\bar{q} \to q\bar{q}$ | $\frac{4}{9}\left(\frac{s^2+u^2}{t^2}+\frac{u^2+t^2}{s^2}\right)-\frac{8}{27}\frac{u^2}{st}$ |
| $gq \to gq$ | $-\frac{4}{9}\left(\frac{s}{u}+\frac{u}{s}\right)+\frac{s^2+u^2}{t^2}$ |
| $q\bar{q} \to gg$ | $\frac{32}{27}\left(\frac{t}{u}+\frac{u}{t}\right)-\frac{8}{3}\frac{t^2+u^2}{s^2}$ |
| $gg \to q\bar{q}$ | $\frac{1}{6}\left(\frac{t}{u}+\frac{u}{t}\right)-\frac{3}{8}\frac{t^2+u^2}{s^2}$ |
| $gg \to gg$ | $\frac{9}{2}\left(3-\frac{tu}{s^2}-\frac{su}{t^2}-\frac{st}{u^2}\right)$ |

For each event, the Monte Carlo program obtains the fraction of hadron momentum, $x$, for the two initial state partons from a flat distribution between 0 and 1. All four parton level 4-vectors are calculated (including $k_T$ smearing) along with $\hat{s}$, $\hat{t}$ and $\hat{u}$. The hadron level 4-vectors are calculated and $Q^2$ is defined. For $\pi^o$ pairs, if $Q^2$ is defined in terms of the hadron $p_T$, the average $p_T$ of the pair is used. The beam and target distribution functions are then calculated. The target distribution function is weighted according to the number of protons and neutrons in the target material. The weights for the fragmentation (including $k_T$ smearing) into the $\pi^o$ pairs is determined. Each of the processes listed in Table 1.1 is explicitly calculated and the sum over these and higher order terms is made, each being weighted with the parton distribution and fragmentation functions. Given that the final weight is non-zero, histograms are then filled.

### 1.2.2 Distribution and Fragmentation Functions Fits

As previously mentioned, the initial distribution and fragmentation functions must be determined by experiment. Using data from deep-inelastic lepton-nucleon scattering, dimuon mass distributions and from $J/\psi$ $x_F$ distributions, the input functions for the distribution of quarks and gluons in nucleons were determined by Duke and Owens [15]. From these input functions, the parton densities were evolved to higher values of $Q^2$ (using the Altarelli-Parisi equation [2]). In this manner, $Q^2$-dependent parameterizations were made which resulted in very convenient and easy to use functions. The plots in Figures 1.4, 1.5, 1.6 and 1.7 were made using the

parameterizations of Duke and Owens [15].

The fits were actually made twice each time using a different value for the arbitrary parameter $\Lambda$. The first, referred to as Set 1, has $\Lambda = 200$ MeV and the second, referred to as Set 2, has $\Lambda = 400$ MeV. Figure 1.4 shows the effect of the two $\Lambda$ values on the nucleon gluon distribution. It is left to experiment to decide which set of fits best describes the data (recall that $\Lambda$ is an arbitrary constant of integration; see Section 1.1.3). In addition to the gluon distribution, fits were made to the valence quark, the sea quark and the charm quark distributions in the nucleon. The sea quark distribution is defined as the antiparticles of the u, d and s quarks.

In a similar manner, the parton distributions in pions were determined by Owens [32] from $J/\psi$ and dimuon data. Using these parametrized fits to the data, we have plotted the parton distributions for the range of $Q^2$ values accessible in this experiment for the Set 2 fits. In Figures 1.5, 1.6 and 1.7 we have plotted the distributions for both pions and nucleons at two values of $Q^2$: $Q^2 = P_{T1}^2$ and $Q^2 = P_{T2}^2$ where $P_{T1} = 2$ GeV and $P_{T2} = 10$ GeV. We have displayed the plots with a logarithmic ordinate to better view the structure at large x.

Figure 1.5 shows the gluon distributions. The first noticeable feature is that both the pion and nucleon distributions become softer (steeper) at the higher $Q^2$ value. The next characteristic one should notice is that as x increases, the relative weight of the pion gluon density increases over that of the nucleon density.

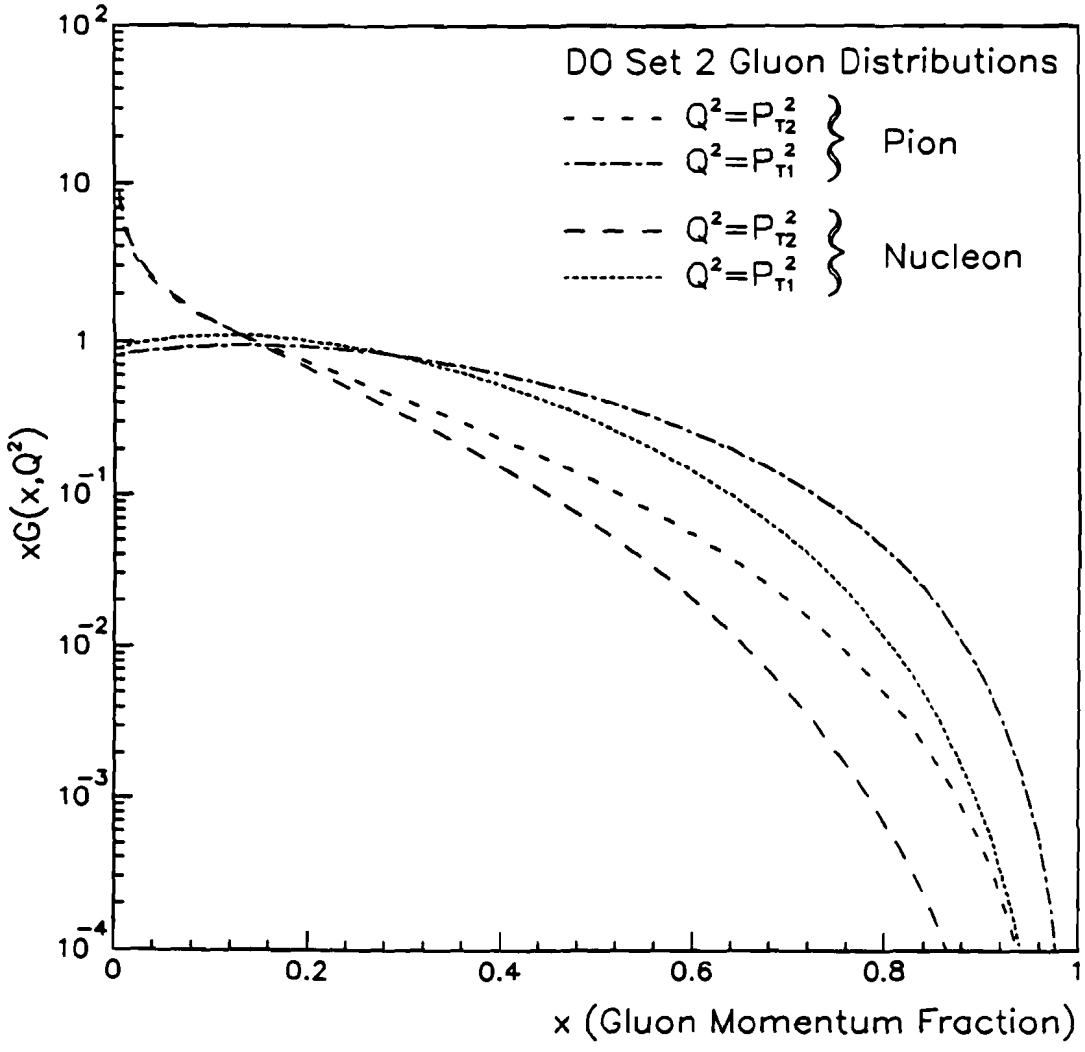


Figure 1.5: Gluon Density in the Nucleon and Pion. The gluon density is plotted as a function of x, the fraction of hadron momentum carried by the gluon. The two choices for $Q^2 = P_{T1}^2 = 4\ GeV^2$ and $Q^2 = P_{T2}^2 = 100\ GeV^2$ show the effect of evolution in the range of $Q^2$ which is roughly accessible in this experiment. These plots are made with the Set 2 fits where $\Lambda = 400$ MeV using the fit parameters of Duke and Owens [15].

In Figure 1.6 we display the valence quark distributions (the up and down distributions have been added together since they are quite similar). We notice here that the pion and nucleon functions are quite different across the entire x-range (except where they intersect). The flatness of the pion distribution is characterized as being harder; the valence quarks within a pion are about as likely to carry 20% of the pion's momentum as they are to carry 80%. On the other hand, the valence quarks within a nucleon are about 100 times more likely to carry 20% of the nucleon's momentum than 80%. Around $x \simeq 0.6$ the pion valence quark density acquires more weight than that for the nucleon.

In Figure 1.7 we observe that the sea quark distributions are quite insignificant at x values greater than about 0.1. Over most of the x-range, the pion distributions dominate. Although not shown here, the charm quark distribution is suppressed at about the same level as the sea distribution. For the fits, it was assumed that the charm quark distribution was zero at our lower value of $Q^2 = 4$ GeV$^2$.

The fragmentation functions used in the Monte Carlo were obtained by hadron production from low $Q^2$ deep inelastic scattering and $e^+e^-$ experiments. The $Q^2$ evolution of the functions was calculated [30] and the fitting procedure is described by Owens [31]. A two-dimensional table in $Q^2$ and $z$ (fraction of parton momentum carried by the materialized. resultant hadron) for the fragmentation functions was constructed and intermediate values were obtained by interpolation.

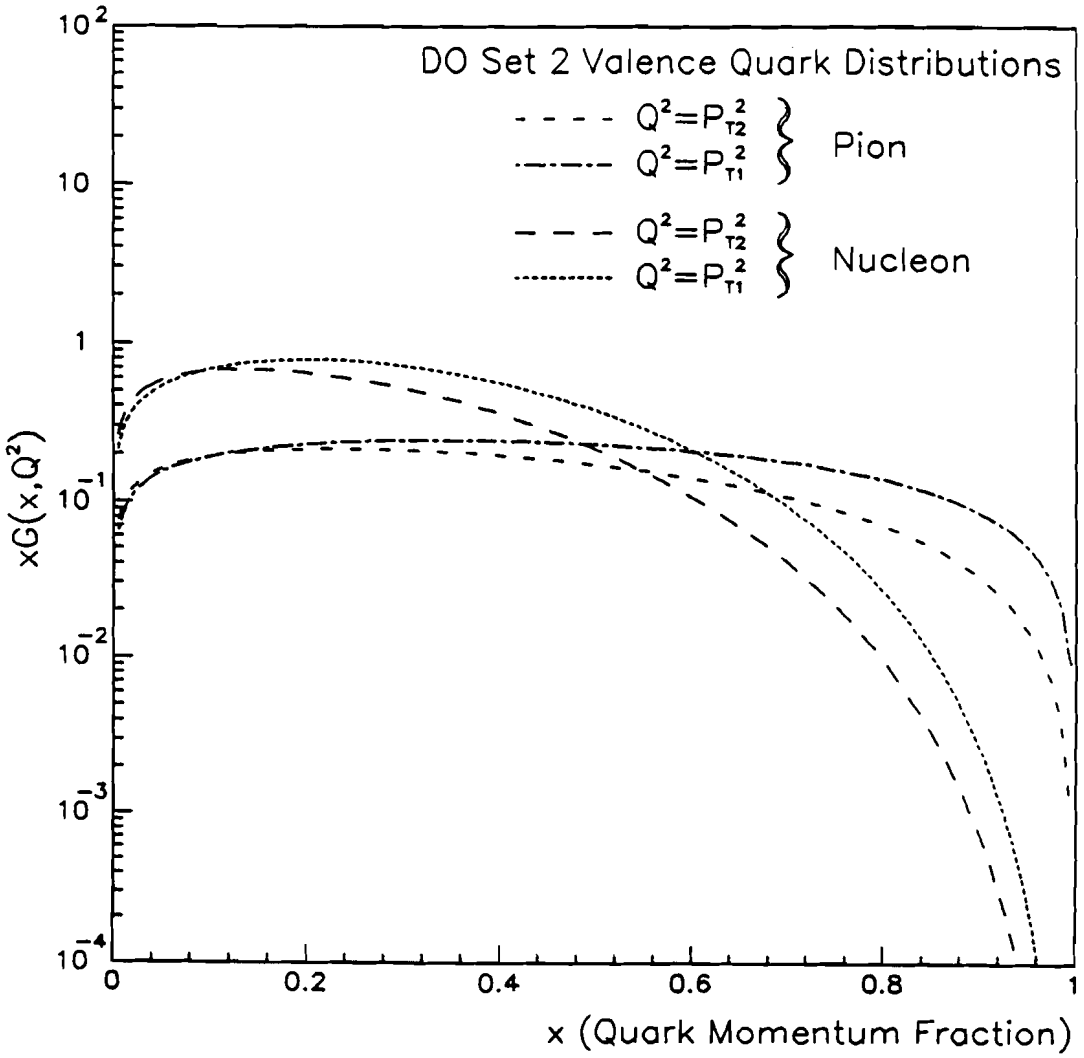


Figure 1.6: Valence Quark Density in the Nucleon and Pion. The quark density is plotted as a function of x, the fraction of hadron momentum carried by the quark. No distinction is made between the up and down quarks in these plots. The two choices for $Q^2 = P_{T1}^2 = 4\ GeV^2$ and $Q^2 = P_{T2}^2 = 100\ GeV^2$ show the effect of evolution in the range of $Q^2$ which is roughly accessible in this experiment. These plots are made with the Set 2 fits where $\Lambda = 400$ MeV using the fit parameters of Duke and Owens [15].

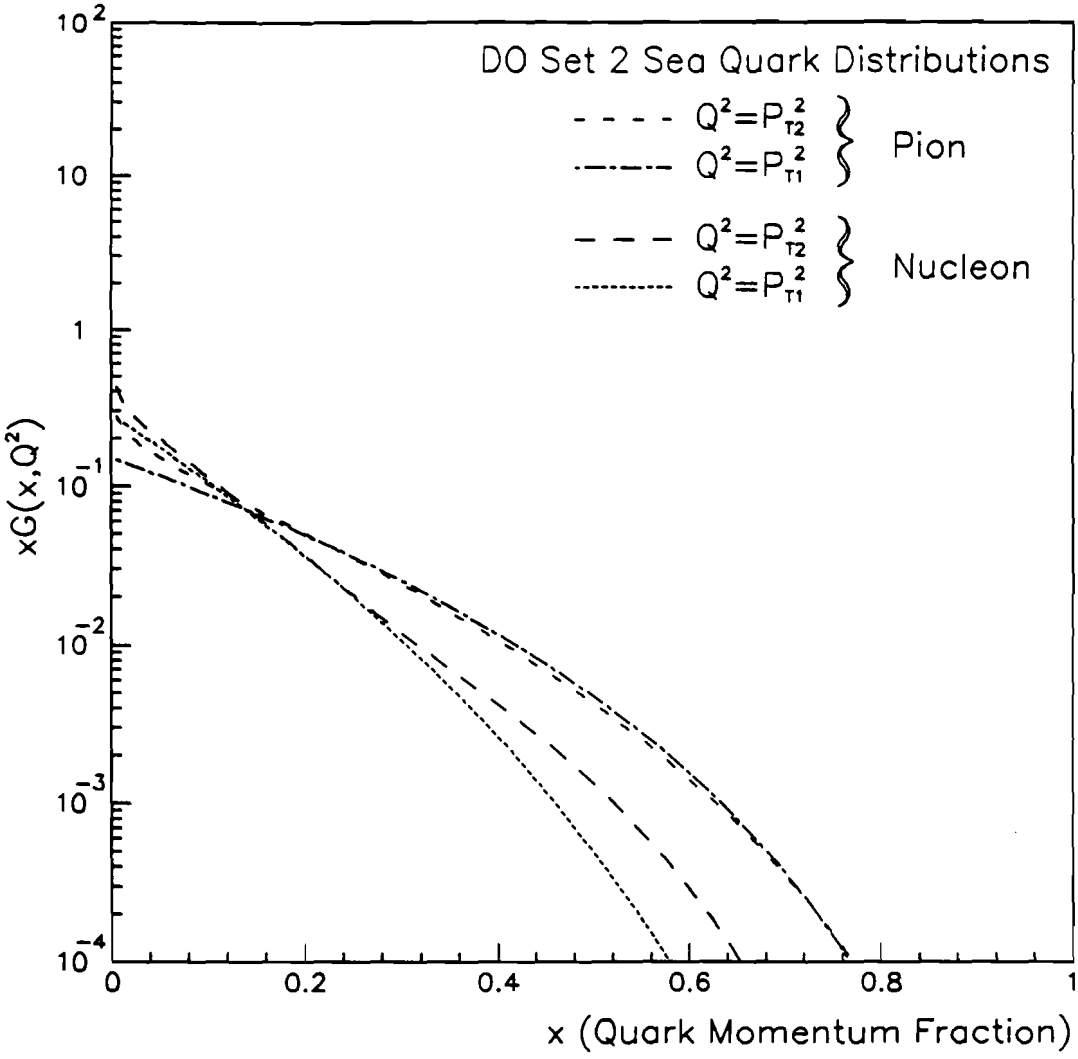


Figure 1.7: Sea Quark Density in the Nucleon and Pion. The quark density is plotted as a function of x, the fraction of hadron momentum carried by the quark. The sea quarks are defined as the anti-particles of the up, down and strange quarks. The two choices for $Q^2 = P_{T1}^2 = 4\ GeV^2$ and $Q^2 = P_{T2}^2 = 100\ GeV^2$ show the effect of evolution in the range of $Q^2$ which is roughly accessible in this experiment. These plots are made with the Set 2 fits where $\Lambda = 400$ MeV using the fit parameters of Duke and Owens [15].

## 1.3 Symmetrically Triggered Events

In the standard description of a high $p_T$ interaction as described by Figure 1.3, the two out-going partons fragment into hadronic jets. If the 4-vectors of the final state jets are well measured, then the parton-level kinematics are completely defined. Because of the large overlap of the beam and target jets with the scattered parton jets, an unambiguous experimental definition of the latter is at best controversial. On the other hand, a reconstructed (or otherwise identified) final state particle (e.g. a $\pi^o$) is a rather well defined experimental quantity. This is one reason for placing emphasis on the di-hadron final state system.

In single particle production, it is possible to trigger on particles which have obtained part of their $p_T$ from the intrinsic $k_T$ of the initial state partons. This configuration corresponds to probing the subprocess at a *smaller* distance than that indicated by the $p_T$ of the interaction; it is also possible that the $p_T$ spectrum will be distorted.

For the production of symmetric pairs, the preferred reaction configuration is one in which the $k_T$ is minimized. If one scattered parton has enhanced $p_T$ from its intrinsic $k_T$, then it is very unlikely that the other scattered parton will have a similarly large $p_T$ component in the opposite direction. This qualitative argument has been supported in a more quantitative format by Baier, Engels and Peterson [6].

## 1.4 Goals of the Thesis

We plan to investigate the yield of $\pi^o$ pairs produced from the collision of a negative pion beam and a proton beam with a stationary nuclear target. We will also investigate some of the properties of the charged particles associated with the $\pi^o$s. We will compare the $\pi^o$ pair yield with the QCD Monte Carlo described in Section 1.2 and we will extract an estimate of the beam parton distribution. We will advance the opinion that the $\pi^o$ pair events tend to be produced from gluons in the beam.

# Chapter 2

# The E706 Spectrometer

In this chapter on the spectrometer, all relevant details of the apparatus will be covered. Since the author was intimately involved in the construction of the wire chambers, some degree of emphasis will be placed on the charged particle detectors.

Studying the nature of high transverse momentum ($p_T$) electromagnetic phenomena and associated charged particles in a fixed target environment calls for a rather specific collection of detector systems. In this experiment, we have used tracking and calorimetry to effect the goal of reconstructing the high $p_T$ events. This chapter will begin with a discussion of these detector systems from an overall perspective followed by more detailed sections on the individual components.

## 2.1 Overall View

The E706 spectrometer consists of about 29,000 distinct detector channels, about 20,000 of which are in tracking and the remainder are in calorim-

etry. Table 2.1 presents a breakdown by detector. In addition to energy information, the calorimeters provided timing information. A plan view of the spectrometer is shown in Figure 2.1 and a plan view of the SSD-Target region is shown in Figure 2.2.

Table 2.1: Breakdown of Spectrometer Channels

| | Number of Channels | Timing Info |
|---|---|---|
| SSDs | 6600 | No |
| PWCs | 13440 | No |
| EMLAC | 6192 | Yes |
| HALAC | 2340 | Yes |
| FCAL | 228 | Yes |

As a component of the trigger, the veto wall identified events contaminated with muons accompanying the primary beam particles. Along with the other scintillation counters used in the trigger, the veto wall will be more fully discussed in Section 3.3. Downstream of the veto wall, the beam chamber silicon strip detectors (SSDs) served to identify the beam par-

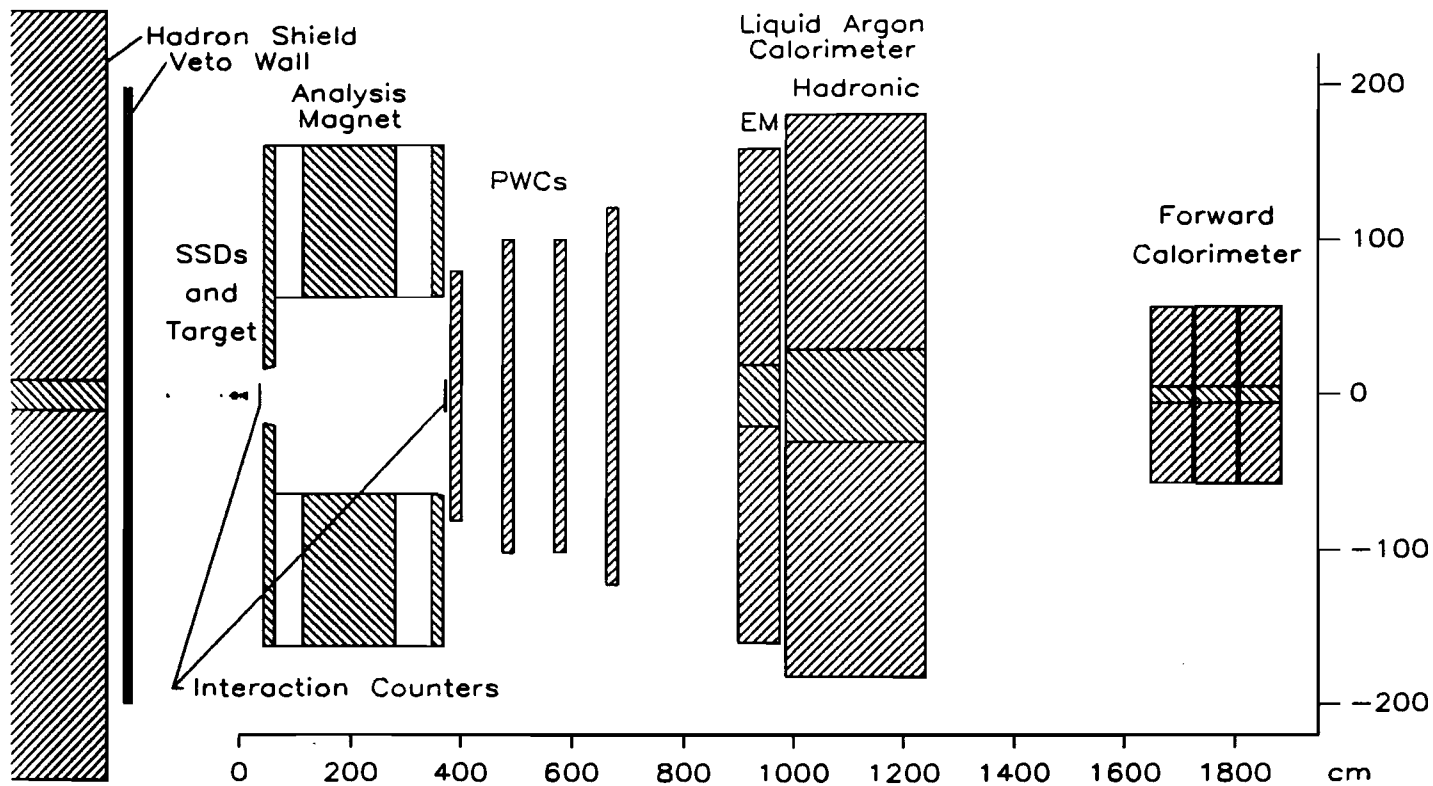


Figure 2.1: Plan View of the E706 Spectrometer; the beam enters from the left.

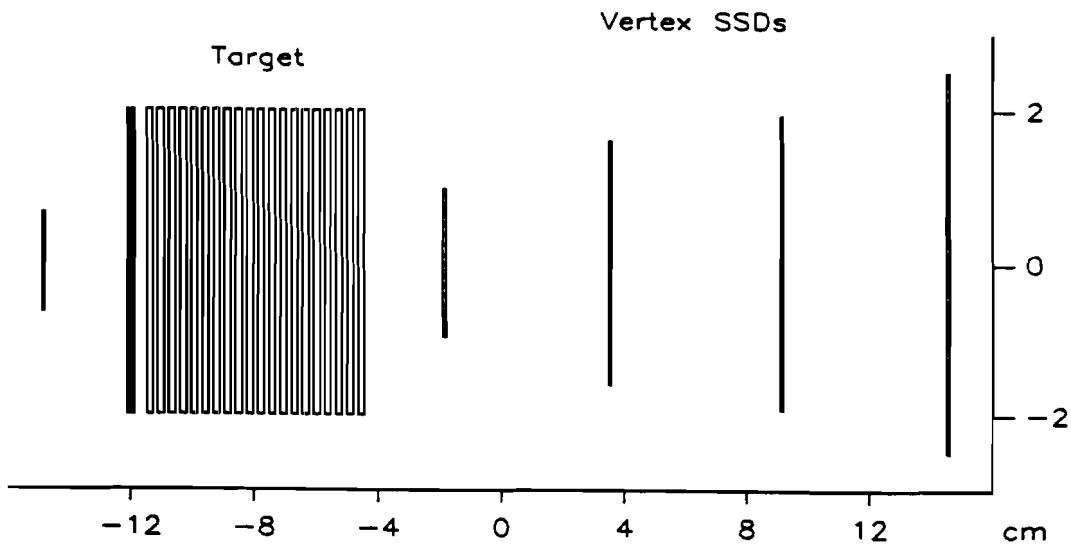


Figure 2.2: Plan View of the SSD and Target Region. The SSD wafer thickness is exaggerated and the beam enters the spectrometer from the left; the two most upstream SSD beam modules are not shown. The two target foils to the left represent the copper segments and the remaining twenty correspond to the beryllium.

ticle trajectory. These SSDs consisted of three modules, each containing one vertical (X) plane and one horizontal (Y) plane. Following the beam SSDs is the segmented target which in turn is followed by a set of four XY SSD modules. This set of SSD planes is used to reconstruct vertices and, in conjunction with the proportional wire chambers (PWCs), to determine the charged particle momenta. A Monte Carlo determination of the SSD angular resolution gives $\sim 10 \times 10^{-3}$ radians.

Between the SSDs and the PWCs is situated the MW9AN spectrometer dipole magnet. At a current of 9600 amperes, it supplied a transverse momentum kick of 450 MeV for all charged tracks.

The PWCs consist of four modules each of which contains four planes in an XYUV orientation. These provide the downstream tracking component of the charged particle momentum measurement. In addition, the PWCs assist in distinguishing electron[1] induced electromagnetic showers from photon induced electromagnetic showers. The angular resolution of the tracking as determined from Monte Carlo is $31 \times 10^{-3}$ radians resulting in a momentum resolution of $\sigma_P/P \simeq 0.09\% \times P$.

For detecting and measuring the energy of electromagnetic and hadronic showers, the PWCs are followed by the liquid argon calorimeter (LAC) comprised of the electromagnetic (EMLAC) and hadronic (HALAC) sections. Both the EMLAC and the HALAC are divided into two components along the beam to give a measurement of the longitudinal development of the

[1]The term *electron* is used throughout this document in its generic sense referring to both positively charged and negatively charged leptons with the mass of the electron.

shower. The EMLAC is comprised of alternating layers of lead and readout boards while the HALAC is constructed of alternating layers of iron and readout boards. Transverse segmentation of the EMLAC into radial and azimuthal strips provides for a position resolution of $\sim 0.5$ mm and an energy resolution $\sigma_E/E \simeq 21\%/\sqrt{E}$. The HALAC is read out from triangular pads providing a position resolution of about 5.0 cm and energy resolution $\sigma_E/E \simeq 80\%/\sqrt{E}$. The EMLAC also provided the signal for the high $p_T$ electromagnetic trigger used in this study. The regions of space between the readout boards and the converters (Pb or Fe) are filled with liquid argon as the ionizing medium.

Situated downstream of the LAC and rounding out the E706 calorimetry is the forward calorimeter (FCAL). The FCAL, which is designed to intercept the forward jet region not covered by the the LAC, is divided into three identical units of alternating layers of steel and scintillator. It provides a measurement of both the total energy and $p_T$ of the forward beam jet with a resolution of $\sigma_E/E \simeq 10\% \div 100\%/\sqrt{E}$.

## 2.2 The MWest Beam and Target

The Meson West (MWest) beam, consisting of 530 GeV positive and negative particles, is generated from collisions of the primary 800 GeV Fermilab Tevatron beam with a fixed beryllium target. With a maximum design momentum of 1000 GeV, the maximum intensity of the primary beam is 2 $\times 10^{13}$ protons per pulse with an acceleration time of 60 seconds and a spill

time of about 23 seconds. The secondary beam is defined in both momentum ($\pm\Delta p/p = 10\%$) and mass with the beamline magnets and a differential Čerenkov counter before being delivered to the E706 spectrometer.

### 2.2.1 The MW Beam

The secondary beam consisted primarily of $p$ and $\pi^-$ for the positive beam and of $\pi^-$ and $\bar{p}$ for the negative: for more precise numbers, see Table 2.2. The secondary beam was delivered to the experiment at a rate of about $2 \times 10^6$ particles per second in spills of about 23 seconds in duration every minute. The between-spill time was used by the accelerator to accumulate and accelerate protons in preparation for the next spill.

The particles in the secondary beam were tagged with a differential Čerenkov counter. The A-dependence of the secondary particle production in the MWEST beamline has been measured [7]. The beamline components including the Čerenkov counter have been described in detail elsewhere [21].

### 2.2.2 The Target

The ideal target for a fixed target hadronic interaction experiment would have the following three properties: a) zero thickness. b) 100% interaction length and c) be composed of a single particle species. In reality, the target must have some finite thickness thereby introducing some uncertainty in the interaction point and presenting the possibility for secondary interactions. A material with less than 100% interaction length allows some fraction of the beam particles to pass through the target without interacting. Most

Table 2.2: Beam Content. Positive and Negative Secondary MWEST Beam Content in Per Cent. The beam particles were tagged with a differential Čerenkov counter and produced with the Fermilab primary 800 GeV proton beam colliding with a stationary beryllium target.

| | Beam Particles | | | |
|---|---|---|---|---|
| Beam Polarity | $p/\bar{p}$ | $\pi^+/\pi^-$ | $K^+/K^-$ | $\mu^+/\mu^-$ |
| Positive | $91.1 \pm 0.2$ | $7.2 \pm 0.2$ | $1.7 \pm 0.1$ | $0.3 \pm 0.1$ |
| Negative | $0.20 \pm 0.01$ | $96.9 \pm 0.2$ | $2.9 \pm 0.2$ | $0.9 \pm 0.1$ |

materials are composed of a combination of protons and neutrons which introduce some uncertainty in the interactions at the parton level. Materials containing equal numbers of up and down quarks (isoscalar targets) are very attractive in that the differences between quarks average out.

In a practical sense, a desirable target material would be easy to handle (machineable and stable in air), reasonably inexpensive and common enough that results may be compared with other experiments. E706 used two different target materials: beryllium and copper. Table 2.3 summarizes the target properties and the number of triggered events we have obtained on each.

The first E706 running period of November 1987 through January 1988 may be divided into five separate beam and target configurations designated Sets A, B, C, D and E. There were two target schemes used: beryllium (Be) and copper plus beryllium (Cu+Be). The Cu+Be target was arranged as four 1.2 mm copper slabs separated by 1.0 mm air gaps followed by twenty 1.2 mm beryllium slabs separated by 0.8 mm air gaps (see Figure 2.2).

## 2.3 The Tracking System

The E706 tracking system, consisting of a silicon strip detector (SSD) system, a proportional wire chamber (PWC) system and the MW9AN spectrometer magnet, existed primarily to measure the momenta of charged particles. Additionally, the SSD system performed as a vertex detector and the PWCs provided, in conjunction with the EMLAC, electron identifica-

Table 2.3: E706 Target Materials. Properties and exposures of the E706 targets to the beam; the numbers of triggered events correspond to all LAC triggers in both positive and negative beam modes.

| | Interaction Length (%) | Radiation Length (%) | Triggered Events ($\times 10^3$) |
|---|---|---|---|
| Be | 5.90 | 6.80 | 2750 |
| Cu−Be | 1.59 − 5.90 | 33.6 + 6.80 | 2451 |

tion.

### 2.3.1 The Silicon Strip Detector (SSD) System

With the advent of solid state detector technology, silicon strip detector systems [23] have become a major component of many fixed target experimental environments. Since the construction of the E706 SSDs at the University of Pittsburgh, SSD planes have become sufficiently common that they are now available commercially [2].

In this section, we will discuss the arrangement and performance of the E706 SSD system.

#### 2.3.1.1 Geometry

The geometry of the SSD-target system layout is shown in the plan view of Figure 2.1. Upstream of the target region there are three XY modules serving as beam chambers (not shown in the above figure). Downstream of the target, four XY modules operate as the vertex detector and as the upstream component of the charged particle spectrometer.

All SSD modules were composed of planes with 50 $\mu$meter spacing (pitch) between the diode strips. The planes were constructed of either 3 cm $\times$ 3 cm or 5 cm $\times$ 5 cm wafers. Not all regions of these planes needed to be instrumented; this not only reduced the complexity of the system, but also minimized the cost without sacrificing acceptance. The wafer size.

[2] For example, Hughes Aircraft Co., Carlsbad, CA., and Micron Semiconductor, Inc., Longwood, FL.

instrumented regions, number of strips and z-position of each SSD plane are given in Table 2.4.

The planes were paired up into vertical (X) and horizontal (Y) modules. As a result, only a portion of the instrumented region of an X-plane overlapped with the instrumented region of the Y-plane within the same module. For example, the X-plane in SSD module 1 is actually sensitive over a region 1 cm × 3 cm and the Y-plane is sensitive over a region 3 cm × 1 cm. The overlapping region is a 1 cm square in the center: the situation is similar for all partially instrumented wafers.

#### 2.3.1.2 Performance

In its capacity as a vertex detector, the SSD system performed entirely as expected. The distribution of reconstructed Z vertex positions is shown in Figure 2.3 where the segmentation of the target is clearly visible. A measure of the Z vertex resolution may be obtained from a plot of the difference of the Z vertex as measured in the X-view and that in the Y-view. From the fit to the distribution, a Z position resolution of 420 $\mu$m may be obtained [43].

### 2.3.2 The MW9AN Dipole Magnet

With iron fabricated in Serpukov and components assembled at Fermilab, the MW9AN spectrometer dipole magnet supplied the 450 MeV $p_T$ kick for all charged particles within its geometrical acceptance. This magnet operated at a current of 1050 amperes for this fixed target run (1987–1988).

Table 2.4: SSD Wafer Parameters. X and Y refer to plane orientation where X strips are vertical and Y are horizontal; "Type" refers to plane location: Upstream (U) or Downstream (D) of the target, see Figure 2.2.

| Module | Plane Number | Wafer Size ($cm^2$) | Type | Intstrumented Region($cm$) | Number of Strips | Z Position ($cm$) |
|---|---|---|---|---|---|---|
| 1 X | 1 | 3×3 | U | ±0.5 | 200 | -129.001 |
| 1 Y | 2 | 3×3 | U | ±0.5 | 200 | -128.114 |
| 2 X | 3 | 3×3 | U | ±0.5 | 200 | -31.872 |
| 2 Y | 4 | 3×3 | U | ±0.5 | 200 | -31.961 |
| 3 X | 5 | 3×3 | U | ±0.5 | 200 | -15.413 |
| 3 Y | 6 | 3×3 | U | ±0.5 | 200 | -14.498 |
| 4 X | 7 | 3×3 | D | ±1.0 | 400 | -2.384 |
| 4 Y | 8 | 3×3 | D | ±1.0 | 400 | -1.470 |
| 5 X | 9 | 3×3 | D | ±1.5 | 600 | 3.067 |
| 5 Y | 10 | 3×3 | D | ±1.5 | 600 | 3.981 |
| 6 X | 11 | 5×5 | D | ±2.0 | 800 | 8.645 |
| 6 Y | 12 | 5×5 | D | ±2.0 | 800 | 9.560 |
| 7 X | 13 | 5×5 | D | ±2.5 | 1000 | 14.086 |
| 7 Y | 14 | 5×5 | D | ±2.5 | 1000 | 15.001 |

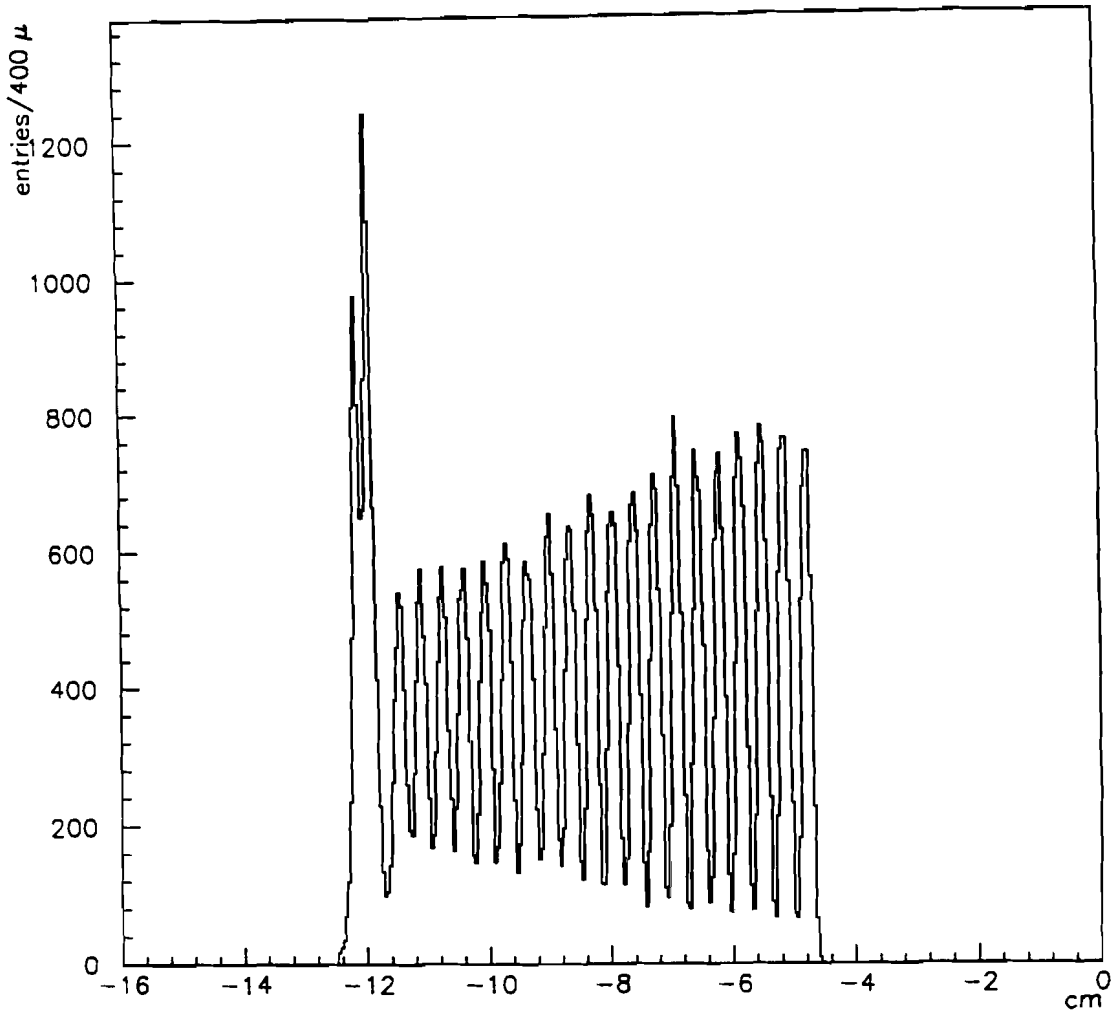


Figure 2.3: Longitudinal (Z) Vertex Distribution. Reconstructed longitudinal vertex position; each target slab is clearly resolved. The two slabs on the far left are copper and the remainder are beryllium.

Although the magnet was not a perfect dipole, the field approached a nearly uniform dipole shape when 20 cm thick mirror plates were installed on both ends of MW9AN. The upstream face of the upstream mirror plate was located at a Z coordinate position of 44.4 cm and the downstream face of the downstream mirror plate was at 354.2 cm. The field was measured to be less than 1 % of its maximum value at the position of the most downstream SSD plane and at the first PWC plane. The field was mapped using a nuclear magnetic resonance probe at currents of 700, 1400 and 2100 amperes and the value of the field integral is believed to be within 1 % of the measured value. At the operating current of 1050 amperes, the Y-component of the field was interpolated to be 6.2 kG.

The yoke was 91.4 cm high, 127.0 cm wide and 83.8 cm long. The geometrical acceptance was defined by the hole dimensions in the two mirror plates. The upstream mirror plate hole was 35.5 cm wide by 25.3 cm high and the downstream mirror plate hole was 127.0 cm by 91.4 cm. The transverse coordinate center was defined to be x=0.0, y=0.0. The longitudinal coordinate center was determined using electrons from photon conversions: see Figure 4.2. A polyethylene bag filled with helium was installed in the central region of the magnet to minimize the effects of multiple Coulomb scattering.

### 2.3.3 The Proportional Wire Chamber (PWC) System

In measuring the trajectory of charged tracks, the PWCs were used to determine the momentum of charged particles (in conjunction with the SSDs)

and to identify electrons (in conjunction with the electromagnetic calorimeter). The E706 PWC system consisted of four independent modules each of which contained a set of four anode planes. For each anode plane, there was a pair of cathode planes, one on either side of the anode. The arrangement of modules is shown in Figure 2.1 while the interleaved layers of anodes and cathodes within a module are shown in Figure 2.4.

#### 2.3.3.1 Geometry

Although all four PWC modules are essentially identical, there are some size differences to maintain an approximately constant acceptance with increasing distance from the target. The active region of each module is roughly equivalent to the sizes of the main cathode regions of that module. These dimensions are given in Table 2.5. The cathodes, constructed of graphite coated 1.0 mil[3] thick mylar sheets, are segmented to decrease the chamber sensitivity in the high rate central beam and diffractive regions. The structure of the central cathode region is shown in Figure 2.4. This segmentation provides for desensitization of anode wires which pass through the central region. These wires, which would otherwise almost always register a hit, are thus able to be sensitive to and see particles outside the central areas.

The anodes were made of 0.8 mil diameter gold-plated tungsten wire stretched to a tension of 40 grams before being soldered and glued to the anode printed circuit board. The wires, for all four modules, were spaced by

[3]The unit of length called the *mil* is equal to $10^{-3}$ inches

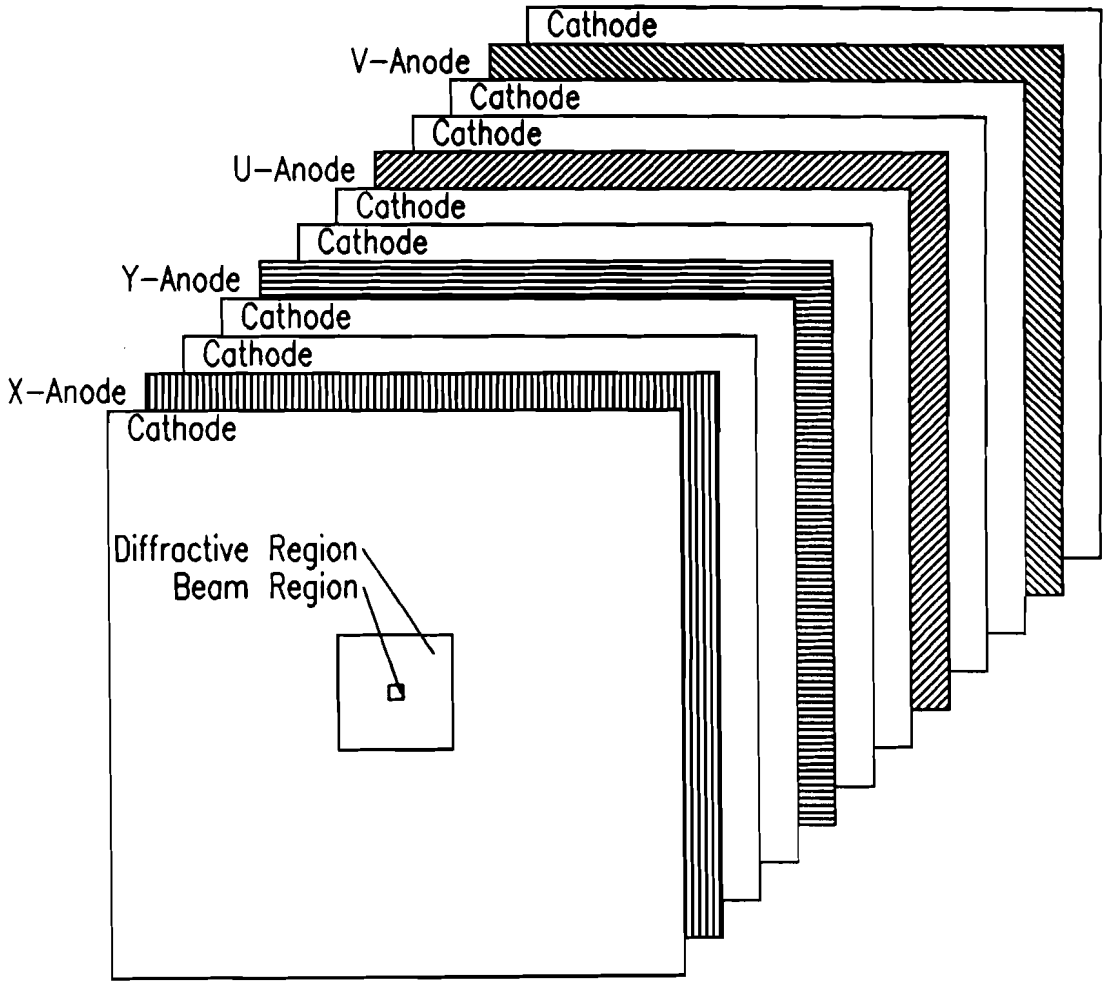


Figure 2.4: Cathode-Anode Arrangement within a PWC Module. The different cathode regions were capable of maintaining different voltages for the purpose of reducing the chamber sensitivity in the central high rate region.

0.1 inch. The distance between the anode and the cathode planes was 0.226 inches. The number of wires, angle of orientation. Z coordinate position and the overall plane efficiency are all given in Table 2.6. The efficiencies and the schemes for calculating these numbers will be discussed in Section 2.3.3.

Table 2.5: Regions of Cathode Segmentation in PWC Modules. All units are centimeters and all cathodes within a module are identical in terms of size and segmentation.

| | Beam | | Diffractive | | Main | |
|---|---|---|---|---|---|---|
| | X | Y | X | Y | X | Y |
| Module 1 | 2.54 | 2.54 | 15.2 | 15.2 | 162.6 | 121.9 |
| Module 2 | 3.81 | 3.81 | 20.3 | 20.3 | 203.2 | 203.2 |
| Module 3 | 3.81 | 3.81 | 20.3 | 20.3 | 203.2 | 203.2 |
| Module 4 | 5.08 | 5.08 | 30.5 | 30.5 | 243.8 | 243.8 |

Table 2.6: PWC Anode Parameters. The definitions of the two efficiency schemes are described in Section 2.3.3.

| Module | Number of Wires | Angle (degrees) | Z Position (cm) | Efficiency(%) Scheme 1 | Scheme 2 |
|---|---|---|---|---|---|
| 1 X | 640 | 90.0 | 380.02 | 92.0 | 96.5 |
| 1 Y | 480 | 0.0 | 381.77 | 95.2 | 99.6 |
| 1 U | 704 | -53.1 | 383.52 | 94.1 | 96.0 |
| 1 V | 672 | 36.9 | 385.27 | 93.8 | 96.8 |
| 2 X | 800 | 90.0 | 473.30 | 95.2 | 93.1 |
| 2 Y | 800 | 0.0 | 475.05 | 94.5 | 98.6 |
| 2 U | 896 | -53.1 | 476.80 | 94.0 | 94.7 |
| 2 V | 896 | 36.9 | 478.55 | 91.9 | 92.2 |
| 3 X | 800 | 90.0 | 567.75 | 93.1 | 95.6 |
| 3 Y | 800 | 0.0 | 569.50 | 95.2 | 97.2 |
| 3 U | 896 | -53.1 | 571.25 | 95.0 | 91.4 |
| 3 V | 896 | 36.9 | 573.00 | 92.0 | 92.2 |
| 4 X | 960 | 90.0 | 660.29 | 95.0 | 87.2 |
| 4 Y | 960 | 0.0 | 662.05 | 95.0 | 97.4 |
| 4 U | 1120 | -53.1 | 663.81 | 93.7 | 90.0 |
| 4 V | 1120 | 36.9 | 665.57 | 94.3 | 91.9 |

#### 2.3.3.2 Cathode Construction

The cathodes were constructed[4] of 1.0 mil mylar sheets stretched on a vacuum operated mylar stretching table (designed and built at Penn State) to a tension of about 40 lbs. per foot before being glued to the G-10 frame. Since the G-10 frame was not sufficiently strong to maintain their designed shape under the tension of the stretched mylar, the glued G-10 mylar unit was stored on a temporary transfer frame. When the construction of a cathode was complete, it was transferred to its permanent support structure. The permanent support frames for modules 2, 3 and 4 were fabricated of iron while that for module 1 was aluminum. This was intended to minimize any interaction of the first chamber module with the field of the spectrometer magnet.

The high rate central region was made insensitive with three electrically independent cathode regions. After carefully masking these areas using standard transparent Scotch tape, three holes (one for each region), approximately 1/4 inch in diameter, were made in the mylar with a heated cork punch. The holes were inspected for irregularities which might cause electrical breakdown in a high voltage environment. On the conductive side of the cathode, the hole was covered with Scotch tape while on the other side conductive epoxy was applied to the hole. A small piece of slightly sanded aluminized mylar was applied to the conductive epoxy. When the

[4]PWC modules 1 and 2 were constructed at Penn State while modules 3 and 4 were constructed at Michigan State University. The construction scheme for modules 1 and 2 will be discussed here.

epoxy hardened, the Scotch tape over the holes was removed. This scheme allowed for the electrical connection through the mylar to the various cathode regions from the back, non-conductive side.

After securing the electrical connection through the mylar, the cathode was ready for its first coating of the graphite paint. This paint was made of a mixture of graphite and ethyl alcohol. The coating of graphite was applied using an automatic sprayer designed and built at Penn State. Between each of three light coats, the graphite was buffed with a piece of soft non-abrasive cloth to provide a uniform coating. A measurement of the uniformity was made by measuring the resistance per square. The sixteen cathodes for modules 1 and 2 were typically measured to be $\sim 2\Omega - 10\Omega$ per square depending on the cathode. Within a cathode, the measurements were consistent within about 7 %.

At this point a critical step in the masking process was ignored. Near the edge of the Scotch tape mask, the graphite liquid made a meniscus which when dried with the tape removed, provided a very sharp edged ridge along the cathode boundaries. When high voltage was applied to the cathodes at Fermilab, the sharp, pointed conductive ridge produced a high density field region which quickly ionized the gas and caused continuous breakdown. A number of small ($\sim$ 5 mm in diameter) holes were burned through the mylar along these ridges. When the ridges were removed with Q-tips and alcohol, the high voltage breakdown stopped and normal operation was observed. Although these holes were aesthetically displeasing, no compromise in chamber performance was observed as a result.

After buffing, a high-voltage feed wire was attached to the aluminized mylar tab and stretched along the back of the cathode. This wire was fastened to the G-10 frame and connected to another wire which lead to a feedthrough high voltage connector. There were three high voltage wires in this connector – one for each cathode region.

On the graphite side of each cathode a set of garland support structures were installed to provide stability for the rather long anode wires. Although the anode wires were tensioned to very near their tensile limit, more support was needed to maintain a constant distance between the anodes and cathodes. These garlands were constructed of zig-zagged pieces of Kapton which stretched from side-to-side or top-to-bottom depending on the anode orientation. For the X and U planes, the Kapton garlands were horizontal while for the Y and V planes, they were vertical. Since the presence of the the garland disturbed the shape of the electric field, a field restoring wire was installed along with each garland. The locations of these garlands on the cathode planes are given in Table 2.7. The chamber efficiency in the garland region decreased to a mean value of $84.6 \pm 1.1$ % from a mean value of $94.5 \pm 0.3$ % for the regions without garlands[5].

After a short period of time ($\sim$ 6 hours) at high voltage, small sections of the U and the V cathodes were observed to become coated with a thin layer of light colored material. These sections were in the corner of the cathodes just outside the outermost of the three anode guard wires[6] and

[5]These numbers are based on Scheme 2 efficiency calculations; see Section 2.3.3.

[6]Since the U and V anode planes were rotated relative to the X and Y planes (see

Table 2.7: PWC Cathode Garland Locations. The positions are relative to the origin in the x-y plane.

| | Orientation | Location (cm) |
|---|---|---|
| Module 1 | | |
| X & U | horizontal | $\pm 2.54, \pm 38.1, \pm 43.2$ |
| Y & V | vertical | $\pm 17.8, \pm 22.9, \pm 58.4, \pm 63.5$ |
| Modules 2 & 3 | | |
| X & U | horizontal | $\pm 12.7, \pm 17.8, \pm 43.2, \pm 48.3, \pm 73.7, \pm 78.7$ |
| Y & V | vertical | $\pm 12.7, \pm 17.8, \pm 43.2, \pm 48.3, \pm 73.7, \pm 78.7$ |
| Module 4 | | |
| X & U | horizontal | $\pm 15.2, \pm 20.3, \pm 50.8, \pm 55.9, \pm 86.4, \pm 91.4$ |
| Y & V | vertical | $\pm 15.2, \pm 20.3, \pm 50.8, \pm 55.9, \pm 86.4, \pm 91.4$ |

extended for about one inch toward the corner. It is believed that this discoloration was due to electrical breakdown on the last anode guard wire since it had more field lines terminating on it from the cathode than any of the other anode wires. We decided to remove a band of the graphite about 1 inch in width along and outside of these outer region guard wires. This modification resulted in triangular regions in each of two corners of each slant (U and V) planes of Modules 1 and 2 which were electrically floating. No discoloration near the boundary guard wires was subsequently observed.

#### 2.3.3.3 Anode Construction

The anode wire frames were constructed of a pair of laminated *G-10* boards the thinner of which was a printed circuit (PC) board. To this PC board, the anode wires were glued and soldered. While the thicker *G-10* board extended the full length of the chamber, the etched boards were typically 16 inches long. We were not terribly successful at bonding these anode boards to the *G-10* support boards with high precision. Since we were able to find solutions to these problems, they ended up being only a nuisance. Our plan was to solder first, then glue. We were able to avoid the problem by gluing the wires in their precise locations first, then soldering them to the appropriate pad on the PC board. The wires were spaced by 0.100 ($\pm$0.002) inches using a digital readout and wire laying system designed and built at Penn State.

---

Table 2.6) the wiring of these anodes extended only to about 6 inches from the corners.

The gold-plated tungsten anode wires were stretched to a tension of 40 grams. Each anode was initially equipped with three grounded "guard" wires which preceded the first and followed the last anode wires. The guard wires successively increased in diameter with distance from the anode wires. The first guard wire was 1.0 mil diameter, the second was 1.2 mil and the third was 5.0 mil. In practice, these guard wires had no apparent effect on the chamber operation. In fact, the outer guard wires of the slant planes were found to be causing electrical breakdown. The remedy for this situation is described in the section on cathode construction.

The chamber was found to draw the same current (0.6 $\mu$ amperes at 2900 Volts in air) when the guard wires were grounded as when they were allowed to float. For the E706 run, the guard wires were grounded.

The traces on the anode boards to which the wires were soldered either lead to a twenty pin (sixteen signal lines and four ground lines) or to a thirty-six pin (thirty-two signal lines and four ground lines) connector located on the outer edge of the anode wire board. These connectors on the outer edge were in the gas box region of the chamber. A short cable carried the signals from these connectors to gas-tight sixteen-pin feedthrough connectors mounted on the gas box leading to the outside world. Into these gas box connectors were mounted the Nanometric System [29] signal amplifiers (see Section 2.3.4).

#### 2.3.3.4 Gas Components

Flowing through the chambers at a total rate of about two liters per minute, the PWC gas was composed of 18.0 % isobutane. 1.1 % isopropyl alcohol vapor, 0.1 % freon with the balance being argon. As the primary component of the mixture, argon provided most of the electrons produced from ionization. The other gases were added mainly to promote high gain under stable operating conditions. In this section, we will briefly discuss the function of the various components in the gas: the next section will describe the hardware used to deliver the final blend. For a more complete review of PWC behavior in various gases see [39. Section 5.3].

In traversing any gaseous medium, energetic. charged particles will ionize the molecules and in the presence of an electric field, the free electrons will drift along the field lines to the anode. In a multiwire chamber, the field assumes a cylindrical symmetry near the wire anode where the drifting electrons become sufficiently energetic to produce subsequent ionization. These secondary ionization electrons may in turn ionize more molecules. This process, referred to as an *avalanche*, may produce a signal gain $10^7$ times the original primary ionization. The gas filling is chosen to maximize this signal avalanche without inducing continuous breakdown.

An obvious first choice for a chamber gas is one of the noble gases. The advantage of a noble gas is its inertness (filled electronic shell structure) and. as such, it will not easily react with any of the chamber components. On the other hand, such a highly symmetric atom has very few modes through

which energy may be absorbed and dissipated. Those modes available for absorption are are ionization and excitation to higher electronic levels.

As one goes down the periodic table, along the noble gas column, the size of the atoms increase while the ionization potentials decrease. A lower ionization potential results in a lower chamber operating voltage. Although this behavior is desirable, the rather exotic noble gases like xenon or krypton are relatively expensive. The first affordable choice leads one to argon.

During the avalanche process, argon atoms are both excited and ionized. The primary mode through which an excited argon gas atom may dissipate energy is radiative transition back to its ground state. The PWC cathodes are made of graphite in which carbon may absorb one of the argon radiated photons (11.6 eV) generating a photoelectron which may then produce a spurious avalanche. The positively charged argon ions will drift towards the cathode and there be neutralized. It is possible that this neutralization process may also radiate a photon or extract another free electron, either of which may produce yet another spurious avalanche. These problems may be minimized by adding polyatomic components, called *quenchers*, to the argon.

Large, asymmetrical molecules function well as quenching components in chamber gases. One of the most popular for PWC applications is isobutane ($C_4H_{10}$) at the 20% level (of total gas content). The photon absorbtion spectrum of isobutane has a large overlap with the emission spectrum of argon. Its large size and structure provides for many modes (vibrational and rotational) through which the energy from absorbed photons may be

dissipated without ionizing or radiating.

In addition to photon quenching, a small quantity of an electronegative gas has been found to be very effective in absorbing the photoelectrons produced at the cathode. This is the role filled by the halocarbon freon 13B1. It may be viewed as an absorber of a small number of free electrons. Obviously, too much of this gas is not a very good idea, but concentrations at the 0.1 % level have been found to improve the operating characteristics of chambers without deterioration of the signal. Also, the negatively charged freon ion is incapable of producing an avalanche due to its rather large size, compared to the electron.

The avalanche process can (and does) produce a large variety of molecular species. Of the products generated in an avalanche, those which polymerize present the most serious problems. With large large dipole moments, alcohols tend to concentrate near the surfaces of the anodes and cathodes. Those near the cathodes neutralize many of the avalanche products which tend to polymerize. The addition of isopropyl alcohol has been found to minimize the effects of aging in wire chambers [42].

#### 2.3.3.5 Gas Delivery and Mixing System

Each of the three gas sources were pressure controlled with one regulator on the cylinder and another at the gas mixing station. The individual gases were then flow controlled separately with an automatic flow control system. The argon gas was taken from the gas of a liquid argon dewar and the isobutane was taken from the gas of a liquid isobutane cylinder. The freon

was obtained pre-mixed with argon in a ratio of 1:25 in a high pressure cylinder (1900 PSI).

The automatic flow control system consisted of three Datametrics [7] model 825 mass flow controllers and a Datametrics 1511 controller unit. The 825's performed two functions: measurement and control of gas flow. They were powered, controlled and monitored by the 1511 which provided digital readout of flow and set points for each channel.

After flowing through the flow controllers, the argon and argon-freon components were combined and passed through a tank of 10° C isopropyl alcohol at 6 PSI to obtain a 1.4% mixture of the alcohol vapor in the gas. At this temperature, the alcohol has a vapor pressure of 0.02 atmospheres. The argon-freon-alcohol mixture was then combined with the isobutane producing a final 1.1% alcohol vapor in the final blend. The combined gas was then fanned out to the four PWC modules.

This scheme also allowed for automatic compensation in total flow volume in the event the gas to one or more chambers was turned off (e.g. in the event of a broken wire). The overall flow rate for four PWC modules was about 1.5 liters per minute and this flow was monitored with the Datametrics unit and with a series of mechanical flow meters. The system was also monitored with a visual inspection once per shift during the running period and with a low pressure alarm system on each gas channel.

Overall, the system was quite reliable when supplying gas for all four

[7] Datametrics/Dresser Industries, Inc. 340 Fordham Road, Wilmington, MA. 01887.

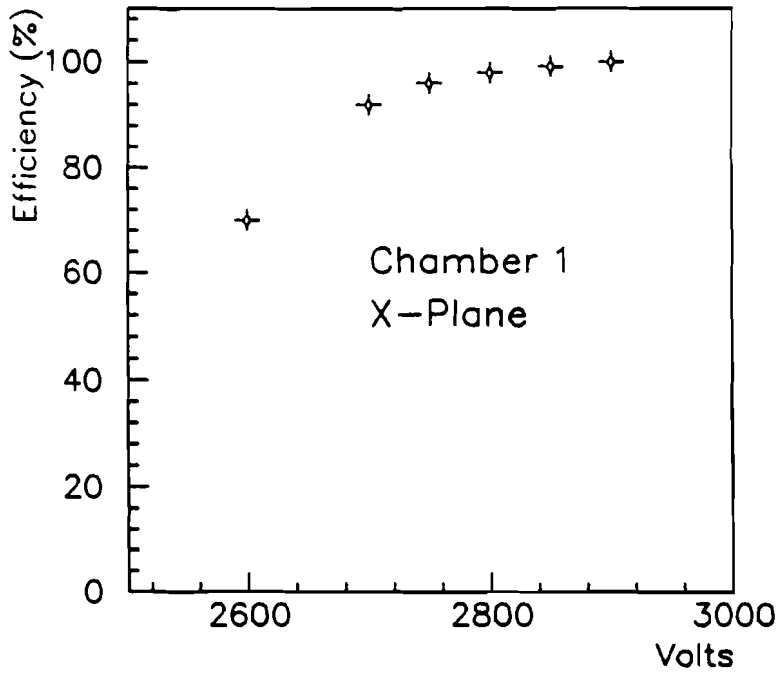


Figure 2.5: Sample Wire Chamber Plateau Curve. All sixteen planes behaved in a very similar manner.

Overall, the system was quite reliable when supplying gas for all four modules.

**Performance**

There are a number of ways to measure the performance of the PWCs. The first method is to measure the "plateau curve". The plateau curve determines the operating voltage of the chamber; it is the point at which one obtains maximum amplification before continuous breakdown (see Figure 2.5). We see from this figure that the operating voltage is about 2800 Volts.

ment. Measured in this manner, the efficiency has two components: hardware and software. The hardware efficiency in this context refers to the number which indicates the probability that a hit for a particular wire was recorded by the complete hardware system (PWC + PWC electronics + data acquisition system) given that a track was known to have passed very nearby. [8] It is possible to extract the efficiency of the tracking software given that a known track deposited a set of hits in the chambers.

Due to the large size of the PWCs, and the constraints of limited computer time, it is practically very difficult make a high statistics efficiency measurement of all wires. As a result, an average over sets of wires was measured.

The Scheme 1 efficiency determination was performed by Easo [16] and the results are shown in Table 2.6. In essence, this technique may be described as follows: a) choose a plane, b) reconstruct a track without using this plane (but require a 15-hit track with the remaining fifteen planes), c) project the track to the plane in question and ask: Is there a hit within the chamber resolution at this point? This scheme is measuring the efficiency of the hardware components of the tracking system; it is circumventing the effects of the software.

Scheme 2 is a somewhat simpler yet biased method for estimating the efficiency. It may be described as follows: a) choose a track b) loop over all planes and check for unused planes. An unused plane indicates an ineffi-

[8] "Nearby" here means that the track was close enough that sufficient charge was deposited on the wire to overcome the amplifier threshold.

ciency in the system. In this technique, the efficiency being measured is that of the hardware *plus* the software. The set of tracks used for this scheme 2 efficiency determination was selected as electrons from the conversion of photons. This requirement places a rather high degree of confidence in these tracks; they are not likely to be fake. These *zero-mass-pair* (ZMP) tracks have the property that in any particular Y-plane, they hit chambers in very nearly the same Y-position (see Section 4). As a result, these tracks will typically deposit twice as much charge on the Y-wires as non-ZMP tracks. This is observed as an increase efficiency for the Y-planes (see Table 2.6) using these tracks.

Comparing the two lists of numbers for the plane-by-plane efficiencies, we have a rather rough agreement. The errors implied by the precision with which the numbers are presented correspond to statistical errors only. The discrepancies in the number are apparently due to some as yet unaccounted-for systematic uncertainties.

### 2.3.4 The Nanometrics Readout System

The electronic readout scheme employed for the SSD and the PWC detectors were identical after the preamplifier boards of the SSDs. This common readout was provided by the commercial vendor Nanometrics Systems, Inc. [29] and maintained by Fermilab's electronics repair group (PREP). The preamplifier system of the SSDs is described in detail in the thesis of Mani [27]. Here we will provide an outline of the basic components of the Nanometrics System: for more details see the Nanometric Systems documentation.

The first electronics module seen by the charge collected on a PWC wire is the Nanometric *N-277* sixteen channel amplifier/discriminator (330 $\Omega$ input impedance) which is sensitive to $\sim 1/2$ $\mu$ampere ($\pm$ 150 nanoamperes). The ECL time-over-threshold output is limited to a 45 nsec wide pulse. The discriminated ECL output is controllable with an external threshold voltage where 1 volt = 1 $\mu$ampere over a range from 0 to 20 $\mu$amperes. The threshold voltage for the PWCs was typically $\sim$ 1.2 volt. The *N-277* card was also implemented with a test pulse pin which allowed diagnostic testing by pulsing each channel on the board.

Each *N-277* card required +5.0 volts at 0.4 amperes and -5.2 volts at 0.68 amperes. With 260 of these amplifier boards, PWC Module 4 had the largest demand requiring 104 amperes at +5.0 volts and 177 amperes at -5.2 volts.

The ECL output of the *N-277* was passed to signal/delay cables of about 50 feet in length which connected to the Nanometric *N-278* Data Latch units. Each latch unit received 32 ECL input signals each of which was delayed for up to 650 nanoseconds and then loaded into a 32 bit buffer register. The data in the buffer was latched when the leading edge of the input pulse arrived within the range of a 100 nanosecond "load" pulse provided by the trigger logic. Each channel in the latch unit was capable of having its internal delay programmed in a range from 300 to 650 nanoseconds. Although the latch unit channels were capable of a delay out to $\sim$ 700 nanoseconds, they became more unreliable in this region. Nonetheless, the time required by the trigger logic forced the delays to be in the 700

nanosecond area resulting in some detector inefficiencies.

The load pulse was followed by a data read from the Nanometrics *N-280* dedicated Crate Controller in which only the non-zero words were read. The latched data were passed through a software controlled wire map to assign hits within the data word to a wire address. Each wire address is composed of a 15 bit word allowing up to 32,768 wires.

Each *N-280* Crate Controller was connected serially to the *N-281* CAMAC Interface Module. From the *N-281*, data were transferred directly to memory in a PDP-11 micro computer. There was one CAMAC interface module for the SSD system and one for the PWC system. The Nanometric system allowed for stacking of events in the different system units: while one event was in the CAMAC Interface Module, the next was in the Crate Controller memory and the third was in the Latch unit buffer. This decreased system dead time by a factor of three.

## 2.4 The Liquid Argon Calorimeter

The primary component of the E706 spectrometer is the three meter diameter liquid argon calorimeter (LAC). This device consists of an electromagnetic (EMLAC) section in the front followed by a hadronic (HALAC) section in the rear; both calorimeters are installed in the same cryostat. The LAC provided for the measurement of position and energy of electrons, photons and hadrons. In this section, the two calorimeters will be discussed separately.

### 2.4.1 The Electromagnetic Section

The primary function of the EMLAC is to measure the energy and position of electromagnetically interacting particles.

#### 2.4.1.1 Geometry

The EMLAC is constructed of four mechanically independent quadrants held together by the overall support structure. Each quadrant is composed of sixty-six layers in each of which 2 mm lead plates are separated from *G–10* readout boards by 2.5 mm liquid argon gaps. The lead plates are quadrant-sized while the readout boards are octant-sized. The readout boards alternate in $r$ and $\phi$ coordinates making thirty-three layers of each type. The $r$ coordinate board consists of 256 concentric radial strips; these strips subtend a constant angle focused on a point 9 meters upstream such that the $r$ strips increase in width with increasing distance from the target point. The $\phi$-strips are divided into inner-$\phi$ and outer-$\phi$ sections at a distance of 40.0 cm from the center of the calorimeter (44.4 mradians in the laboratory azimuthal angle). A perspective view of the EMLAC is shown in Figure 2.6.

Electrically, the EMLAC is divided into front and back longitudinal sections in which each of the corresponding channels of the first eleven ($r$ or $\phi$) boards are ganged together and read out as a unit of eleven strips. Similarly, the back layers are ganged together and are read out as a unit of twenty-two strips.

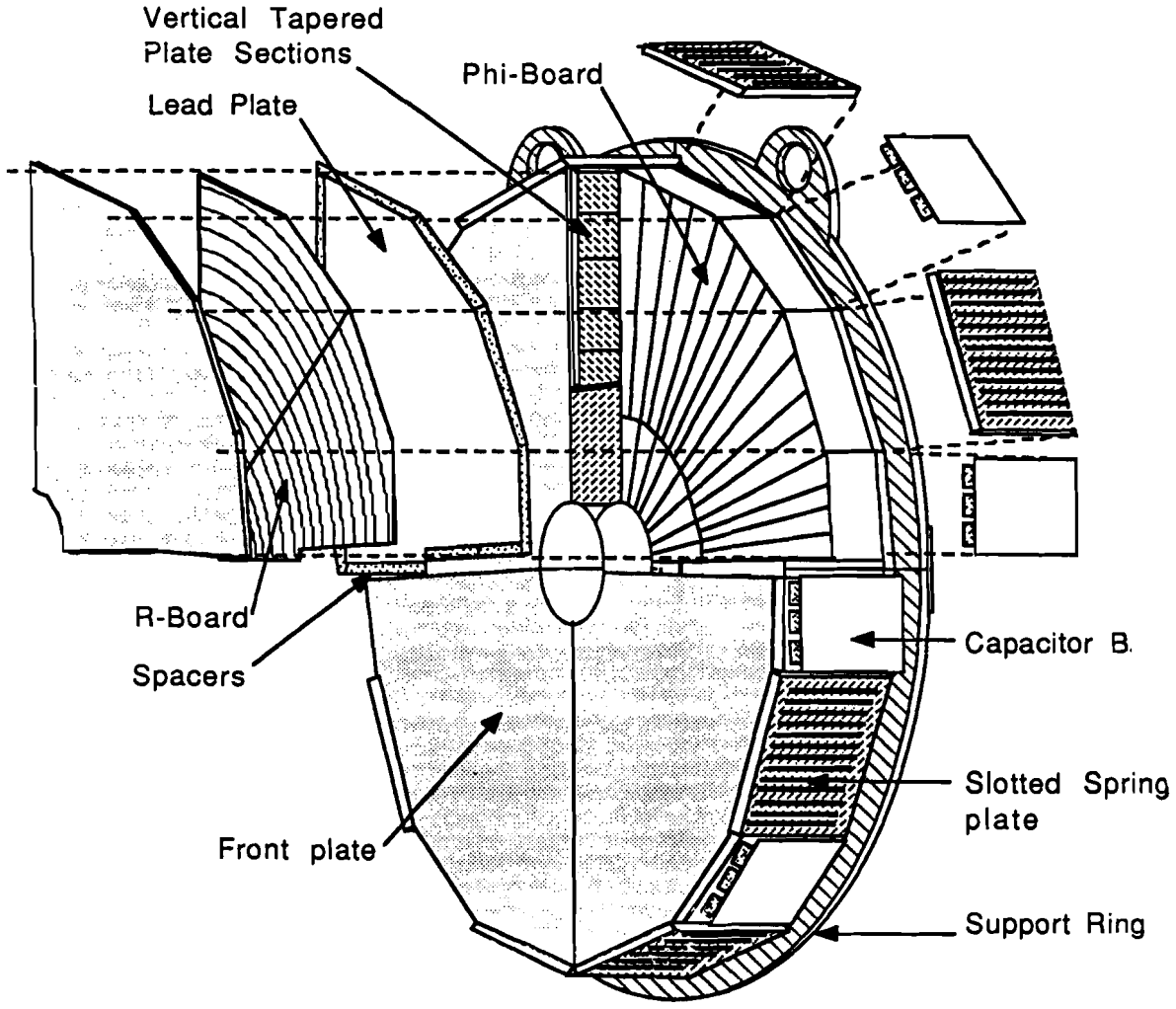


Figure 2.6: Perspective View of the EMLAC. All primary components of the detector are visible.

#### 2.4.1.2 Performance

Since the operational performance of the EMLAC is a rather complicated issue. Chapter 4 has been devoted to this topic.

### 2.4.2 The Hadronic Section

The hadron calorimeter (HALAC) hangs in the liquid argon dewar behind the EMLAC. As implied by its name, the function of the HALAC is to measure the position and energy of hadronically interacting particles.

#### 2.4.2.1 Geometry

The HALAC is comprised of fifty-two 2.5 cm annular cells each of which consists of a 2.54 cm stainless steel absorber plate separated by 3 mm from the *G-10* readout board. To maintain at least the same solid angle as the upstream detector components, the HALAC extends 12 feet from top to bottom. The charge collection pads on the copper-clad *G-10* readout boards were cut into equilateral triangular shapes to minimize the X-Y correlation problem in the reconstruction software. These triangular pads increase in size with Z, subtending the same solid angle from the target. From the first cell, with a height of 10.9 cm, the pad size increased to 13.3 cm in the last cell.

#### 2.4.2.2 Performance

The HALAC is most effective in identifying hadronic showers when used in conjunction with both the EMLAC and the charged particle spectrometer. This arises primarily from the difficulties inherent in hadron calorimetry. In particular, energy is lost in nuclear excitation and breakup which can typically be as high as 30 %. In addition to this, sampling fluctuations give rise to large, difficult-to-measure losses.

## 2.5 The Forward Calorimeter

Downstream of the liquid argon dewar, at a distance of about 15 meters from the target, the forward calorimeter (FCAL) is designed to intercept the forward jet region not covered by the the LAC. Capable of operating at rates of 10 megahertz, the FCAL is divided into three identical units of alternating layers of steel and scintillator. It provides a measurement of both the total energy and $p_T$ of the forward beam jet [10]. This section on the FCAL represents only an overview of the structure since results from this device were not used in this analysis.

The FCAL is composed of three identical modules each containing thirty-two 3/4 inch thick steel plates each of which is separated by 1/4 inch. Between the steel plates is sandwiched the 0.18 inch thick sheets of acrylic scintillator. On a 4.5 inch grid, holes through the entire of stack of scintillator sheets and steel plates accommodate the seventy-six 34 inch long, 0.38 inch diameter wavelength shifter rods. The holes in the scintillator sheets

are 0.44 inch in diameter, while in the steel the corresponding holes are 0.5 inch in diameter. A 1.25 inch diameter beam hole through the entire array of detector material allowed for the passage of non-interacting beam particles.

# Chapter 3

# Event Reconstruction

We begin this chapter discussing briefly the scheme employed by E706 in the processing of triggered events. Starting with the data acquisition system, we proceed to a description of the event reconstruction packages. The chapter concludes with a more detailed presentation of the selection of events used in this analysis.

## 3.1 Data Acquisition

The FORTRAN code used by E706 for accumulating events from the experimental apparatus was written primarily by the Data Acquisition Software Group at Fermilab. This set of software packages, generally referred to as VAXONLINE [41], provides for the collection and combination of data from many sources. For E706/E672, these sources were four Front-End PDP-11 computers.

### 3.1.1 Front Ends

Each of the four Front-End machines executed a variety of specific tasks pertaining to the detector components for which they collected data. Three of the PDP-11s were used by E706 and the fourth by E672.

One of the PDP-11 micro computers accomplished the task of collecting the sub-event containing the LAC data from both the electromagnetic and hadronic calorimeters. This machine also executed jobs pertaining to the calibration of the calorimeter electronics.

A second PDP-11 computer was dedicated to the readout and diagnostics of the forward calorimeter. The third PDP-11 performed the same tasks for the tracking system. Each machine had one version or another of the RSX-DA running for the collection of sub-event data.

### 3.1.2 VAXONLINE

As a flexible and modular data acquisition system, VAXONLINE consists of numerous independent programs and software tools available as subroutine libraries. Central to the system is EVENT BUILDER. The primary task of this program is to collect the appropriate sub-events from each of the active Front Ends and concatenate them into a single event on the $\mu$VAX. These whole events are then transferred to the *event pool*, where BUFFER MANAGER assumes control. From the event pool, event copies may then be taken by OUTPUT for logging of data to tape or they may be selected (non-destructively) by any number of CONSUMER programs for

monitoring of the data-taking process.

The OUTPUT program provided for the logging of data to tape. It was configured in such a manner that no run extended over more than one tape, corresponding to approximately 11,000 events. While OUTPUT was capable of filling one tape in about ten minutes, E706 was writing to one tape about every twenty minutes.

The CONSUMER program provided a framework within which user-supplied event monitoring programs could be written. Many such CONSUMERs were running during the data-taking period to monitor as much of the hardware and data acquisition software as possible.

The E706 event display, using the DI-3000[1] graphics library, was also executing throughout the data-taking period as an online event monitor of the data-taking process. Selecting events from the online event pool, color displays of data in the entire E706 spectrometer (silicon strip planes, wire chambers and all three calorimeters) were possible. As a component of MAGIC (see section 3.2.1), the event display graphics allow the option of presenting raw data in addition to reconstructed results. It was possible, for example, to view *online* reconstructed tracks in the tracking system and reconstructed showers in the electromagnetic calorimeter.

Running on the $\mu$VAX and on each of the PDP-11s, RUN CONTROL coordinated and controlled the entire data-taking process. In addition to passing information to and from all Front Ends, RUN CONTROL commu-

[1] DI-3000 (Trademark) Precision Visuals Inc., Boulder, CO 80301

nicated with EVENT BUILDER and with OUTPUT. On the Front Ends, RUN CONTROL initiated many of the pre-run and post-run calibration and test procedures.

## 3.2 First Pass Analysis

The first pass analysis was performed with a program which controlled the reconstruction of the entire event from the E706 spectrometer. We will discuss briefly the various aspects of the event reconstruction in this section.

### 3.2.1 MAGIC and Event Reconstruction

As the overall reconstruction package for E706, MAGIC [3], provides a framework in which various subprograms such as unpackers and reconstructors for each detector exist. Additionally, it also handles many bookkeeping and organizational jobs such as controlling the number of events to process and all input and output of data. MAGIC has been written primarily in FORTRAN-77 and has run on the VAX, the AHMDAL, the ACP [5] system and Silicon Graphics machines at Fermilab. It has also successfully executed on many VAX systems at most of the universities within the E706 and E672 collaborations. The first pass analysis of the data presented in this thesis was analyzed with MAGIC running on the Fermilab ACP parallel computer system.

The unpacker routines convert the raw event data (as written by OUT-

PUT) into ZEBRA [12] banks[2] which are then passed to the individual reconstructors. Each reconstructor processes the event and places the results into ZEBRA output. These banks are then written to the ZEBRA output tapes. These ZEBRA tapes are then subsequently divided into a number of separate streams by another program called the SPLITTER. We will outline briefly the programs which performed the reconstruction of tracks (PLREC) and of electromagnetic showers (EMREC) followed by a discussion of the selection of the final event sample.

### 3.2.2 Tracking

The track reconstruction program (PLREC) used in this analysis was developed primarily by Sajan Easo and it is described completely in his thesis [16]. Here we will discuss the general scheme by which tracks and verticies were reconstructed.

Since the PWCs are constructed of sixteen planes in four independent views ($X$, $Y$, $U$ and $V$), PLREC began its task by forming three or four hit view tracks in each view. With the tracking SSDs consisting of eight planes in two independent views ($X$ and $Y$), the same view track finding code is used for finding view tracks in the SSD system. PLREC then correlated the PWC $X$ and $Y$ view tracks with $U$ and $V$ view tracks. When an $XY$ view track pair was found to match with a $UV$ pair, a *space* track was formed with a minimum requirement of thirteen hits.

[2] A ZEBRA *bank* is a specific structure within which data are stored.

Each accepted space track was required to have a minimum $\chi^2$ per degree of freedom of less than 3.0. Although tracks with large $\chi^2$ are likely to be fake, they were kept for subsequent study of the nature of these tracks. The distribution of $\chi^2$ for space tracks is shown in Figure 3.1 for tracks with different numbers of used hits. The hit multiplicities for space tracks is shown in Figure 3.2.

In order to calculate the momentum of a charged track, the track trajectory both before and after the magnet is required. After the PWC space tracks and the SSD view tracks were constructed, linking between the upstream and the downstream tracks at the magnet center was attempted. The accuracy of the linking was limited by a number of effects. First of all, the PWC track projected position uncertainty at the magnet center was about three times larger than that for the SSD tracks. This resulted in the possibility of linking a PWC track to the wrong SSD track. Since the SSD tracks were not highly constrained (requiring only 3 or 4 hits), there existed the very real possibility of linking to a fake SSD track. The linker first tried to match PWC space tracks to SSD tracks which were used in the vertex reconstruction. Failing that, other tracks were then used. The nearest SSD track could be no further away than 7 mm (about three sigma of the PWC track projection uncertainty at the magnet center). If no SSD track was found within this window, a line was drawn from the projected magnet point to the reconstructed vertex and the PWC track momentum was determined from this.

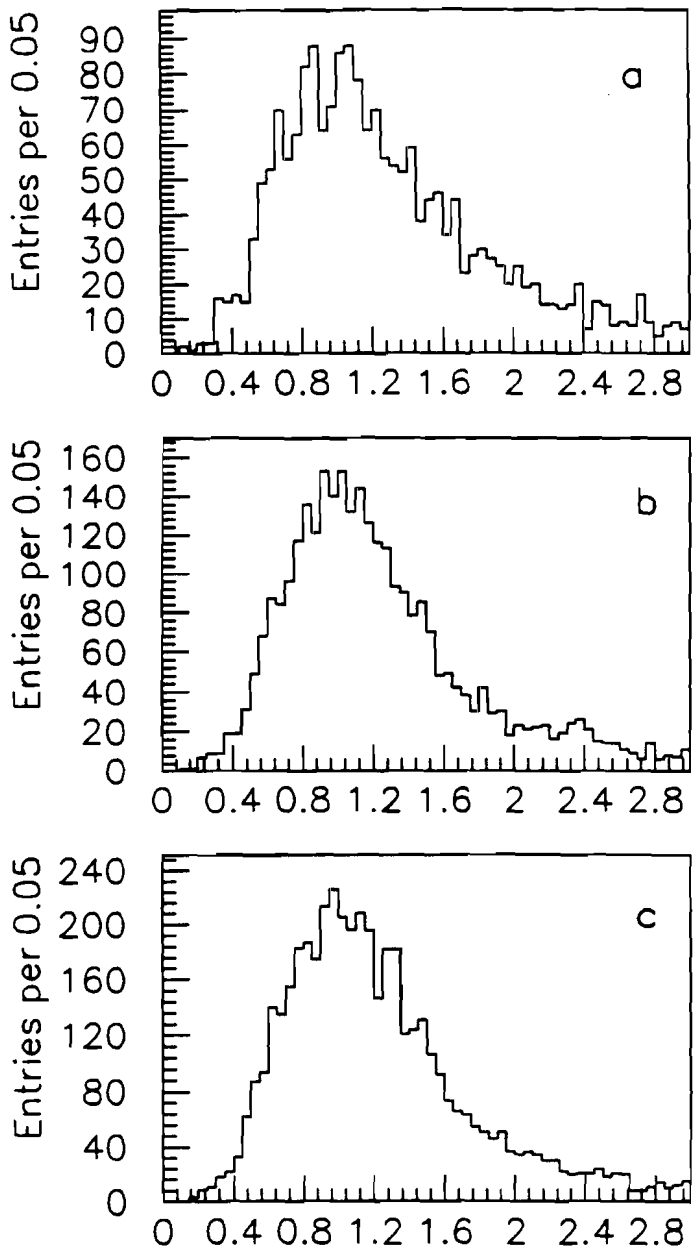


Figure 3.1: $\chi^2$ Per Degree of Freedom for PWC Space Tracks. (a) fourteen hit (b) fifteen hit and (c) sixteen hit tracks. A track was accepted as a space track if $\chi^2/DOF \leq 3.0$.

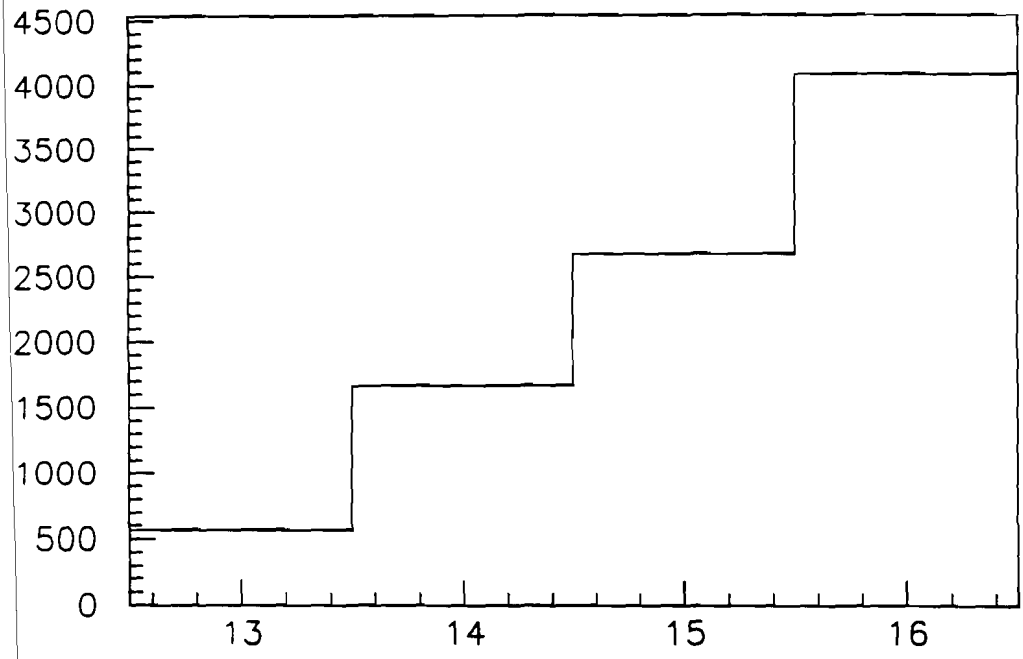


Figure 3.2: Number of Points Used in PWC Space Tracks

Vertices were reconstructed using the SSD view tracks first in the X-view and then in the Y-view. A Z-position was obtained in each view and a cut was applied to the difference in these two numbers. The final Z-position was given as the weighted average of the two independent numbers.

As evidence for the successful performance of the tracking system we present plots of a variety of massive states decaying into charged tracks. First we show invariant mass distributions of states decaying into hadrons. Figure 3.3 shows the mass plots for the $K^0$, $\Lambda^0$ and $\overline{\Lambda^0}$. Although the $K^0$ signal has also been observed in the SSD system, these plots are were made exclusively from PWC system information. They were selected from pairs of oppositely charged tracks which intersect upstream of the spectrometer magnet but downstream of the SSDs.

In conjunction with the electromagnetic calorimeter, electrons may be selected and a search for particles with electrons as decay products may be performed. In particular, some fraction of the photons arising from the decay of a $\pi^0$ will convert into a pair of electrons. These electrons are easily identified and the invariant mass for the combinations of $e^+e^-\gamma$ is shown in Figure 3.4a. Figure 3.4b shows this scheme taken one step further: the $e^+e^-e^+e^-$ invariant mass distribution. In each plot, the $\pi^0$ signal is clearly visible. In fact, the signal for the $\eta$ is visible in the $e^+e^-\gamma$ distribution.

Next we show the $e^+e^-$ mass distribution in Figure 3.5. The cuts applied to this distribution were as follows:

- Select all events with a pair of oppositely charged tracks.

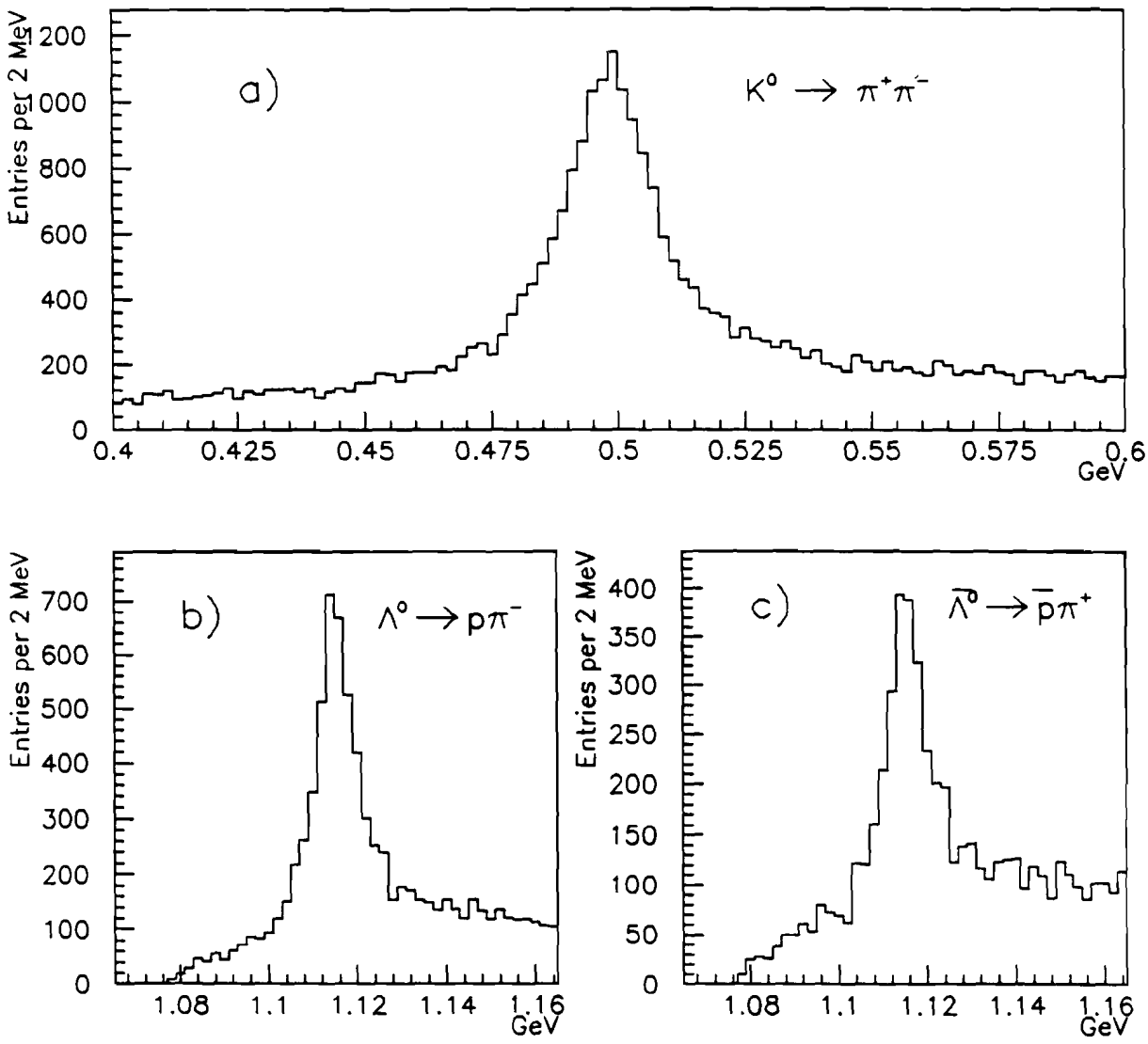


Figure 3.3: $\pi^+\pi^-$, $p\pi^-$ and $\overline{p}\pi^+$ Mass Distributions. (a) $K^0 \rightarrow \pi^-\pi^-$, (b) $\Lambda^0 \rightarrow p\pi^-$ and (c) $\overline{\Lambda^0} \rightarrow \overline{p}\pi^-$.

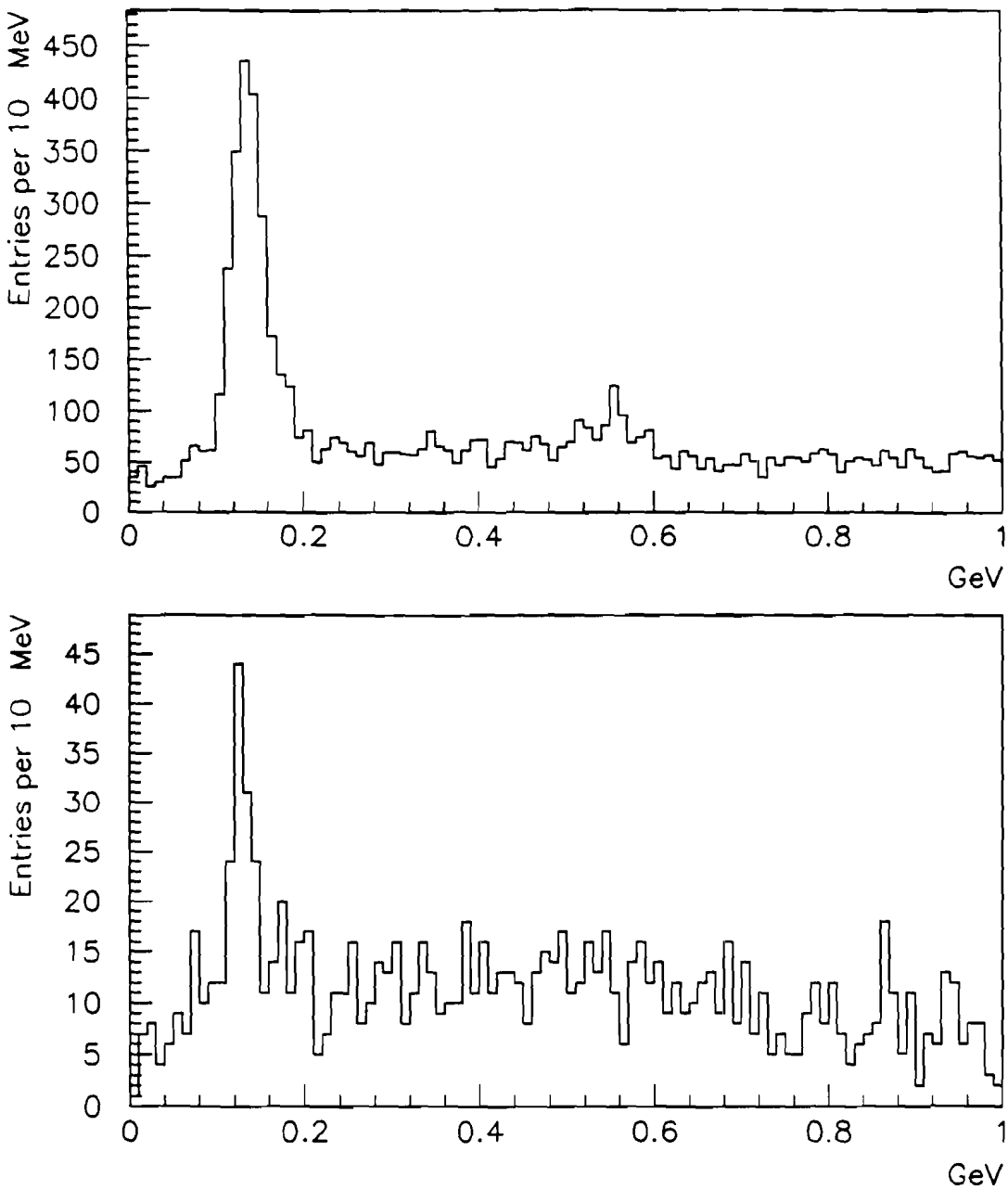


Figure 3.4: $\pi^0$s and $\eta$'s from Photon Conversions. (a) $e^+e^-\gamma$ and (b) $e^-e^-e^+e^-$ Mass Distributions.

- Require that each track match with a LAC shower within 1 cm.
- At least 70% of each shower's energy must be in the front of the EMLAC.
- Track momentum and shower energy to agree within 30%.
- Eliminate any electrons which obviously arise from photon conversions (apply ZMP cuts, see Chapter 4).
- At least one of the showers must have the highest $p_T$ in a trigger octant (see Section 3.3.

The first four cuts simply select electrons; the last two are required to reduce further the background of electrons arising from the conversion of photons. As shown in Figure 3.5, a clear signal for the $J/\psi$ (at 3.1 GeV) is visible. It was hoped that this signal would have have triggered the LAC two-gamma trigger but the unexpectedly high threshold of the pre-trigger prevented this (see Section 3.3.

### 3.2.3 PLREC Efficiency

We have used two schemes to estimate the efficiency of the tracking program. The first scheme, *Scheme 1* is described in detail elsewhere [16], will be summarized here. It consists of removing one PWC plane from the PLREC algorithm and reconstructing tracks with the remaining planes. The efficiency is calculated as the ratio of two numbers N/D; where N equals the number of times a 15-hit track, when projected to the plane left out,

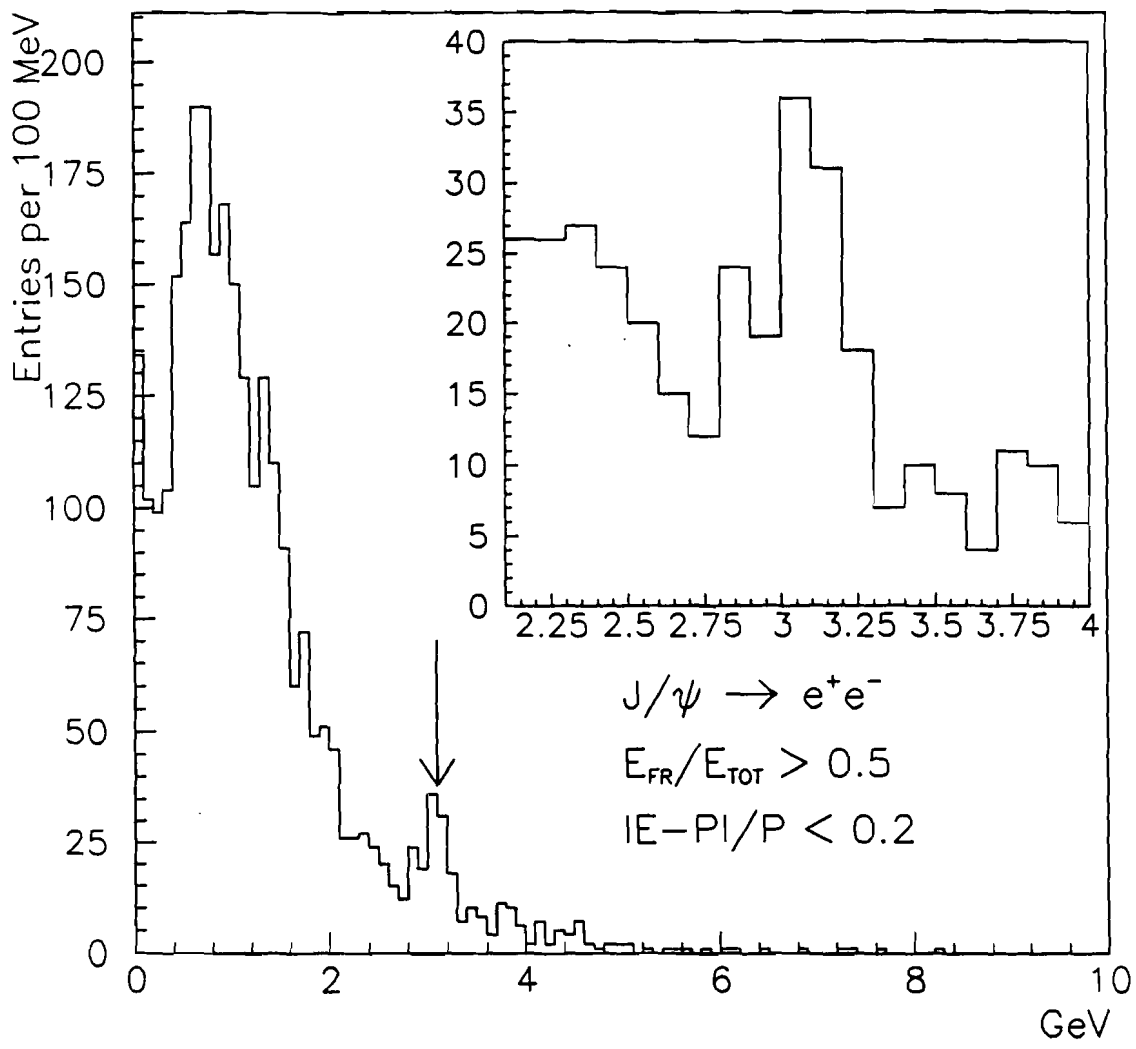


Figure 3.5: $e^+e^-$ Mass Distribution. The standard $J/\psi$ mass is indicated by the arrow. The inset shows the same distribution over a more constrained mass range using the same bin size.

finds a hit: D equals the number of tracks used in the test. This is a measure of the efficiency of the PWC planes. The numbers are reported in Table 2.6.

Alternatively, *Scheme 2* is also a measure of the efficiency of the PWC planes but it employs a much simpler technique since it does not require rerunning the reconstruction program. This scheme simply takes a reconstructed PWC space track and calculates the ratio N/D; where N equals the number of times a specific plane was used for the track; D equals the number of tracks used in the test. These results are also presented in Table 2.6.

### 3.2.4 Electromagnetic Showers

Showers in the electromagnetic calorimeter were reconstructed with the program called EMREC. This software was written by a number of authors [19, 9, 28] over a rather long period of time. We will present a short description of its algorithm here and refer the reader to the previous references for details.

Physically, the electromagnetic calorimeter is divided into four distinct quadrants and each quadrant is divided longitudinally into front and back sections. Within each quadrant, the EMLAC copper-clad *G-10* readout boards span one octant. As a result, EMREC operates on each quadrant independently, dividing them into four separate *views*: $r$-right, $r$-left, $\phi$-inner and $\phi$-outer.

For the correlation of showers between different views, the strip energies in the front and back sections were summed. The EMREC algorithm first makes a discrimination between energy which is likely to originate from a

true electromagnetic shower and that which is likely to be from noise. A *group* is formed from a set of contiguous strips each with a minimum of 150 $MeV$, with at least one strip having 300 $MeV$ and the group sum being greater than 750 $MeV$. A search for groups is made in each of the four separate views.

The groups are then tested for the appropriate electromagnetic shower shape and defined to be either an $r$–gamma or a $\phi$–gamma. The gammas are then correlated by energy and declared to be *photons*. The total energy of the photon is the sum of the correlated $r$–gamma and $\phi$–gamma.

## 3.3 General Trigger Considerations

In order to study the structure of events containing particles with high $p_T$, some sort of scheme must be devised to trigger on these events. Toward this end, E706 has produced a trigger which tends to select high $p_T$ electromagnetic showers. In this section, a simplified discussion of the E706 trigger will be presented. A more detailed description of this system has been reported in its entirety elsewhere [44].

The E706 trigger will be described in terms of two separate components: 1) the beam component and 2) the LAC component. The beam component, discussed in the previous section, consists of signals originating primarily from a variety of scintillation counters. These signals are counted, or *scaled*, and written to tape along with the rest of the event. The LAC component of the trigger originates from energy deposition in the EMLAC.

Before we can discuss the LAC trigger, we must first cover a few definitions. As mentioned above, muons may accompany beam particles along the beam line and generate showers which look like high $p_T$ electromagnetic showers which cause a trigger. The muon wall was built to veto events in which one of these halo muons was observed to coincide, in time, with an event. The muon veto wall is an array of scintillation counters upstream of the target and downstream of the hadron absorber (see Figure 2.1) designed to veto events in which a muon accompanies a beam particle.

The SCRKILL signal indicated noise from the 400 Hz low voltage power supplies for the LAC amplifiers in the Faraday Room.

When a previous event occurred within 300 ns of the current event and the residual energy from that event corresponded to an octant global $p_T \geq$ 1.5 GeV, an early transverse momentum (EARLYPT) signal was generated for that octant.

The trigger $p_T$ was calculated from the energy deposited in the radial strips of the EMLAC as follows:

$$p_T(trigger) = \frac{2}{Z_{LAC}} \sum E_i r_i. \tag{3.1}$$

The sum is taken over all strips with signal above threshold, $Z_{LAC}$ is the z-position of the front face of the EMLAC, $E_i$ is the energy in r-strip $r_i$. The factor of two comes from the assumption that half the energy is deposited into the r-strips and half in the $\phi$-strips; for triggering purposes, only the r-strips are used. Figure 2.6 shows the readout structure where the r-strips

are on the R-Board and $\phi$-strips on the PHI-Board.

The LAC component of the trigger consists of a global[3] pre-trigger and combinations of global and local trigger signals. In terms of the pre-trigger, each octant was further divided into two radial regions at a distance of 74.4 cm from the LAC center. The inner region (radial strips 1–96) consisted of $p_T$ modules 1, 2 and 3 while the outer region (radial strips 97–224) consisted of modules 4–7; $p_T$ module 8 was not used for triggering.

### 3.3.1 Beam Determination

To determine the cross section for any particular process, we need to know the number of beam particles which could have produced an interaction and we need to know the behavior of our trigger. We will begin with a list of definitions in hopes of making the subsequent discussions more understandable.

The bottom line in the determination of the incident beam is the quantity referred to as *live triggerable beam* (LTB). The LTB is the number of incident beam particles which hit the target when the entire experimental system was ready. A more technical definition of LTB will follow a few definitions.

The beam scintillation counters BA, BB and BH are used to define the beam where BA and BB are both square pieces of scintillator 2.54 cm on a side while BH is square with 12.7 cm sides and a central 0.95 cm hole.

[3] *Global* in the context of the trigger refers to the physical boundaries defining an *octant*.

All three counters are centered on the beam where BA and BB are used to identify a beam particle and BH is used to identify a beam halo particle.

A triggerable beam particle is said to have entered the spectrometer target if each of BA and BB has a signal in conjunction with a pair of signals originating from the main accelerator control. One signal, called *beam gate* (BMGATE) indicates the begin of the beam spill[4]. Since the BMGATE signal is ON until the *end of spill* (ENDSP) signal is received from the accelerator control, it has a frequency of about 1/60 Hz and a width of about 23 seconds. The other signal, RF_CLOCK, from the accelerator is that which corresponds to the radio frequency ($\sim$ 52 MHz) beam buckets and it has a width of 10 ns. We may now define a beam particle: [5]

$$BM \equiv BA \otimes BB \otimes BMGATE \otimes RF_CLOCK$$

The interaction counters SE1, SW1, SE2 and SW2 were used to indicate an interaction in the system (see Figure 2.1). The interaction counters are square pieces of plexiglass with a semi-circular hole centered on the edge near the beam. The upstream counters (SE1 and SE2) are 15.2 cm on a side with a 0.95 cm diameter beam hole while the downstream counters (SE2 and SW2) are 20.3 cm on a side with a 1.75 cm diameter beam hole. The

[4]The actual signal from the accelerator control is the *begin spill* (BEGSP) signal; the BMGATE signal is turned ON 100 milliseconds after the BEGSP signal.

[5]In many of the following definitions, we will use the binary symbols $\oplus$ and $\otimes$ to indicate the logical .OR. and the logical .AND., respectively. We will also use the overline to indicate the logical equivalent of .NOT.

counters SE1 and SE2 are located on the east side of the beamline while SW1 and SW2 are on the west. An interaction is defined as a signal in any of the four interaction counters in conjunction with a BM signal:

$$INT \equiv BM \otimes (SE1 \oplus SW1 \oplus SE2 \oplus SW2)$$

The interaction signal was sent through a sequence of delay circuits, one for every beam bucket. Each delay circuit produced an output corresponding to the status of the interaction definition for that beam bucket time slice. With this scheme, a history of interaction definitions was saved for the buckets immediately before and after a trigger interaction, which allowed us to avoid events occurring too closely in time. All events with another interaction within $\pm$ 3 buckets ($= \pm 60ns$) were rejected. Two signals which indicated this interaction history were generated: CLEAN_EARLY and CLEAN_LATE. We define the single *clean* signal as:

$$CLN \equiv CLEAN_EARLY \otimes CLEAN_LATE$$

When an event was accepted by the system, it was then written to tape. During this process, the computer system was busy and hence unable to write subsequent events to tape. When the computer system was again ready to take data, the system is said to be *live* and a computer ready signal is generated (CMPRDY). The final interaction signal definition is:

$$LIVE_INT1 \equiv INT \otimes \overline{BH} \otimes CMPRDY \otimes CLN.$$

With the CMPRDY signal we may also define a live beam signal:

$$LIVE_BM \equiv BM \otimes \overline{BH} \otimes CMPRDY.$$

With this we are now be able to define the live triggerable beam:

$$LTB \equiv BM \otimes \overline{BH} \otimes CMPRDY \times C_1 C_2 C_3 C_4 \tag{3.2}$$

where the $C_i$ are corrections to the live beam number which we will now describe.

As previously mentioned, only events which were defined as clean within $\pm$ 60 ns were used. The correction for this requirement is $C_1$ and can be measured from quantities scaled and written to tape for each spill:

$$C_1 = \frac{LIVE_INT \otimes CLN}{LIVE_INT}.$$

This constraint requires a correction which was typically $C_1 \geq 0.995$.

The LIVE_INT1 signal defined above was transmitted to the LAC trigger hardware in the Faraday Room (FR) from the upstream Latch House (LH). On occasion, this signal was lost in transmission or a fake signal was generated. The correction for lost LIVE_INT signals is given by:

$$C_2 = \frac{LIVE_INT1(FR)}{LIVE_INT1(LH)}.$$

Since this was a rather infrequent problem, $C_2 \simeq 0.99$. When an interaction signal *was* observed in the Faraday Room and *not* at its point of origin in the Latch House, the run was not used. This class of events corresponds to about ten out of about 500 runs.

The corrections $C_3$ and $C_4$ originate from cuts made on the trigger signal as generated from the LAC. We will describe these corrections here and define the terminology in the next section. The decision-making process of the LAC pretrigger hardware requires a finite amount of time during which we are counting beam particles. This is referred to as the *pretrigger live time* and its correction is measured by $C_3$:

$$C_3 = \frac{PRETRIG \ominus \overline{PRETRIG}}{LIVE_INT1},$$

and has a correction $C_3 \simeq 0.97$.

Three sources of false trigger signals were observed in the LAC: a) high energy muons accompanying the beam particles (VW), b) coherent noise signals generated by the high frequency low voltage power supplies in the Faraday Room (SCRKILL) and c) residual LAC energy from an earlier event (EARLYPT). The correction for these situations was the largest of the four corrections and it was measured as $C_4$:

$$C_4 = 1 - \frac{GINT1 \otimes (VW \oplus \overline{SCRKILL} \oplus \overline{EARLYPT})}{GINT1},$$

with a typical value of $\simeq 0.83$. GINT1 in this expression is the same as LIVE_INT1 with the additional constraint that the LAC trigger electronics have been allowed to settle down for some period of time.

### 3.3.2 Pre-Trigger

The pre-trigger is defined by the coincidence of the following:

- deposition of $p_T \sim 1.8$ GeV in either radial region of any octant.

- Live interaction signal: LINT1.
- no signal in the veto wall ($\overline{VW}$).
- no coherent power supply noise ($\overline{SCRKILL}$).
- $p_T \leq 1.5\ GeV$ in the entire octant in preceding 300 ns ($\overline{EARLYPT}$).

A final LAC pretrigger was generated from the logical .OR. of the sixteen individual octant pre-triggers. This LAC pre-trigger was then directed to each of the four final LAC triggers.

To minimize the effects of coherent noise and of low $p_T$ multiphoton events, a local $p_T$ requirement was made on LAC triggers. Two signal thresholds were employed: a local $p_T$ low and a local $p_T$ high. The locality of a shower was defined as within a region of sixteen radial strips within a single octant in the EMLAC. Electromagnetic showers are found to be contained within this local region. Similarly, a pair of global $p_T$ thresholds were implemented against which global signals were discriminated.

Within these two regional $p_T$ definitions (local and global) and the two threshold levels (low and high) four LAC triggers were employed and they are defined as follows:

**LOCAL⊗GLOBAL–HIGH (LGH)** a LAC signal which simultaneously exceeds the lower local $p_T$ threshold and the higher global $p_T$ threshold in a single octant.

**LOCAL⊗GLOBAL–LOW (LGL)** a LAC signal which simultaneously exceeds the lower local $p_T$ threshold and the lower global $p_T$ threshold

in a single octant.

**SINGLE LOCAL (SL)** a LAC signal which exceeds the higher local $p_T$ threshold.

**TWO GAMMA (TG)** a LAC signal which simultaneously exceeds the lower local $p_T$ threshold in two distinct octants. The octant pair must be separated by at least two octants (90 degrees in azimuth).

Since the analysis in this thesis was performed on events triggered using the two-gamma trigger, we will discuss no further the other LAC triggers [44].

### 3.3.3 Data Compression

The data analyzed in this thesis were recorded as being triggered by the E706 TWO GAMMA trigger. These events occurred at a rate of about 5 % of all other triggered events. The SPLITTER program separated these events into a separate stream of pure TWO GAMMA events, resulting in a compression by a factor of twenty in the number of these events on a tape. Other streams were generated by the SPLITTER (e.g. ZMP stream, MEP stream, and many others), but we will be concerned here only with the TWO GAMMA stream.

The data on the split TWO GAMMA tapes were still in the MAGIC format which included the raw data in addition to reconstruction results. For the second pass analysis, the raw data were unnecessary and a subsequent

compression of the data was performed for the final DST format. Only the final results of the reconstructors were written to these tapes, resulting in an additional compression factor of approximately twenty.

## 3.4 The TWO GAMMA Trigger

The TWO GAMMA (TG) is a very specialized trigger designed to trigger on the simultaneous deposition of high $p_T$ electromagnetic energy into two local regions of the EMLAC separated by at least 90 degrees in the azimuthal angle (see Figure 3.6). The general features of the trigger were described in the previous section. With this definition, there are twelve distinct octant combinations available, when all octants are operating, see Table 3.1.

Table 3.1: Possible Two-Gamma Trigger Combinations. There are twelve possible combinations: four directly opposite and eight adjacent-opposite.

| | | | | |
|---|---|---|---|---|
| Directly Opposite | 1–5 | 2–6 | 3–7 | 4–8 |
| Adjacent–Opposite | 1–4 | 1–6 | 2–5 | 2–7 |
| | 3–6 | 3–8 | 4–7 | 5–8 |

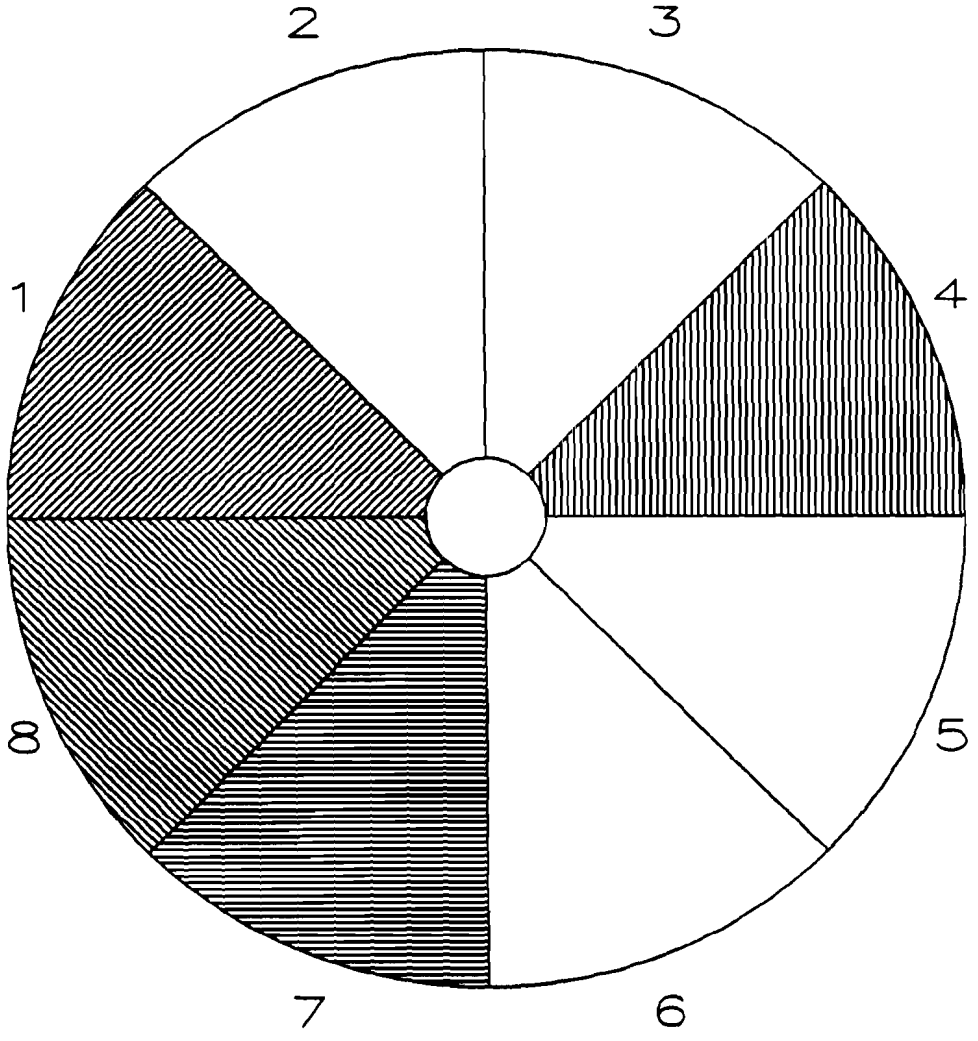


Figure 3.6: Allowable Orientation of the Two-Gamma trigger. There are twelve distinct octant-pair combinations possible; see Table 3.1.

### 3.4.1 Performance

The TG trigger performed rather well during the 1987-1988 data-taking run. Most of the time all eight octants were working at about the same rate. On occasion, though, one or more octants were experiencing some sort of difficulty. These periods are shown in Figure 3.7. From these plots, the problem runs are displayed rather clearly. In particular, Figure 3.7c shows the number of inactive octants on a run-by-run basis. A large part of the Set E data show a consistent problem with at least one octant. During this time, octants 5 and 8 were having problems and the correction for this set of data is discussed in the section on acceptance.

Another indication of the performance of the TG trigger is given by the plots in Figure 3.8 and Figure 3.9. The overall frequency of octant triggers is quite uniform over the entire period of running.

### 3.4.2 Efficiency

A typical method for determining the efficiency of the turn-on of a trigger threshold is to use another trigger with a lower threshold which has already completely turned on. Since the two-gamma trigger already has the lowest threshold in the experiment, such a scheme is not available to us. An alternative approach is to measure the $p_T$ spectrum of $\pi^0$s (the most likely objects to cause a trigger in E706) and make a fit of the form used in previous $\pi^0$ production experiments. In particular, we have made a fit to the form:

Table 3.2: Run Statistics. The data were divided into five chronological units; the number of TWO-GAMMA triggered events (TG Events) are in thousands. The year of the dates is 1988.

| Set Label | A | B | C | D | E |
|---|---|---|---|---|---|
| Beam | $-$ | $-$ | $-$ | $-$ | $-$ |
| Target | Cu+Be | Cu+Be | Cu+Be | Be | Be |
| Dates | 9-15 Feb | 30 Jan-1 Feb | 25-30 Jan | 16-25 Jan | 4-13 Jan |
| # Runs | 95 | 53 | 141 | 162 | 162 |
| TG Events | 23.0 | 25.6 | 46.2 | 45.1 | 53.6 |

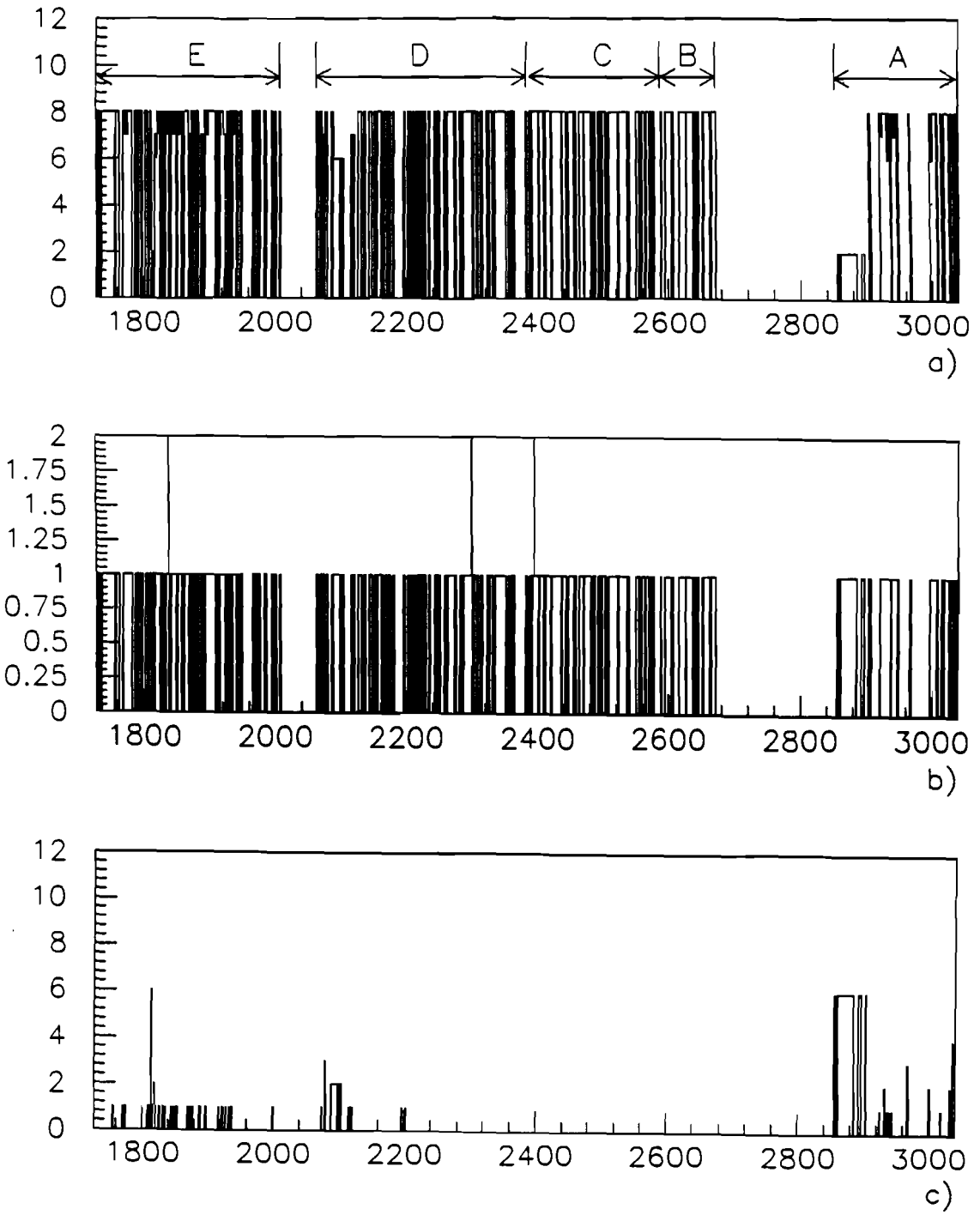


Figure 3.7: Octant Activity in the Two-Gamma Trigger. a), number of active octants vs run number; b), data tape runs; c), number of *inactive* octants per run. The letters A–E correspond to running periods described in Table 3.2.

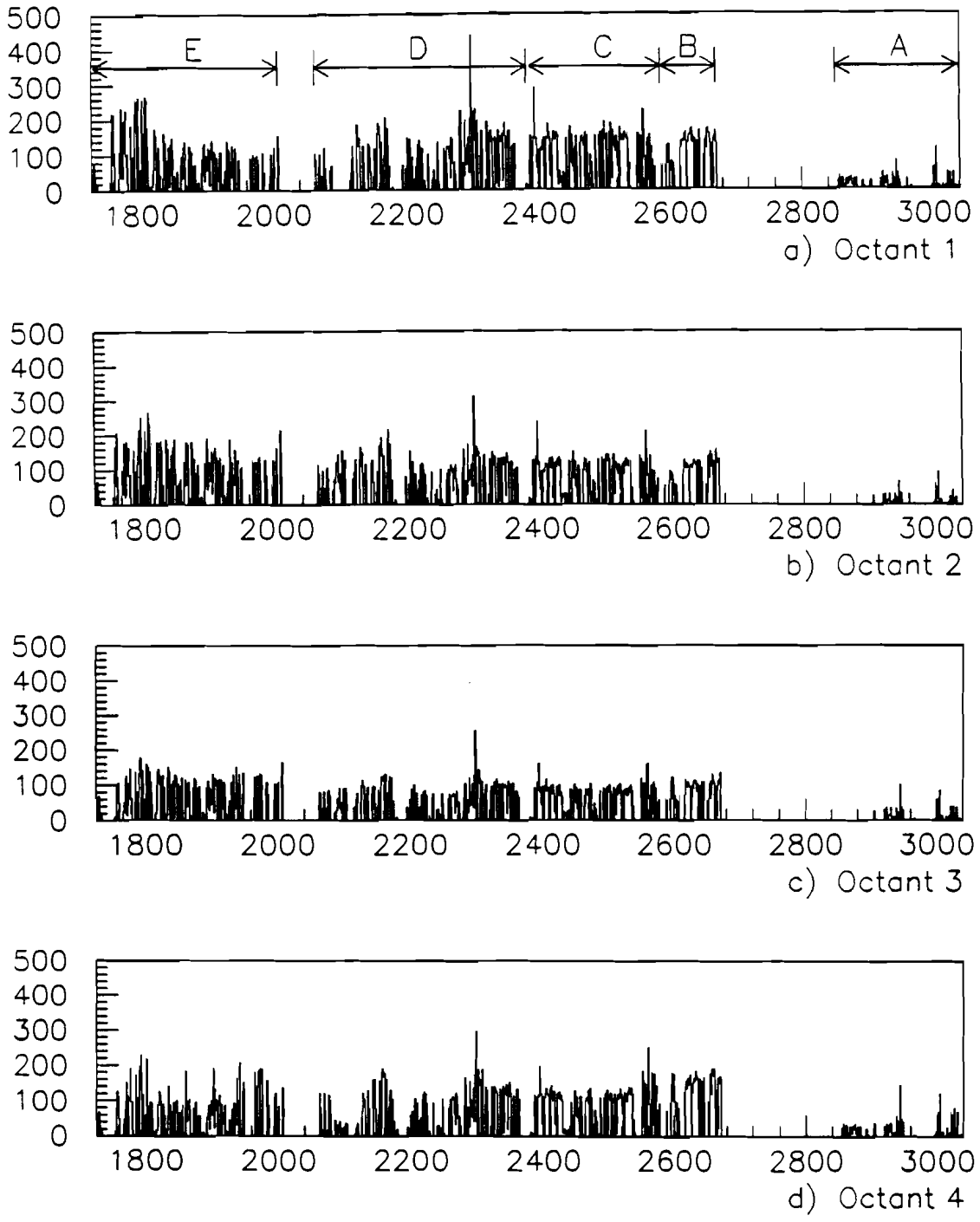


Figure 3.8: Octant (1–4) Frequency in the Two–Gamma Trigger. Octants 1 through 4 are shown in a through d, respectively. The letters A–E correspond to running periods described in Table 3.2.

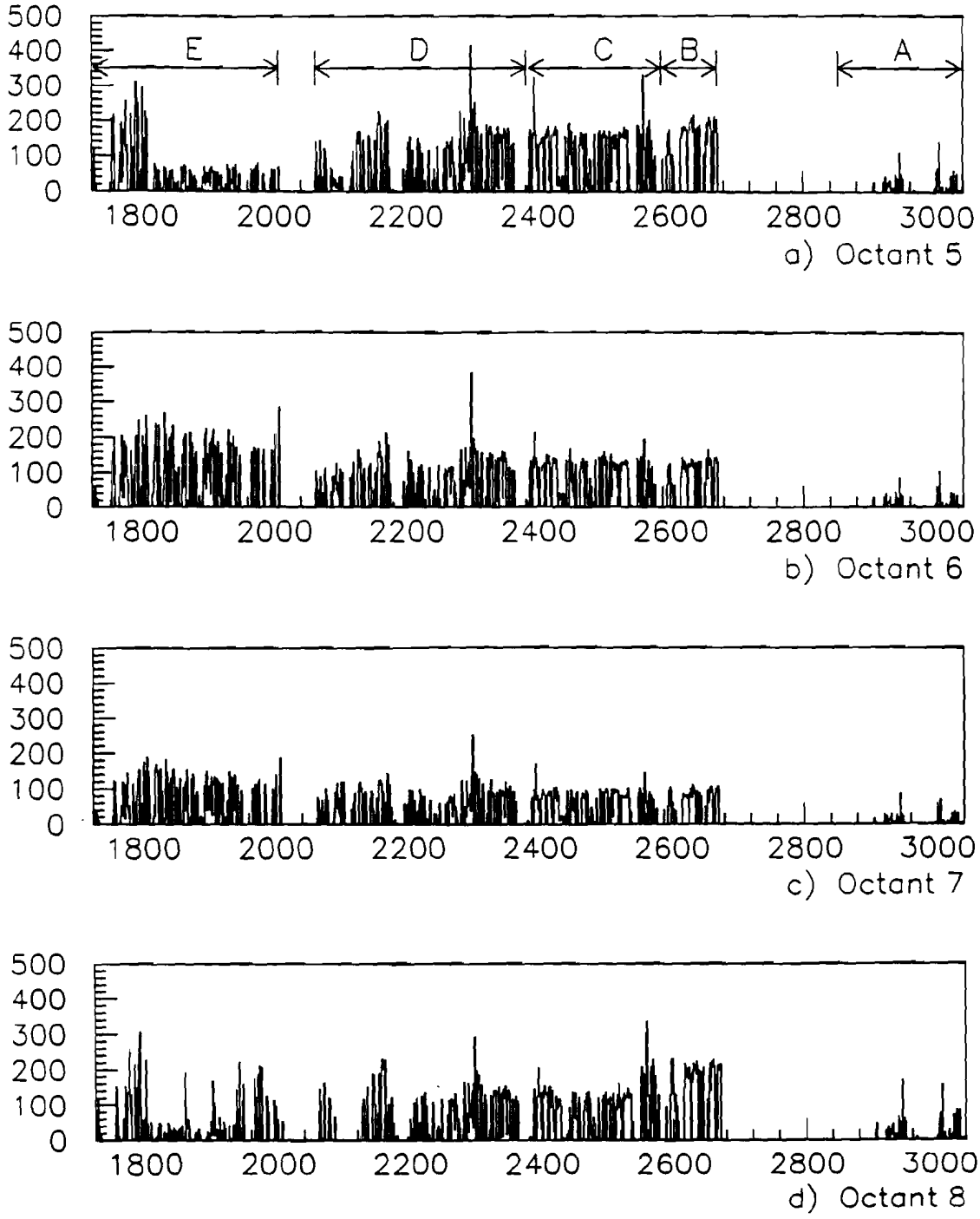


Figure 3.9: Octant (5–8) Frequency in the Two-Gamma Trigger. Octants 5 through 8 are shown in a through d, respectively. The letters A–E correspond to running periods described in Table 3.2.

$$\frac{dn(\pi^0)}{dp_T} = A \times (1 - x_R)^m \times p_T^n \times erf(\tau, \sigma) \tag{3.3}$$

where

$$x_R = (x_T^2 - (\overline{x_F} - x_0)^2)^{1/2}$$

$$x_T = \frac{2p_T}{\sqrt{s}} \qquad x_F = \frac{2p_z}{\sqrt{s}}.$$

The error function, $erf(x)$ is defined as:

$$erf(x) = \frac{2}{\pi}\int_0^x e^{-t^2}\,dt$$

where for our application, we have made the substitution $x = \tau/\sigma$. The parameters $m$, $n$ and $x_0$ were allowed to float in the fits. The error function supplied the simulation of the trigger turn-on where $\tau$ is the threshold and $\sigma$ is the width of the Gaussian function inside the integral. In practice, a ten parameter Chebyshev fit to the error function was used [34, section 6.2]. The quantity $\overline{x}_F$ is the mean value of $x_F$ in the given rapidity interval.

Initially, fits were made to the $p_T$ spectra in four different regions of the electromagnetic calorimeter using the form of Equation 3.3. Although these regions were selected in terms of rapidity, they closely follow physical boundaries of the $p_T$ modules of the detector. They are:

- $-1.0 \leq Y_{CM} < -0.3$; this region corresponds approximately to $p_T$ modules 4–7 ranging from $74.4\ cm \leq r_{LAB} < 144.8\ cm$
- $-0.3 \leq Y_{CM} < 0.0$; this region corresponds approximately to $p_T$ module 3 ranging from $56.5\ cm \leq r_{LAB} < 74.4\ cm$

- $0.0 \leq Y_{CM} < 0.3$; this region corresponds approximately to $p_T$ module 2 ranging from 38.9 $cm \leq r_{LAB} < 56.5\ cm$

- $0.3 \leq Y_{CM} < 0.9$; this region corresponds approximately to $p_T$ module 1 ranging from 21.6 $cm \leq r_{LAB} < 38.9\ cm$.

The initial $\chi^2$ minimization fits were performed for each of the above rapidity intervals and averaged over all azimuthal angles. Values for A, $x_0$, m and n were obtained for each region, and they are given in Table 3.3. The data on which the fits were applied and the $\chi_2$ minimized curves are shown in Figure 3.10.

Given the parameters of these fits, we then fix $x_0$, m and n allowing A, $\tau$ and $\sigma$ to float and separate the data into the eight octant regions. The results of these fits are given in Tables 3.4 and 3.5.

The numbers in Tables 3.4 and 3.5 were used as effective trigger thresholds and trigger widths in determining the effective efficiency for the two-gamma trigger. A plot of the error function with the obtained values for $\tau$ and $\sigma$ for a typical octant (octant 6) for the four different rapidity regions is shown in Figure 3.11.

### 3.4.3 Two-Gamma Trigger Acceptance Issues

When one octant is missing, the overall trigger acceptance decreases by 3/12 and the corresponding correction is 1/(1-3/12) = 4/3. When two octants are not operating, we have two situations possible: 1) the two octants are such that they could not both be part of the same trigger (e.g. adjacent

Table 3.3: Fit Parameters to Azimuthally Averaged $\pi^0$ $p_T$ Spectra. The fits are defined by Equation 3.3 and were made to the background subtracted. $\pi^0$ $p_T$ spectra (not corrected for acceptance) as observed in the two–gamma trigger. The regions are rapidity intervals as described in the text. The data are shown in Figure 3.10

| Region | $x_0$ | m | n |
|---|---|---|---|
| 1 | $0.09 \pm 0.05$ | $3.8 \pm 3.1$ | $-6.8 \pm 1.1$ |
| 2 | $0.18 \pm 0.06$ | $10.2 \pm 2.1$ | $-3.5 \pm 0.6$ |
| 3 | $0.19 \pm 0.01$ | $11.4 \pm 1.4$ | $-3.3 \pm 0.3$ |
| 4 | $0.12 \pm 0.02$ | $7.5 \pm 0.2$ | $-4.46 \pm 0.03$ |

| Region | $\tau$ | $\sigma$ | $\chi_2$/dof |
|---|---|---|---|
| 1 | $3.1 \pm 0.6$ | $0.7 \pm 0.2$ | 1.7 |
| 2 | $2.17 \pm 0.05$ | $0.51 \pm 0.02$ | 1.3 |
| 3 | $1.93 \pm 0.02$ | $0.40 \pm 0.01$ | 1.3 |
| 4 | $2.04 \pm 0.01$ | $0.36 \pm 0.01$ | 1.6 |

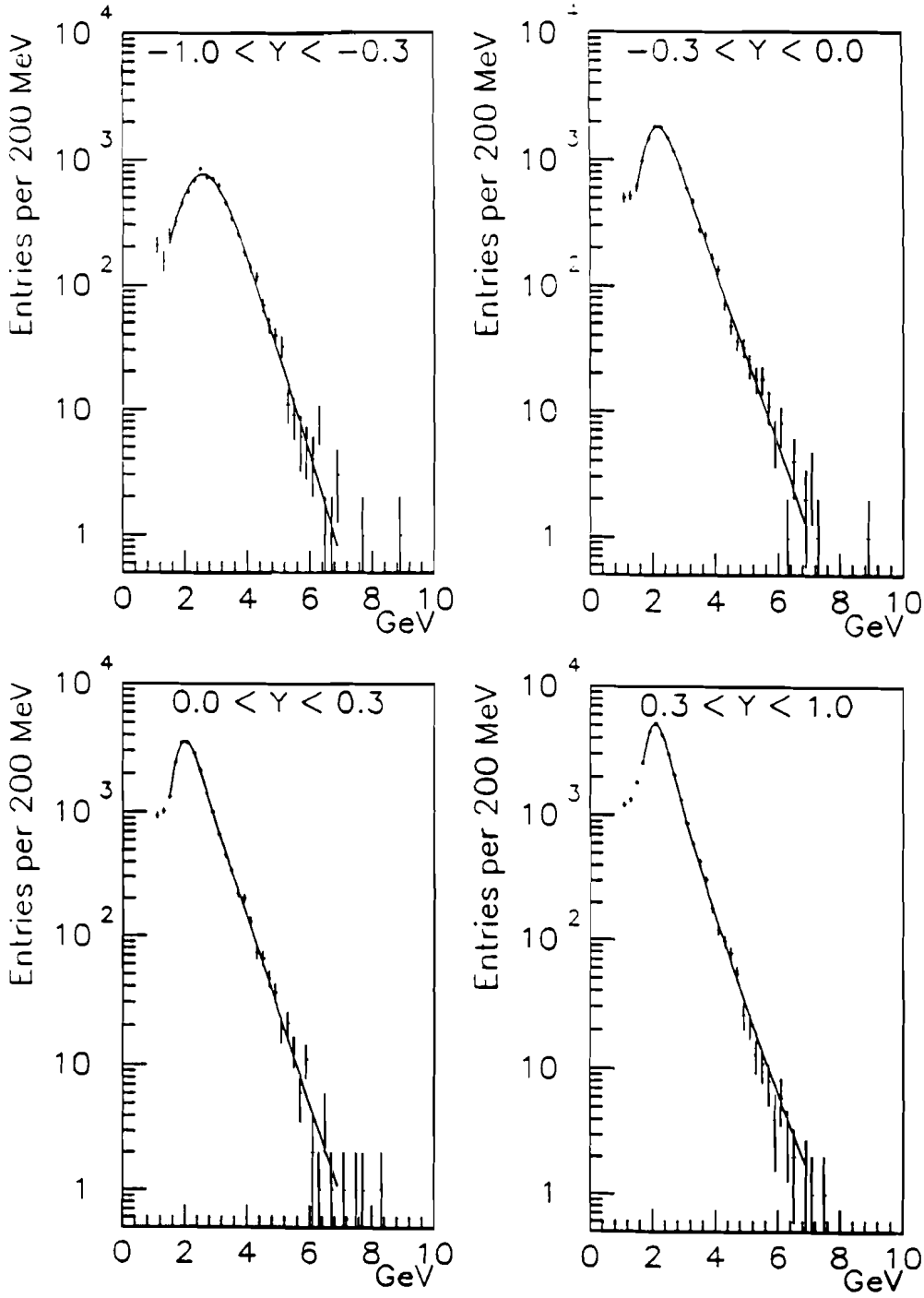


Figure 3.10: Fits to Uncorrected $p_T$ Spectra for Single $\pi^0$s. Details of the fits are given in the text.

Table 3.4: Fit Parameters to Single $\pi^0$ $p_T$ Spectra for Octants 1–4. The four regions (1–4) are rapidity intervals as described in the text, $\tau$ is the effective trigger threshold, $\sigma$ the effective width of the trigger turn-on. All fits used about thirty points.

| Octant | Region | $\tau$ | $\sigma$ | $\chi^2$/dof |
|---|---|---|---|---|
| 1 | 1 | $3.01 \pm 0.06$ | $0.69 \pm 0.03$ | 0.9 |
| 1 | 2 | $2.20 \pm 0.04$ | $0.51 \pm 0.03$ | 1.1 |
| 1 | 3 | $2.00 \pm 0.02$ | $0.44 \pm 0.02$ | 0.9 |
| 1 | 4 | $2.06 \pm 0.01$ | $0.32 \pm 0.02$ | 1.4 |
| 2 | 1 | $3.02 \pm 0.06$ | $0.71 \pm 0.03$ | 1.1 |
| 2 | 2 | $2.34 \pm 0.04$ | $0.52 \pm 0.03$ | 1.3 |
| 2 | 3 | $2.03 \pm 0.02$ | $0.43 \pm 0.02$ | 1.0 |
| 2 | 4 | $1.98 \pm 0.01$ | $0.27 \pm 0.02$ | 1.0 |
| 3 | 1 | $3.20 \pm 0.06$ | $0.72 \pm 0.03$ | 1.1 |
| 3 | 2 | $2.45 \pm 0.04$ | $0.55 \pm 0.03$ | 1.1 |
| 3 | 3 | $2.05 \pm 0.01$ | $0.43 \pm 0.01$ | 1.3 |
| 3 | 4 | $2.03 \pm 0.02$ | $0.42 \pm 0.02$ | 1.9 |
| 4 | 1 | $3.08 \pm 0.07$ | $0.70 \pm 0.04$ | 1.5 |
| 4 | 2 | $2.18 \pm 0.03$ | $0.48 \pm 0.03$ | 0.8 |
| 4 | 3 | $2.04 \pm 0.02$ | $0.39 \pm 0.02$ | 1.4 |
| 4 | 4 | $1.91 \pm 0.01$ | $0.30 \pm 0.02$ | 1.0 |

Table 3.5: Fit parameters to single $\pi^0$ $p_T$ spectra for octants 5–8. The four regions (1–4) are rapidity intervals as described in the text, $\tau$ is the effective trigger threshold, $\sigma$ the effective width of the trigger turn-on. All fits used about thirty points.

| Octant | Region | $\tau$ | $\sigma$ | $\chi^2$/dof |
|---|---|---|---|---|
| 5 | 1 | $2.95 \pm 0.06$ | $0.71 \pm 0.03$ | 0.6 |
| 5 | 2 | $2.14 \pm 0.03$ | $0.50 \pm 0.03$ | 1.2 |
| 5 | 3 | $1.90 \pm 0.03$ | $0.38 \pm 0.03$ | 1.1 |
| 5 | 4 | $2.05 \pm 0.01$ | $0.32 \pm 0.02$ | 0.9 |
| 6 | 1 | $2.94 \pm 0.05$ | $0.65 \pm 0.03$ | 1.0 |
| 6 | 2 | $2.24 \pm 0.03$ | $0.51 \pm 0.03$ | 1.0 |
| 6 | 3 | $1.99 \pm 0.02$ | $0.41 \pm 0.02$ | 0.9 |
| 6 | 4 | $1.97 \pm 0.01$ | $0.29 \pm 0.02$ | 0.9 |
| 7 | 1 | $3.41 \pm 0.09$ | $0.83 \pm 0.04$ | 1.1 |
| 7 | 2 | $2.36 \pm 0.03$ | $0.55 \pm 0.03$ | 0.9 |
| 7 | 3 | $2.04 \pm 0.02$ | $0.42 \pm 0.02$ | 1.8 |
| 7 | 4 | $2.12 \pm 0.02$ | $0.36 \pm 0.02$ | 0.9 |
| 8 | 1 | $3.07 \pm 0.09$ | $0.77 \pm 0.04$ | 1.0 |
| 8 | 2 | $2.00 \pm 0.05$ | $0.48 \pm 0.05$ | 1.3 |
| 8 | 3 | $1.93 \pm 0.03$ | $0.49 \pm 0.03$ | 1.4 |
| 8 | 4 | $1.88 \pm 0.02$ | $0.47 \pm 0.02$ | 1.8 |

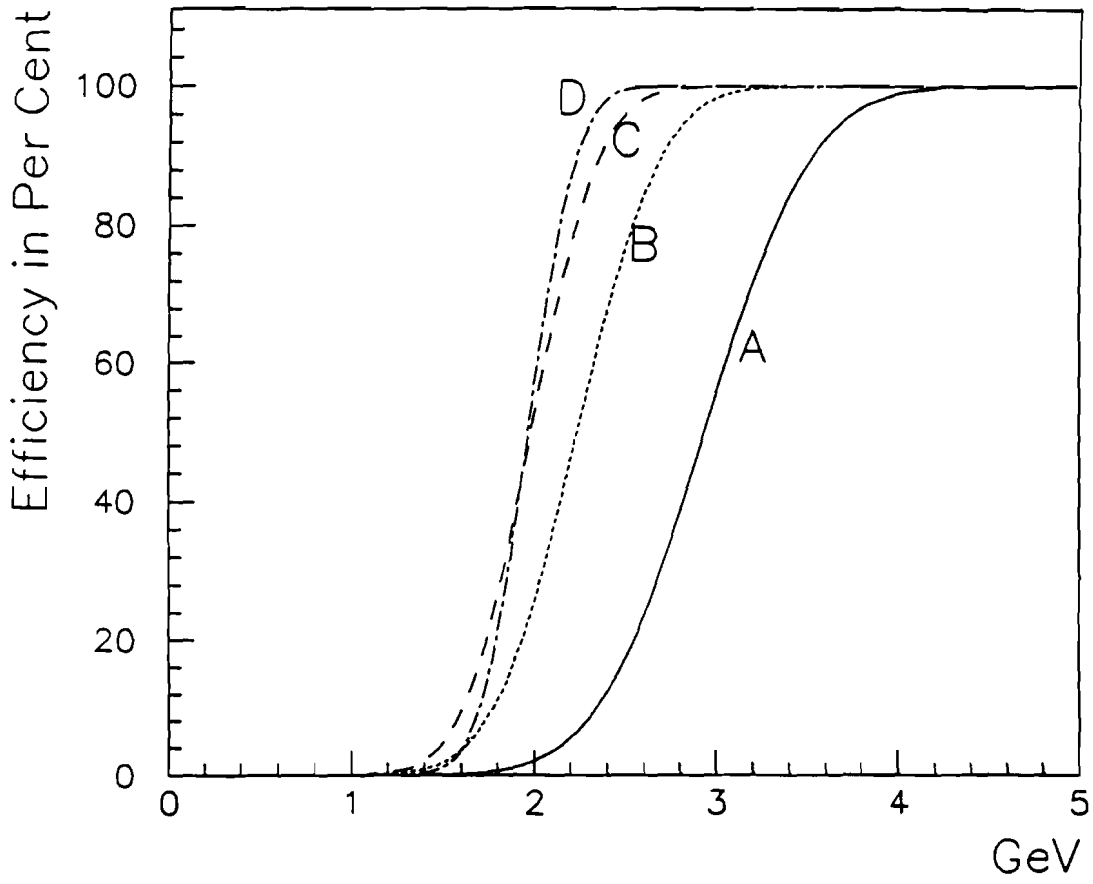


Figure 3.11: Example of Two-Gamma Efficiency Curves. For an arbitrarily chosen octant, the four different rapidity regions, A) region 1, B) region 2, region 3 and D) region 4, responded differently to the triggered particles.

octants) or, 2) the two octants *could* both be part of the same trigger. In the former situation, the trigger acceptance simply decreases by 1/2 and in the latter it decreases by 5/12, assuming that all three opposite octants have equal probability of triggering. If this assumption is true (which it isn't, but more on this momentarily), the corresponding corrections for these are 12/6 = 2 and 12/(12-5) = 12/7, respectively. There were occasional runs in which a single octant was not working very well (varying from 0–10% of neighboring octant activity). For these runs, no events from this particular octant were used and the 4/3 correction was applied.

As mentioned above, it is not true that a Two-Gamma trigger is equally probable to occur in the directly opposite octants (say, 4 and 8) as in the adjacent-opposite octants (4 and 1 or 4 and 7), see Figure 3.6 and Table 3.1. Suppose $\epsilon$ is the probability that a directly opposite pair triggers. Since for each such opposite octant-pair, there are two adjacent-opposite pairs, the occurrence probability for these is $(1-\epsilon)/2$. For the entire detector, there are four directly opposite pairs available, so the probability that any one of these four pairs is in the trigger is $\epsilon/4$ and the probability that any adjacent-opposite pair is in the trigger is $(1-\epsilon)/8$. For two octants out of order (i.e., not working), the acceptance decreases by $3\times(1-\epsilon)/8+2\times\epsilon/4 = (3-\epsilon)/8$ and the correction is $8/(5-\epsilon)$. This correction was applied to a set of runs in Set E during which time octants 5 and 8 were not operating properly. From fully reconstructed $\pi^0$ pairs in runs where all octants were working properly, $\epsilon$ was determined to be 0.61.

### 3.4.4 Selection of Single $\pi^0$s

Before we define a single $\pi^0$ we select events which have a reconstructed vertex in the target region. Then for each trigger octant, effective mass combinations are made for all pairs of fully reconstructed electromagnetic showers (hereafter referred to as *photons*) which satisfy the following cuts:

- No PWC track within 1.0 cm of a photon at $Z_{LAC}$
- $E_F/E_{TOT} > 0.2$
- $DR \leq 0.4$
- Pass EMLAC fiducial cuts

The quantity $DR$ is referred to as the *directionality* and is defined as

$$DR \equiv r_F - r_B \frac{Z_F}{Z_B} \tag{3.4}$$

where the subscripts F and B refer to the front and back sections of the EMLAC, respectively. Also, $r$ refers to the radial position measurement and $Z$ is the position along the z-axis.

The track cut is intended to remove electrons from the sample of showers. The $E_F/E_{TOT}$ cut eliminates hadronic-type showers while the directionality cut (DR) reduces the number of muons which survived the veto wall cut. The EMLAC fiducial cuts excluded showers which were near the quadrant and octant boundaries. These showers were considered less reliable since the detector is not fully sensitive in these regions.

Each pair of photons within a trigger octant must pass the following cuts:

- $p_T \geq 1.5$ GeV
- $Asymmetry \leq 0.75$

The effective mass of all two-photon combinations with $p_T \geq 2.0$ GeV is shown in Figure 3.12 both before (solid line) and after (dotted line) the asymmetry cut. In this figure, the $\pi^o$ mass range is defined by $A$ and the lower sideband region by $B$ and the higher sideband by $C$.

The angular distribution of photons from $\pi^o$ decay is isotropic in the $\pi^o$ rest frame ($\pi^o$s have zero spin). For relativistic $\pi^o$s (this is true for all of our reconstructed $\pi^o$s), this center of mass angular distribution is the same as the asymmetry distribution defined in the lab as:

$$A = \frac{\mid E_1 - E_2 \mid}{E_1 + E_2} \tag{3.5}$$

From this point of view, one may expect the asymmetry to be flat. It turns out that high values of asymmetry (near $A \sim 1$) correspond to $\pi^o$s which are very difficult to detect experimentally since one photon is typically of very low energy (and below our detector threshold) and the other has a high energy (since we triggered on it). The high energy photon is reconstructed and combined with low energy photons not associated with the initial $\pi^o$ decay. For experimentally observed $\pi^o$s, we expect a flat asymmetry distribution which dips at high values. Figure 3.13a is the background subtracted

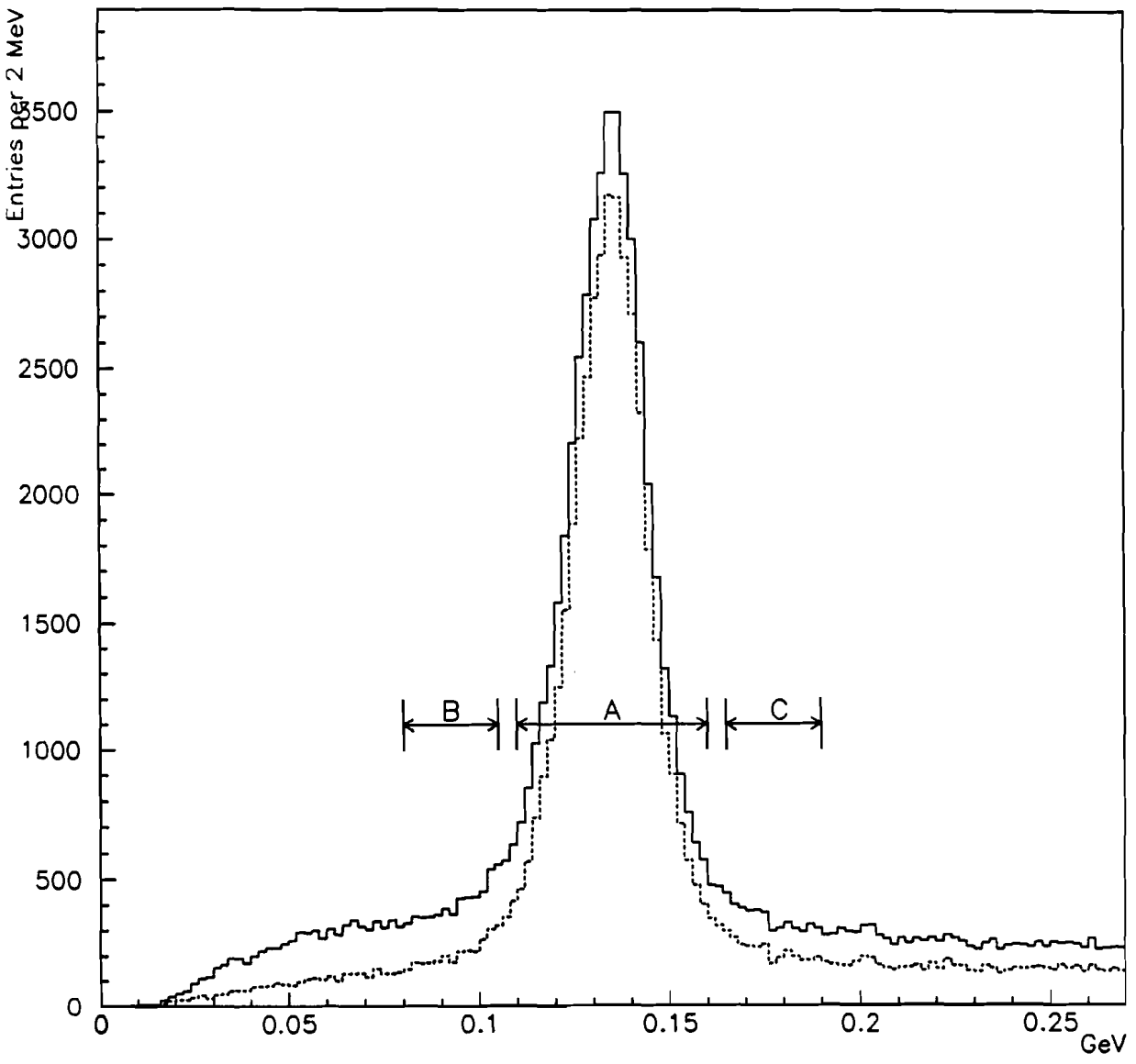


Figure 3.12: $\gamma\gamma$ Effective Mass. The dotted line shows the result of applying an asymmetry cut of 0.75. Region $A$ ($\pi^0$ mass region) extends from 110–160 MeV; Region $B$ (lower sideband) extends from 80–105 MeV; Region $C$ (upper sideband) extends from 165–190 MeV. The nominal $\pi^0$ mass is 135 MeV.

asymmetry distribution for reconstructed $\pi^0$s; the dotted line is an overlay of the same distribution from Monte Carlo generated $\pi^0$s. Figure 3.13b and c are the asymmetry for the two background regions on either side of the $\pi^0$ mass region, as defined in Figure 3.12.

With the EMLAC focussed on the target, the radial shower position in the front section should be very similar to that in the back section. The directionality cut removes showers originating in places other than the target.

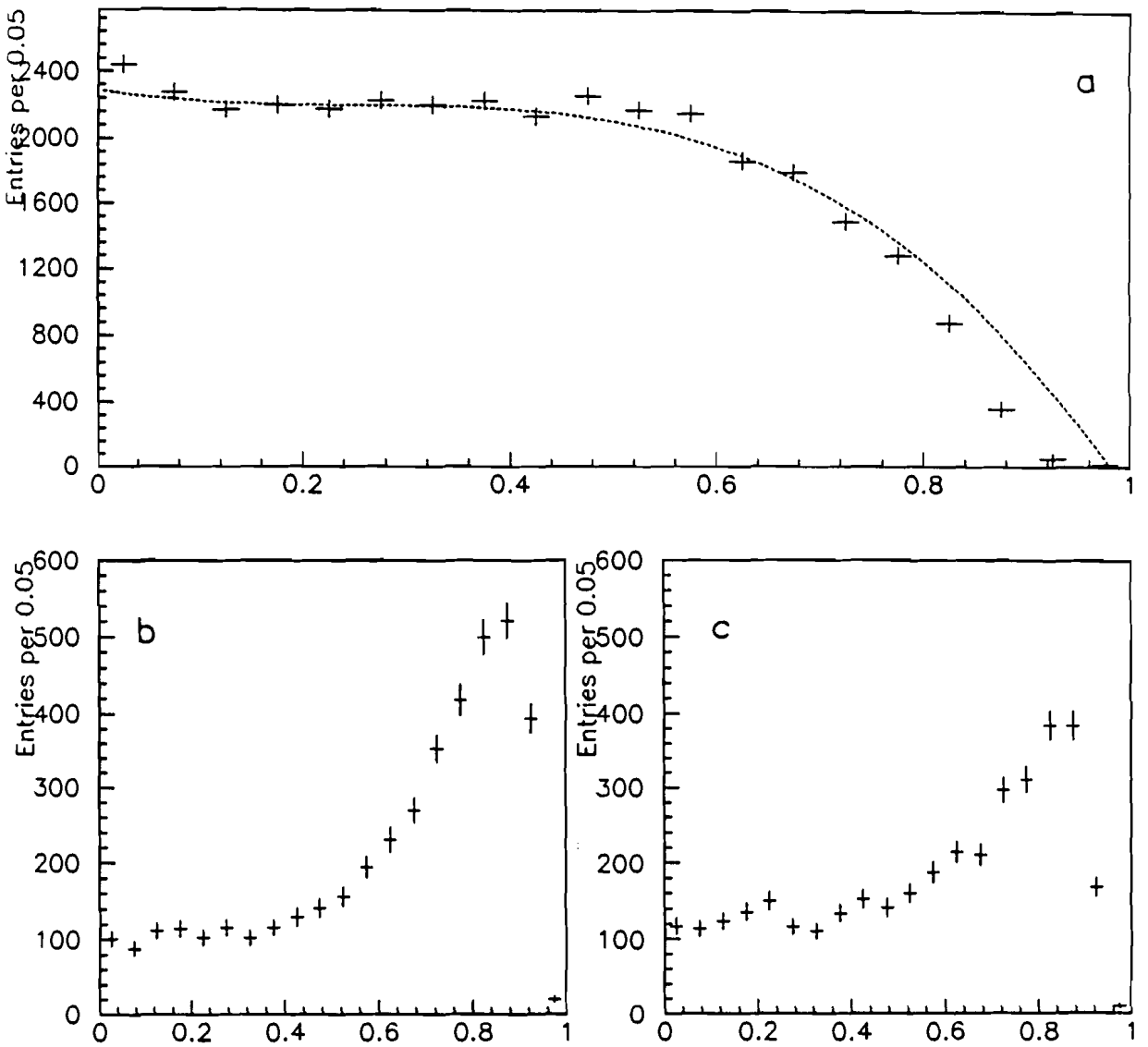


Figure 3.13: Two-Photon Asymmetry Distributions. (a) the $\pi^o$ mass region with the background subtracted: the dotted line is a Monte Carlo overlay; (b) lower sideband region; (c) upper sideband region. The regions are defined in Figure 3.12.

# Chapter 4

# Electrons

In this chapter we will present a brief discussion of the properties of electrons as observed simultaneously in both the tracking system and in the electromagnetic calorimeter. We will begin with a description of the source of the electrons used in this study and follow with a definition of the cuts used to select them. Having a rather clean sample of electrons, we will then compare results obtained from the two components of the spectrometer. All data presented here were obtained from analyzing the DST data described in Section 3.3.3.

## 4.1 Photon Conversions

In the course of traversing nuclear matter, photons with energy above the two-electron mass threshold may convert to an electron-positron pair. Above about 200 MeV [17, 37], the cross section for this process has nearly reached its asymptotic value and is inversely proportional to the radiation length of a given material. The radiation length is defined as that amount

of material required, on average, for an electron to degrade its energy by 1/e of its initial value. We will refer to these conversion electrons as ZMPs (zero mass pairs).

Since most of the photons generated and observed in E706 come from the decay of $\pi^o$s, this is the primary source of electrons. The ZMPs are then generated in the target (primarily) and enter the spectrometer as a pair of charged tracks along with the remainder of the event. The characteristic opening angle of a ZMP is $\sim m_e/E_\gamma \sim 0.1$ mr[1] for a 5 GeV photon; as such, we expect most ZMP electrons to be seen as a single track in the silicon strip detector system since the angular resolution here is at best $0.7 \times 10^{-1}$ mr. As the electron pair passes through the magnet, the individual tracks will split apart and become resolvable in the wire chamber system as two distinct tracks in three of the four views (X,U and V). In the Y-view, they will overlap since the upper limit of the angular resolution is about 0.4 mr. We will use these characteristics of the ZMP electrons for their selection.

## 4.2 Definition of a Zero Mass Pair

Basically, the scheme for selecting electrons is as follows: choose oppositely charged, PWC track pairs having the same slope in their Z-Y projection plane and which, in the Z-X projection plane, intersect at the center of the magnet. At this point one applies subsequent cuts to clean the sample. While these cuts will vary depending on the purpose of the study, we will

[1] We will use *mr* (milliradian) as a unit of angular measure where 1000 mr = 1 radian.

define them here and quantify them as we go along.

After selecting a pair of oppositely charged PWC tracks, we will apply the following cuts at various times throughout this chapter:

$\Delta S_Y$ : difference in y-slopes; tracks are selected with this less than $3.0 \times 10^{-3}$.

$ZXI$ : Z-X Intersection point; $189.3 \leq ZXI \leq 209.3$ cm.

$\Delta R^2$ : track-shower matching at $Z_{LAC}$; we define this as

$$\Delta R^2 = (X_T - X_S)^2 + (Y_T - Y_S)^2 \leq 1\ cm^2$$

where the T subscript corresponds to the projected track position at the EMLAC and the S subscript corresponds to the shower position. See Figure 4.1f.

$E_F/E$ : ratio of front EMLAC energy to total EMLAC energy for a shower; we typically make the selection that $E_F/E \geq 0.5$.

$E/P$ : ratio of EMLAC shower energy to tracking momentum; this is typically $0.7 \leq E/P \leq 1.3$ for an agreement of 30%.

We will frequently refer to the first two cuts together as the tracking ZMP cuts, $\Delta R^2$ as the matching cut and the the last two as the electromagnetic (EM) cuts.

We can see the ZMP signal in the distribution of Z-X intersections for all oppositely charged track pairs in Figure 4.2a. With the additional constraint

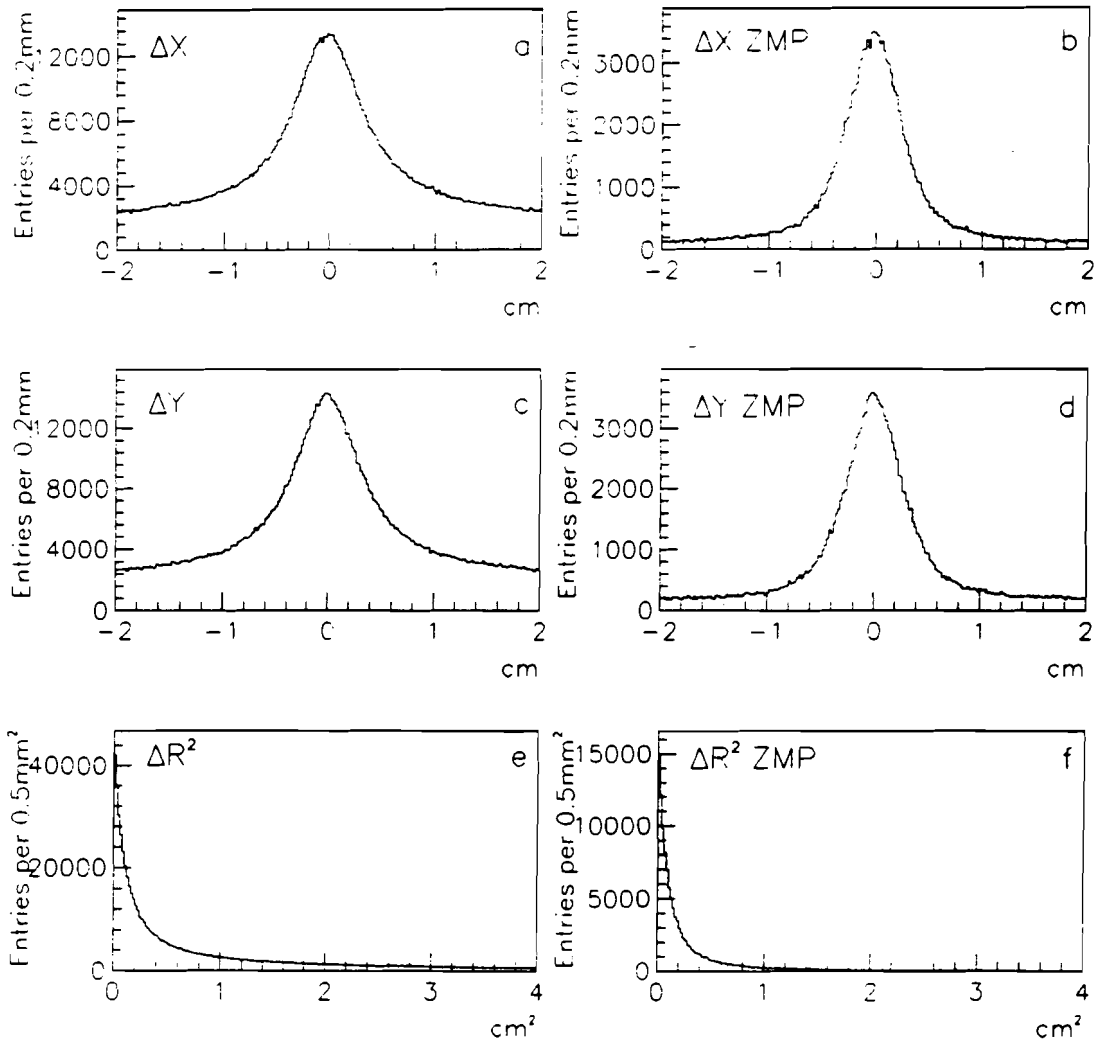


Figure 4.1: $\Delta X$, $\Delta Y$ and $\Delta R^2$ Distributions. (a) $\Delta X$, (b) $\Delta X$ (ZMP), (c) $\Delta Y$, (d) $\Delta Y$ (ZMP), (e) $\Delta R^2$ (f) $\Delta R^2$ (ZMP). ZMP indicates that the track was required to be a member of a zero mass pair.

that the two tracks satisfy the $\Delta S_Y$ constraint, the signal becomes much more prominent as shown in Figure 4.2b. Up to this point, the cuts have been limited to the tracking system; other tracking system cuts have only a marginal effect on the ZMP signal. In Figure 4.2c, we have required that both tracks match with showers in the EMLAC; this constraint has reduced the background substantially. A truly clean sample of electrons may now be selected by requiring that these matched showers satisfy electromagnetic cuts on EMLAC measurements. In Figure 4.2d, we have required that the both showers satisfy the two EM cuts.

In like manner, we may observe the effect of various cuts on the $\Delta S_Y$ distribution; see Figure 4.3. In this case, we show in Figure 4.3a, $\Delta S_Y$ for oppositely charged track pairs and in Figure 4.3b, we have selected those tracks satisfying the ZXI cut. For Figure 4.3c and 4.3d, we have applied the same cuts as in Figure 4.2c and 4.2d.

The means of the $ZXI$ and $\Delta S_Y$ distributions are not measurably dependent upon the momentum[2]. If we select all ZX intersections within the range 190 cm to 210 cm and plot the mean as a function of momentum (applying the $\Delta S_Y$ cut on single matched ZMPs) we have the flat distribution shown in Figure 4.4a. Likewise in Figure 4.4b, we see that the momentum

[2]We will make the following distinction between the electron energy and momentum: energy is measured in the electromagnetic calorimeter and momentum is measured in the tracking system. As a result, there is more content to an E/P plot than the simple kinematical relationship; it will reveal various features of our energy and momentum measurements.

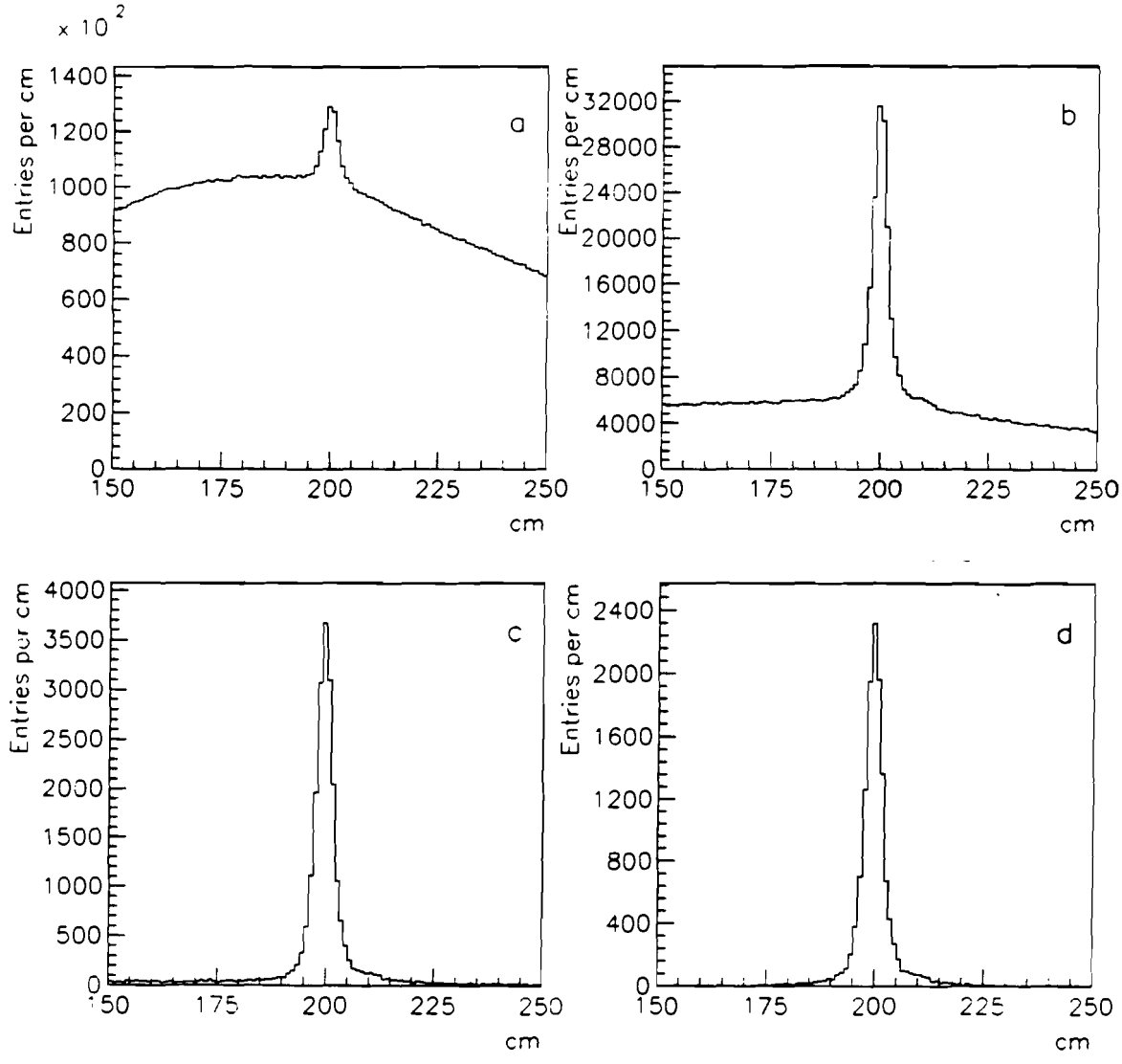


Figure 4.2: Z–X Intersection. The effect of various cuts on the distribution of Z–X intersection is shown in this series of plots: (a) all oppositely charged track pairs; (b) $\Delta S_Y \leq 3$ mr; (c) both tracks match with showers; (d) $E_F/E \geq 0.5$ and $0.7 \leq E/P \leq 1.3$. Each plot has the cuts of the previous plots; i.e., b) also has the same cuts as a), etc.

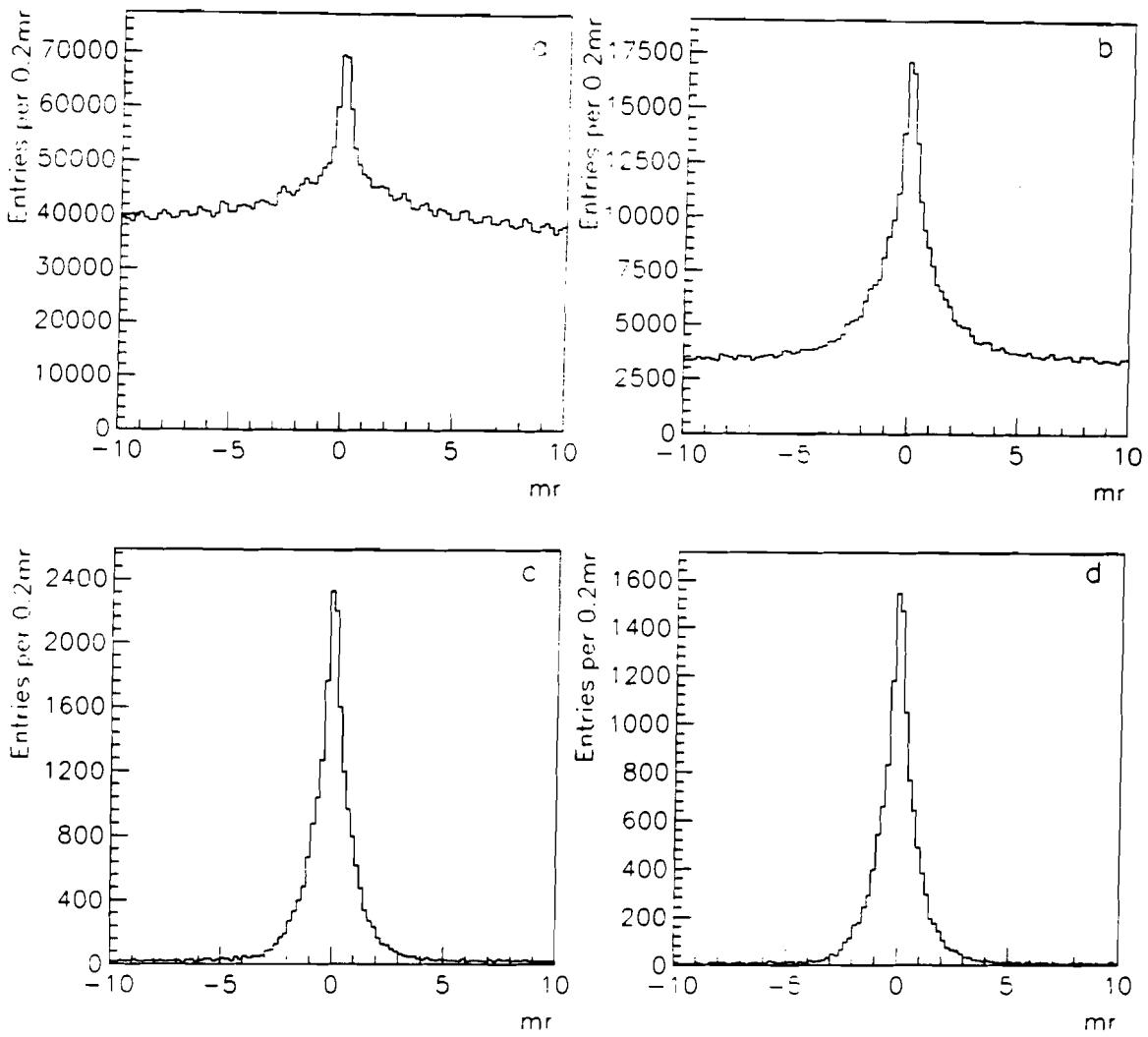


Figure 4.3: $\Delta S_Y$ Distributions. The effect of various cuts on the distribution of $\Delta S_Y$ is shown in this series of plots: (a) all oppositely charged track pairs; (b) ZXI = 199.3 $\pm$ 10 cm; (c) both tracks match with showers; (d) $E_F/E \geq 0.5$ and $0.7 \leq E/P \leq 1.3$. Each plot has the cuts of the previous plots; i.e., b) also has the same cuts as a), etc.

dependence of the $\Delta S_Y$ (applying the $ZXI$ cut on single matched ZMPs) is flat out to around 125 GeV. This distribution was limited to the range $\pm 3$ mr. In both figures, the vertical error bars represent the error on the mean in the given bin.

The track-shower matching cut is motivated by the plots in Figure 4.1 where we show the $\Delta X$, $\Delta Y$ and $\Delta R^2$ histograms. The $\Delta X$ and $\Delta Y$ distributions correspond to those showers nearest a given track in the event. The plots on the left (Figure 4.1a,c,e) are for all such track-shower combinations. Those on the right (Figure 4.1b,d,f) show the same quantity with the additional requirement that the tracks be part of a ZMP pair as defined by the two tracking ZMP cuts.

Since the EMLAC was designed and constructed to be focussed on the particles following a straight-line trajectory from the target (i.e. photons), it is reasonable to assume that some differences should be observed for unfocussed tracks. Low momentum electrons, being bent in the magnet, generate the largest deviation from a focussed trajectory. For example, suppose a 4.5 GeV electron is produced with zero $p_T$; it is bent 100 mr hitting the EMLAC at X = 70 cm. A photon generated in the target and striking the LAC at 70 cm makes an angle of 78 mr. The difference in these angles is a measure of the unfocussed character of the electron; in this case, 22 mr. If the centroid of the shower penetrates to 5 cm (this is typical for a shower of this energy [26]), this will correspond to a maximum position measurement error of about 1 mm. Since the track projection error at the

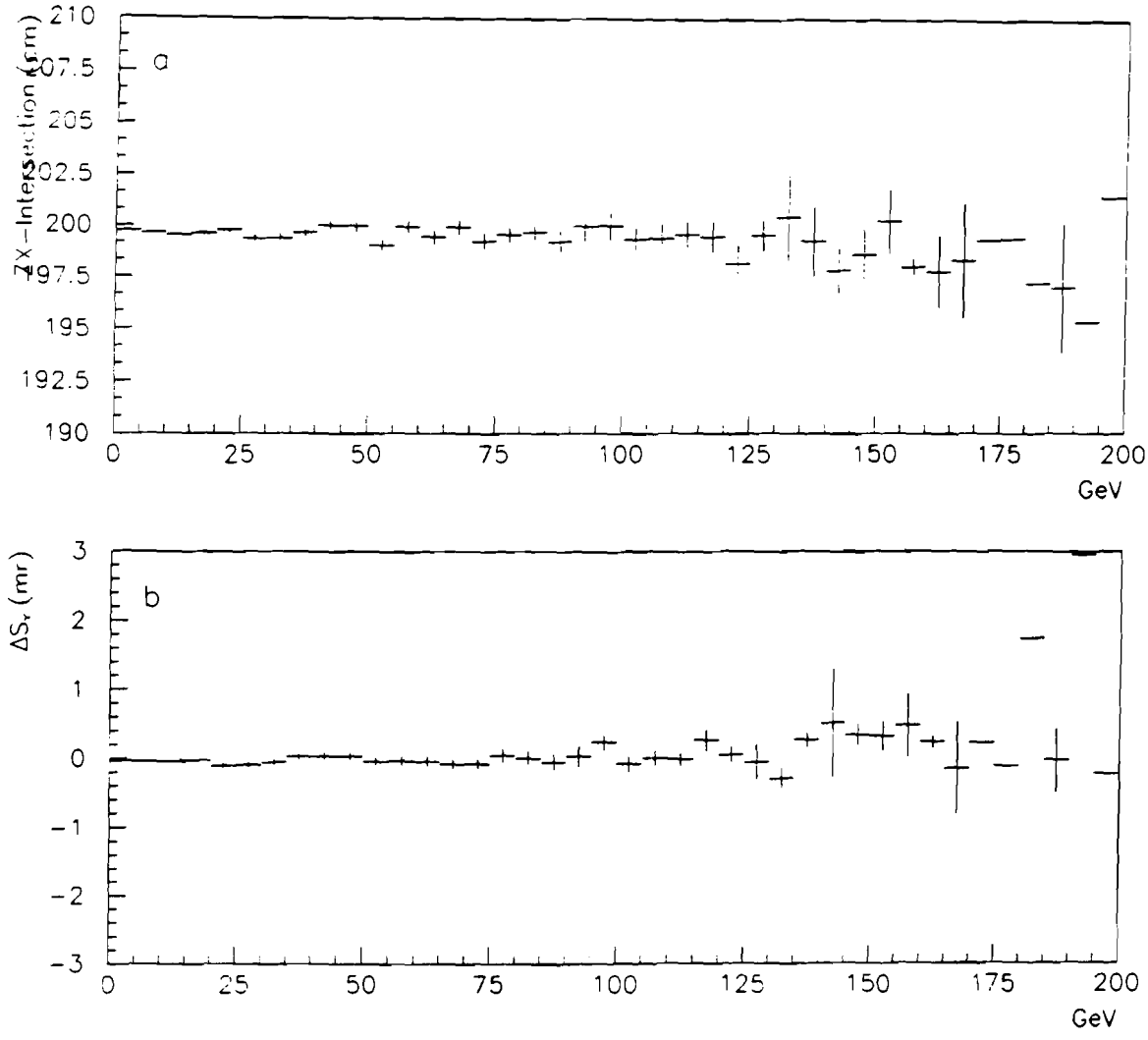


Figure 4.4: $ZXI$ and $\Delta S_Y$ vs Momentum. (a) Z-X Intersection vs Momentum ($\Delta S_Y \leq 0.3\ mr$) and, (b) $\Delta S_Y$ vs Momentum ($ZXI = 199.3 \pm 10\ cm$). These data are from the ZMP electron sample in which one or more of the electrons matches with a shower.

EMLAC is about 2 mm (for an angular resolution of 0.4 mr), it is very unlikely that both the track and shower positions will fluctuate in the same direction to fall outside the matching cut of 1 $cm^2$ (see Figure 4.1f).

Although the numbers in this example represent the worst case for an electron of this momentum, they give an indication of the level of the problem. From the data we show in Figure 4.5a the dependence of $\Delta R^2$ on the momentum of ZMP electrons. The mean of $\Delta R^2$ increases with decreasing momentum as we expect. Also shown, in Figure 4.5b, is $\Delta R^2$ vs radial position in the EMLAC. Similarly, since electrons with lower momenta tend to populate the outer regions of the detector, we see $\Delta R^2$ increase with radial position.

## 4.3 Properties of the ZMP Electrons

Having defined the cuts used to select electrons, we will now look at various distributions describing their characteristics.

With $\pi^o$ photons as the primary source of ZMP electrons, we expect the energy distribution to be heavily weighted towards the low energy region, when compared to the $\pi^o$ energy spectrum. In the energy spectrum of Figure 4.6b, we see that while the energies are typically less than 20 GeV (the mean is 17 GeV), electrons are observed out to energies around 150 GeV. There are a few differences between the energy and momentum spectra which we will point out here and discuss more fully in Section 4.4.2.

At the low end of both the energy and momentum spectra, the distribu-

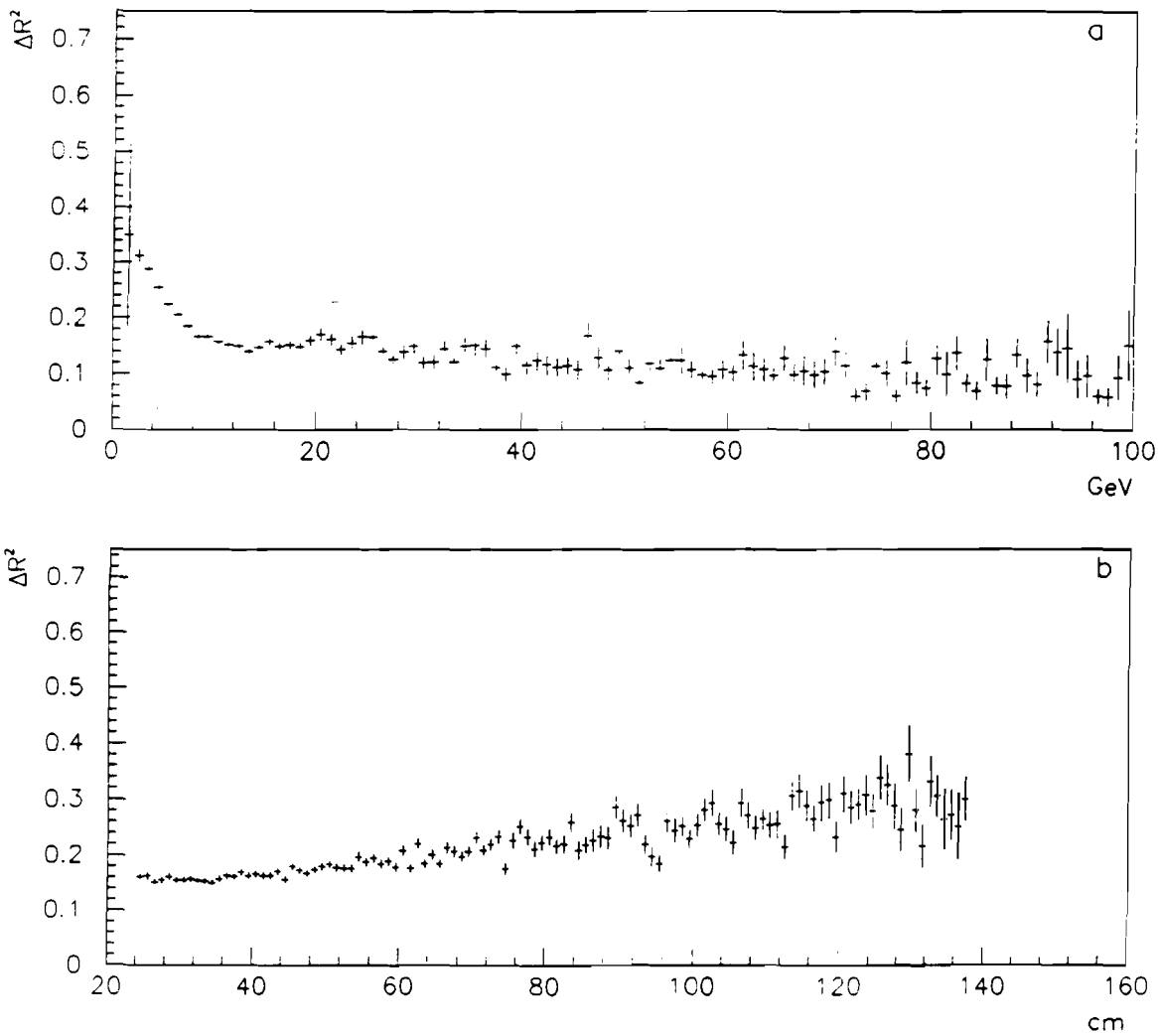


Figure 4.5: Momentum and Position Dependence of Track–Shower Matching. (a) $\Delta R^2$ vs Momentum, (b) $\Delta R^2$ vs Radial Position at EMLAC.

tions fall off since the acceptance for both devices is constrained here. The high end of the distributions indicate that we have more electron tracks in this region than we have showers. This is purely an artifact of the tracking resolution. We will discuss this situation more fully in Section 4.4.2.

Since ZMP electrons tend to have low momentum, we expect them to be distributed horizontally across the face of the EMLAC. The distribution of electron positions is shown in Figure 4.7. The sample of ZMPs which went into this plot was required to fall within the sensitive regions of the calorimeter. In this plot, the EMLAC hole, the octant and quadrant boundary fiducial cuts are clearly visible.

With the EMLAC sectioned longitudinally (see Section 2.4.1), we may apply a cut on the ratio of front energy to total energy ($E_F/E$) for each shower. The distribution of this ratio, for all showers which match with tracks, is shown in Figure 4.8a. The peak at low values of $E_F/E$ signifies tracks of a hadronic nature, while that at the higher end corresponds to electromagnetic-type showers. In Figure 4.8b we plot $E_F/E$ for ZMP tracks which match with showers. No other electromagnetic-type cuts were applied to the data of this plot. We can still see a small hadronic bump in the region $E_F/E \leq 0.2$ along with a spike in the first bin which indicates zero energy in the front. The two lower plots, Figure 4.8c and 4.8d, demonstrate the energy dependence of this distribution. Figure 4.8c shows the distribution for energies less than 10 GeV while Figure 4.8d shows that for energies greater than 50 GeV. It is clear that low energy electron showers tend to deposit a larger fraction of their total energy in the front of the detector

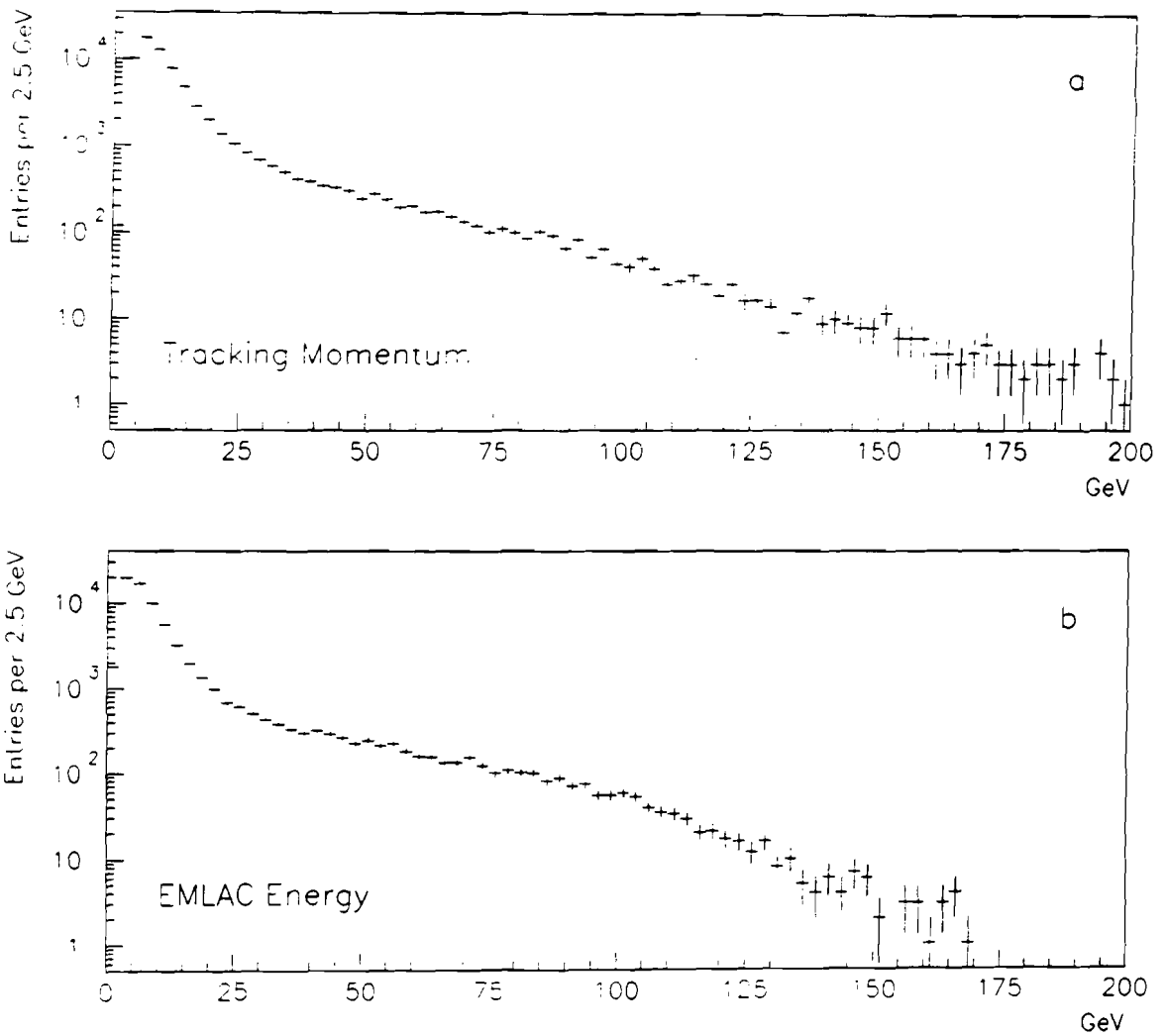


Figure 4.6: Momentum and Energy Spectra of Electrons. (a) Momentum as measured in the tracking system, and (b) energy as measured in the EMLAC.

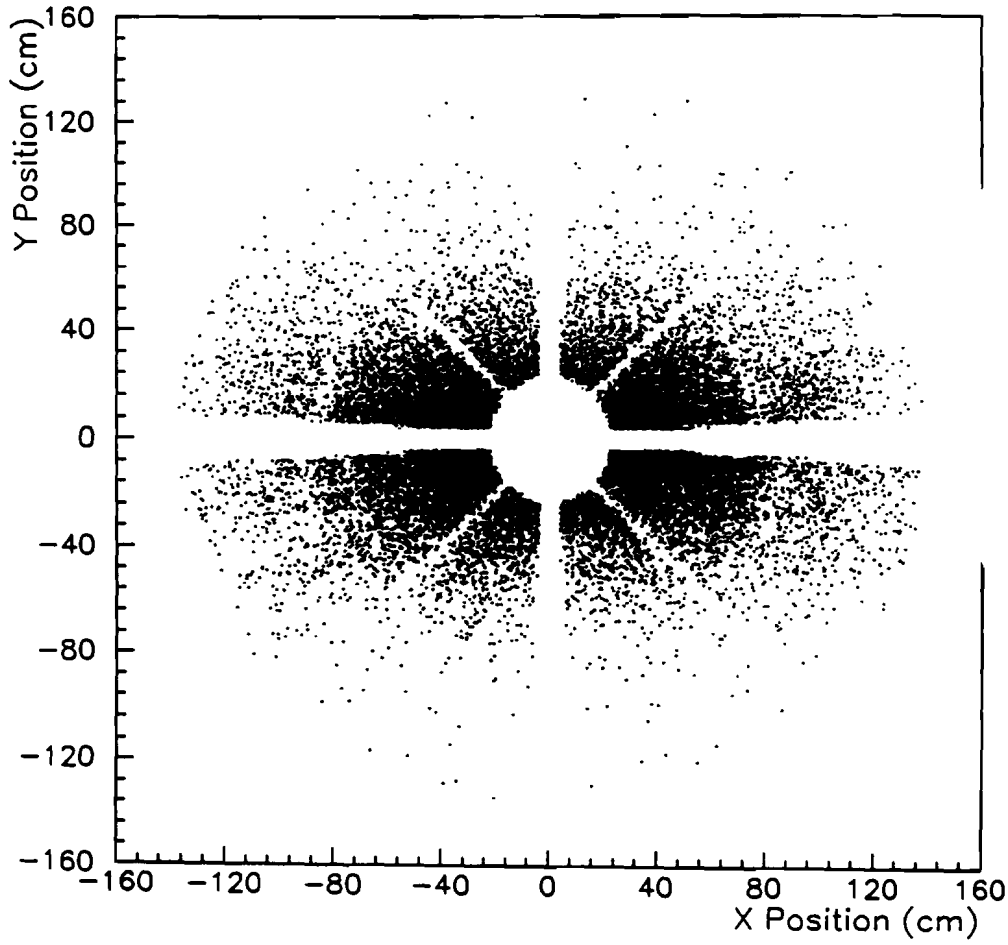


Figure 4.7: Position of ZMP Electrons at EMLAC

than their higher energy counterparts.

All of the plots in Figure 4.8 have been made for the range 0.0 – 0.99 in the ratio of $E_F/E$, since about 20% of the entries of the histogram are in the 0.99 – 1.00 bin. The electrons which fall in this particular bin have no detected energy in the back. This effect has been completely reproduced with a Monte Carlo signal generated from ZMP electrons found in a simulation of full hadronic events using the PYTHIA[35] event generator and the GEANT3[13] detector simulator[26] by applying a minimum energy requirement on each strip of 250 MeV. This type of threshold was applied to the read-out hardware for most of the data (see [40]) to speed up the process of data acquisition.

An additional source of this effect is that of pre-LAC showering. There are about three radiation lengths of material before the first sensitive layer of the EMLAC, making it rather likely that some energy will be lost before we see it. As a result, low energy electromagnetic showers are likely to leave very little energy in the back of the detector and when it is then divided between strips in each of two views, none is detected. Now if each strip has to exceed some threshold value, the two effects conspire to make the situation more challenging. The behavior of low energy showers is still being actively studied with these electrons and the GEANT version of the experiment.

Although we will not apply cuts to the photon asymmetry distribution, we include it here for completeness. We define the photon asymmetry in a

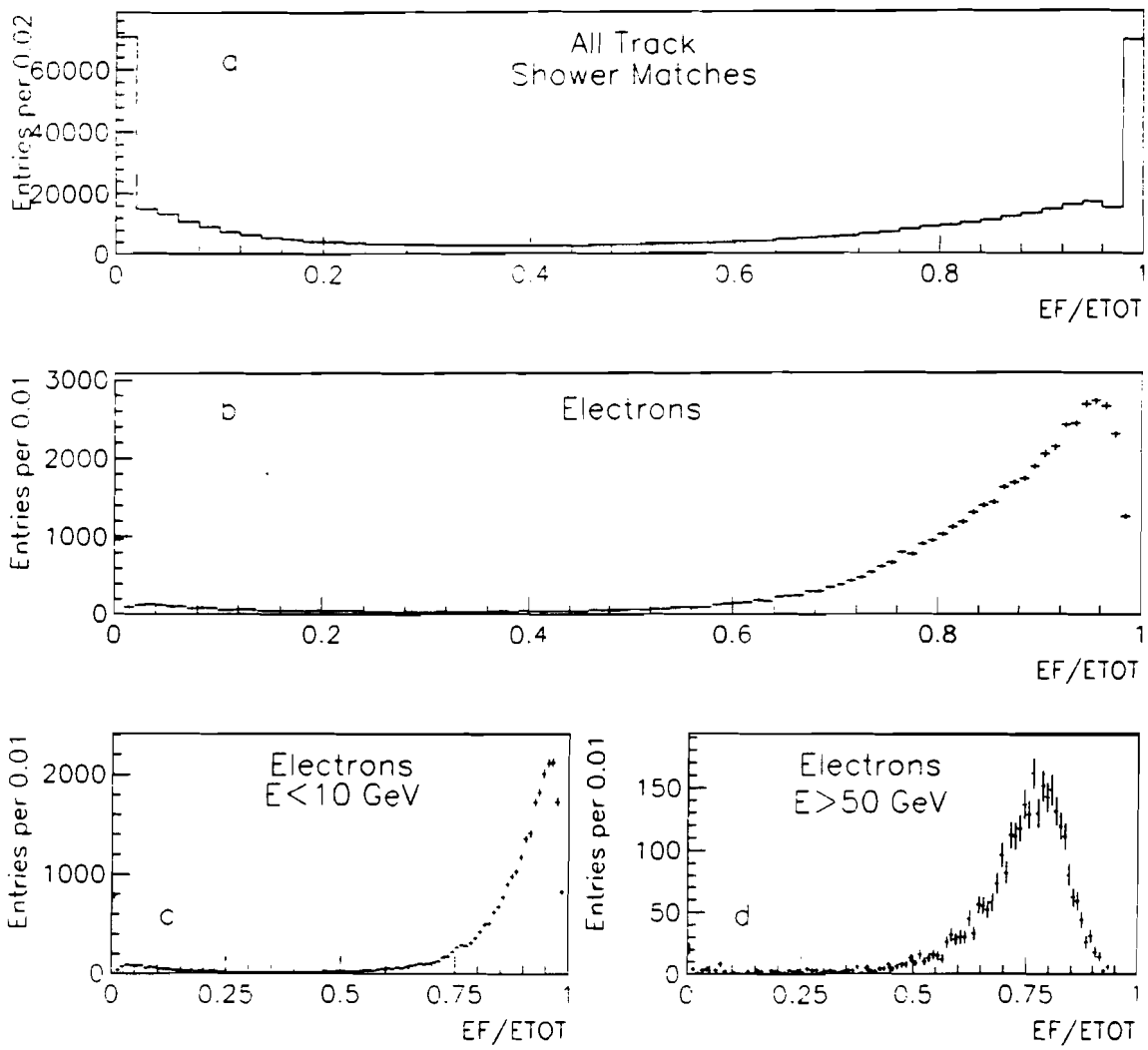


Figure 4.8: $E_F/E$ Distributions. (a) all showers which match with tracks at the EMLAC, (b) ZMP electrons, (c) ZMP electrons for $E \leq 10$ GeV, (d) ZMP electrons for $E \geq 50$ GeV.

manner similar to the $\pi^0$ asymmetry:

$$A = \frac{E_+ - E_-}{E_+ + E_-} \tag{4.1}$$

where the energies are those of the electrons. The asymmetry distributions are quite different depending on whether one calculates it using the momentum or energy. These distributions are shown in Figure 4.9 where on the left (Figure 4.9a,c,e) the asymmetry was calculated using the energies and on the right (Figure 4.9b,d,f) the calculation was made with the momenta. The difference in the distributions primarily reflects the difference in the acceptance of the two systems since for the momentum asymmetry plots, it was not required that both tracks match with showers.

## 4.4 E/P Studies

In this section we directly investigate the level of agreement between the electron energy as measured in the EMLAC and its momentum as measured in the tracking system. We will present these results in terms of Gaussian fits to the E/P distributions for both Monte Carlo and data. We will also test the dependence of the mean of E/P on momentum and energy.

### 4.4.1 E/P Distributions

The distribution in E/P is quite useful for pointing out various features of the data. We will begin the discussion by looking at the plots in Figure 4.10, which are for electrons with energies in the range 18±1 GeV. In Figure 4.10a,

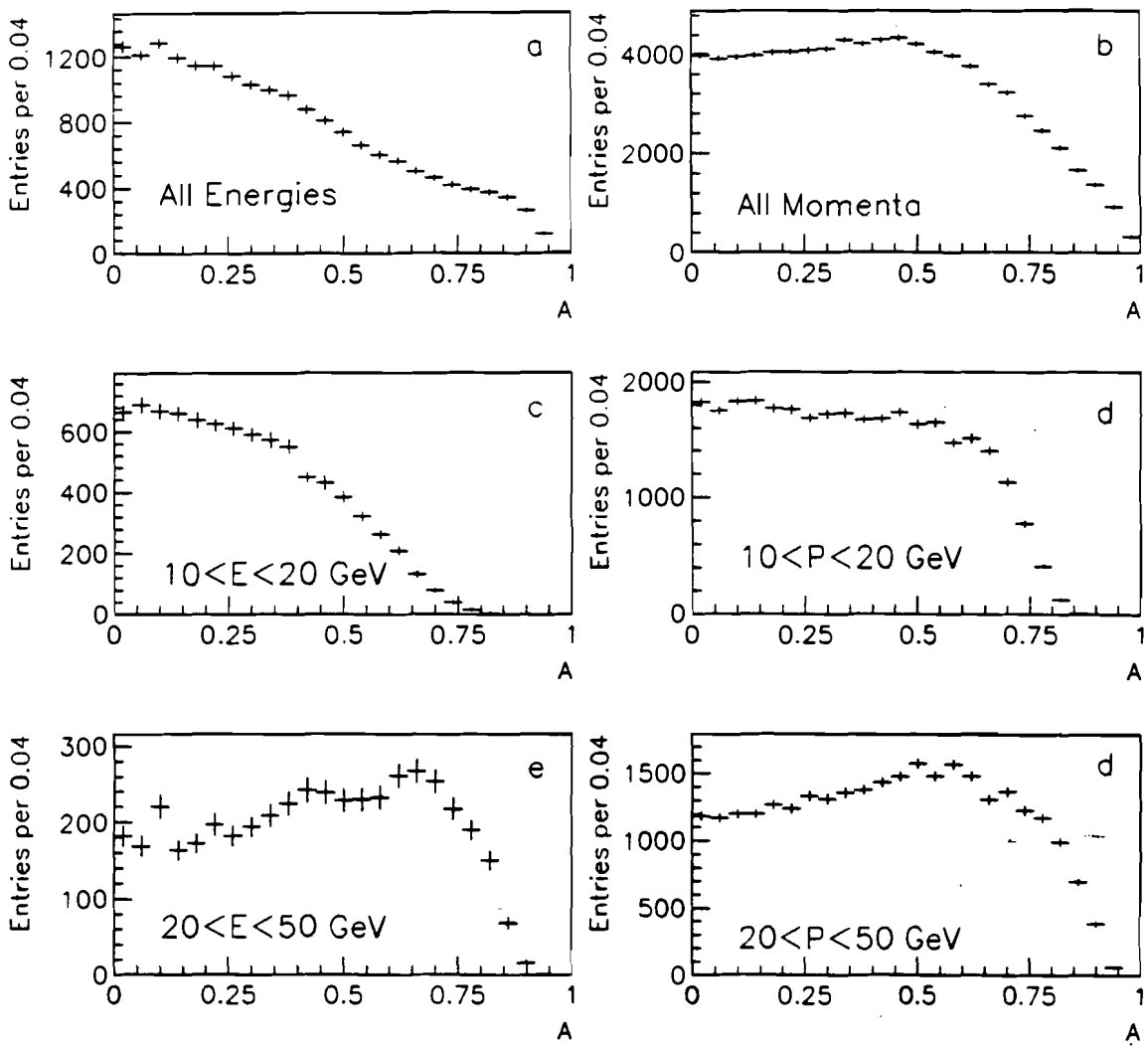


Figure 4.9: Photon Asymmetry Distributions. (a,c and e) using EMLAC energies, (b,d and f) using tracking momenta. (a and b) no cuts; the rest of the plots show the effect of taking slices in either energy or momentum.

Table 4.1: Number of ZMPs. These numbers are not corrected for any detector inefficiencies or trigger threshold changes. Set A had a trigger threshold substantially lower that the other sets and Set B tracks were reconstructed without PWC module 3.

| Set | A | B | C | D | E |
|---|---|---|---|---|---|
| Events ($\times 10^5$) | 3.37 | 0.95 | 1.29 | 1.64 | 1.74 |
| Single Match (%) | 9.1 | 4.2 | 6.2 | 6.8 | 6.4 |
| Double Match (%) | 2.6 | 1.2 | 1.7 | 2.0 | 1.8 |

we have required that at least one of the ZMP tracks matches with an EMLAC shower while in Figure 4.10b we have requested that both tracks match. All showers in both plots have been subject to the $E_F/E$ cut. It is not clear what type of tracks generate the small bump in the region $E_F/E \leq 0.5$, but they disappear when it is required that both tracks match with EM-type showers. While this is consistent with a hadronic background, they are still very interesting. What type of hadrons pass all of the ZMP cuts to this point? Are they actually charged kaons from $\phi$ decay?

Some of this low side tail may be described by energy loss in the EMLAC. This cannot be the entire explanation since these entries completely disappear when applying tighter electromagnetic cuts. The point here is simply that we will select only events in which both tracks match with showers for the following analysis. Based on Figures 4.10 and Figure 4.2, we conclude that the hadronic background leaking into the electron signal is negligible.

Although the angular resolution of the tracking system is independent of the momentum of the track, the momentum resolution is not: it decreases with increasing momentum. On the other hand, since the measurement of energy in a calorimeter is a statistical process, the fractional error in the measurement decreases with energy. As a result, at low momenta, the tracking momentum resolution is negligible compared to the energy resolution and at high momenta the situation is reversed. We will exploit this situation by looking at E/P distributions in the following three intervals:

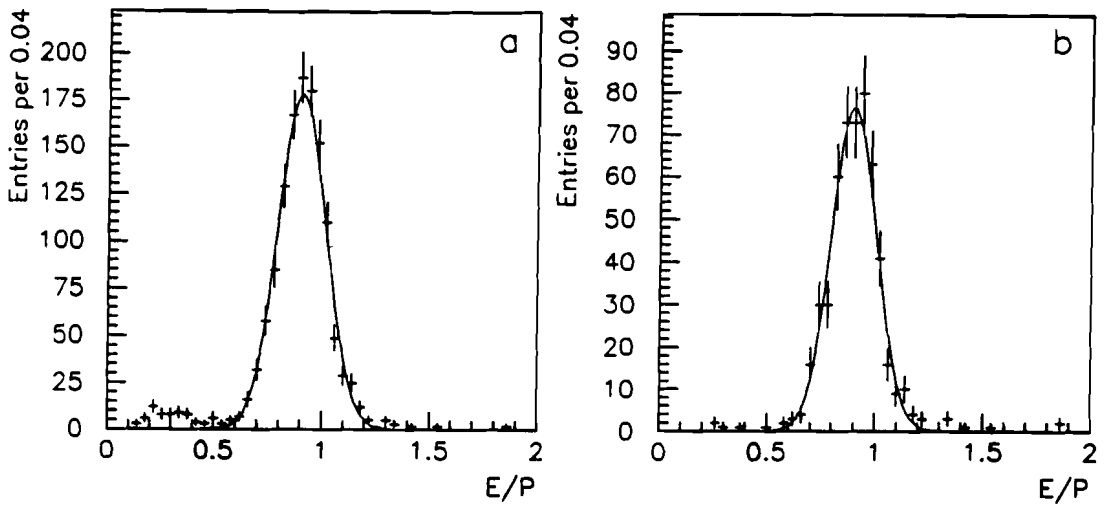


Figure 4.10: E/P for ZMP Electrons in the range: $P = 18 \pm 1 GeV$. The E/P distribution changes when the electrons are subjected to the following cuts: (a) at least one track matches with a shower; (b) both tracks match with showers. Both plots have the shower requirement $E_F/E \geq 0.5$ in addition to the tracking ZMP cuts described in the text.

- Region 1: $9 \leq P \leq 11$ GeV ($\langle P \rangle = 9.95$ GeV)
- Region 2: $22.5 \leq P \leq 27.5$ GeV ($\langle P \rangle = 24.5$ GeV)
- Region 3: $60 \leq E \leq 70$ GeV ($\langle E \rangle = 64.7$ GeV)

For each region we will generate E/P plots employing a simple Monte Carlo which will be described here.[3] Take a sample of electron energies, $E_{GEN}$, randomized according to the electron energy in Figure 4.6 and apply to it a Gaussian smearing which will approximate the EMLAC energy resolution with which a new energy is generated, $E_1$. From $E_{GEN}$, the bend angle of the track may also be calculated. Similarly, a Gaussian resolution is applied to this bend angle and a new momentum, $P_1$, is calculated. We may now produce distributions in $E_1/P_1$ and compare with the data. Since this is a rather simple Monte Carlo, we cannot ask it to reproduce the subtle effects of the data. At best, we hope to show trends which simulate the shape of the data at high momentum.

With this Monte Carlo, we will show the expected contribution to the E/P plots from each detector system: EMLAC and tracking. Also, we will be able to directly compare the Monte Carlo $E_1/P_1$ with E/P from the data.

In Figure 4.11 we show the histograms of E/P for Region 1. The curves are Gaussian fits over the entire range of each histogram. Figure 4.11a we

[3] We use a *simple* Monte Carlo because the basic resolution effects are independent of the details of the detector and as a result, it is very fast.

plot $E_1/E_{GEN}$ as the expected contribution of the EMLAC energy resolution to the $E_1/P_1$ plot at this energy. The sigma on this fit is 12.8%. Similarly, in Figure 4.11b, we see that the contribution of 0.8 mr angular resolution for the tracking system is negligible ($\sigma$=1.9%) compared to the EMLAC resolution. In Figure 4.11c we combine the two generated quantities for the distribution of $E_1/P_1$ ($\sigma$=12.8%) while Figure 4.11d shows the result from the data ($\sigma = 12.7 \pm 0.3\%$). The EMLAC resolution used in the Monte Carlo is $\sigma_E/E = 0.4\sqrt{E}$; it was chosen to fit these data.

Similarly, in Figure 4.12 we show the histograms of E/P for Region 2. Again, the curves are Gaussian fits over the entire range of each histogram. Figure 4.12a is the expected contribution of the EMLAC energy resolution to the E/P plot at this energy ($\sigma$ =8.0%). In Figure 4.12b, we see that the tracking contribution is no longer negligible ($\sigma$=4.5%). Figure 4.12c shows the combined ($\sigma$=9.2%) E/P for the Monte Carlo while Figure 4.12d shows the data ($\sigma = 10.5 \pm 0.5\%$).

In like fashion, Figure 4.13 shows the histograms of E/P for Region 3. The curves are Gaussian fits over the entire range of each histogram. Figure 4.13a is the expected contribution of the EMLAC energy resolution to the E/P plot at this energy ($\sigma$ =5.0%). In Figure 4.13b, we see that the tracking contribution dominates ($\sigma$=11.6%). Figure 4.13c shows the combined ($\sigma$=12.6%) E/P for the Monte Carlo while Figure 4.13d shows the data ($\sigma = 12.1 \pm 1.2\%$).

From these distributions, it is clear that the data are consistent with

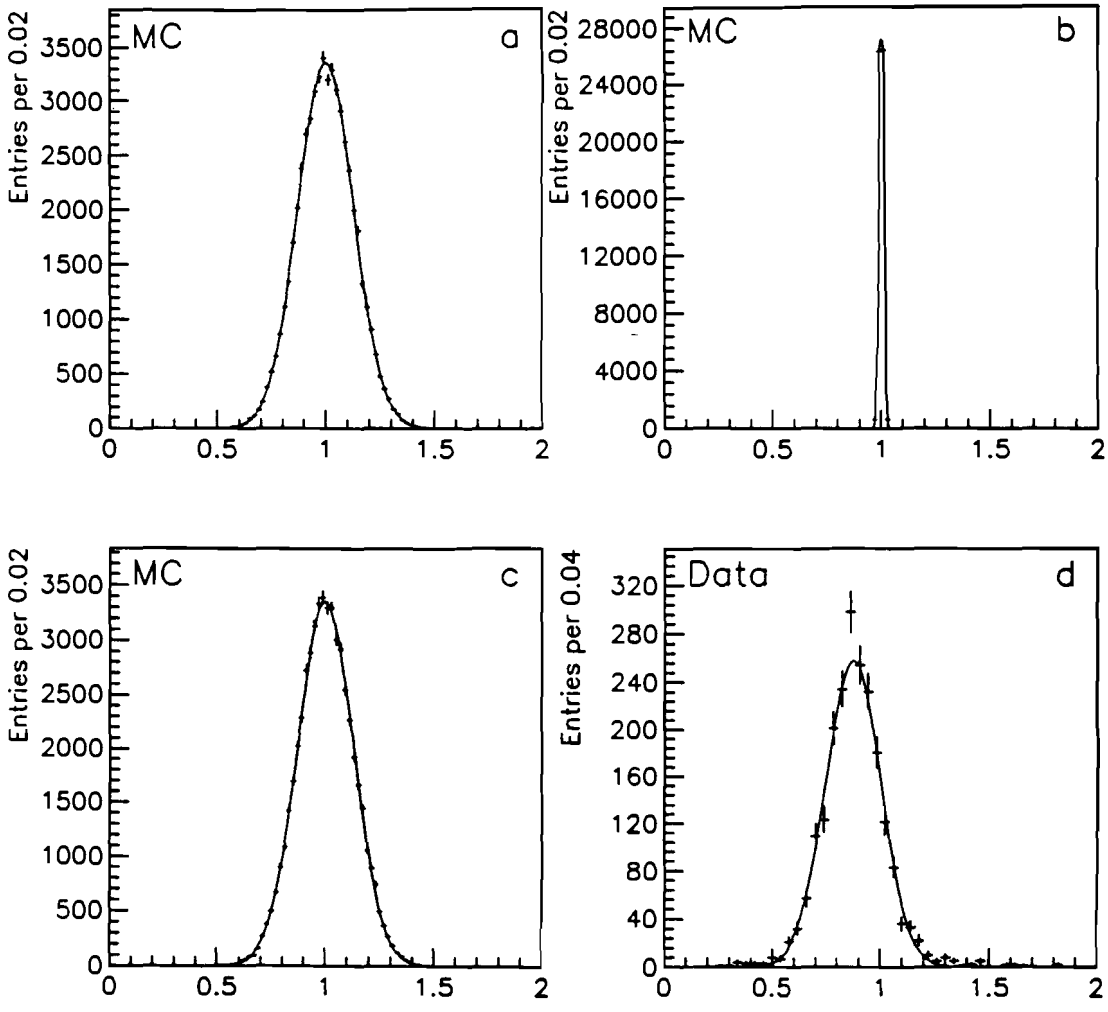


Figure 4.11: E/P for $9 \leq P \leq 11$ GeV. $\langle P \rangle$=9.95 GeV. (a) $E_1/E_{GEN}$ (Monte Carlo), (b) $E_{GEN}/P_1$ (Monte Carlo), (c) $E_1/P_1$ (Monte Carlo), (d) $E/P$ (Data).

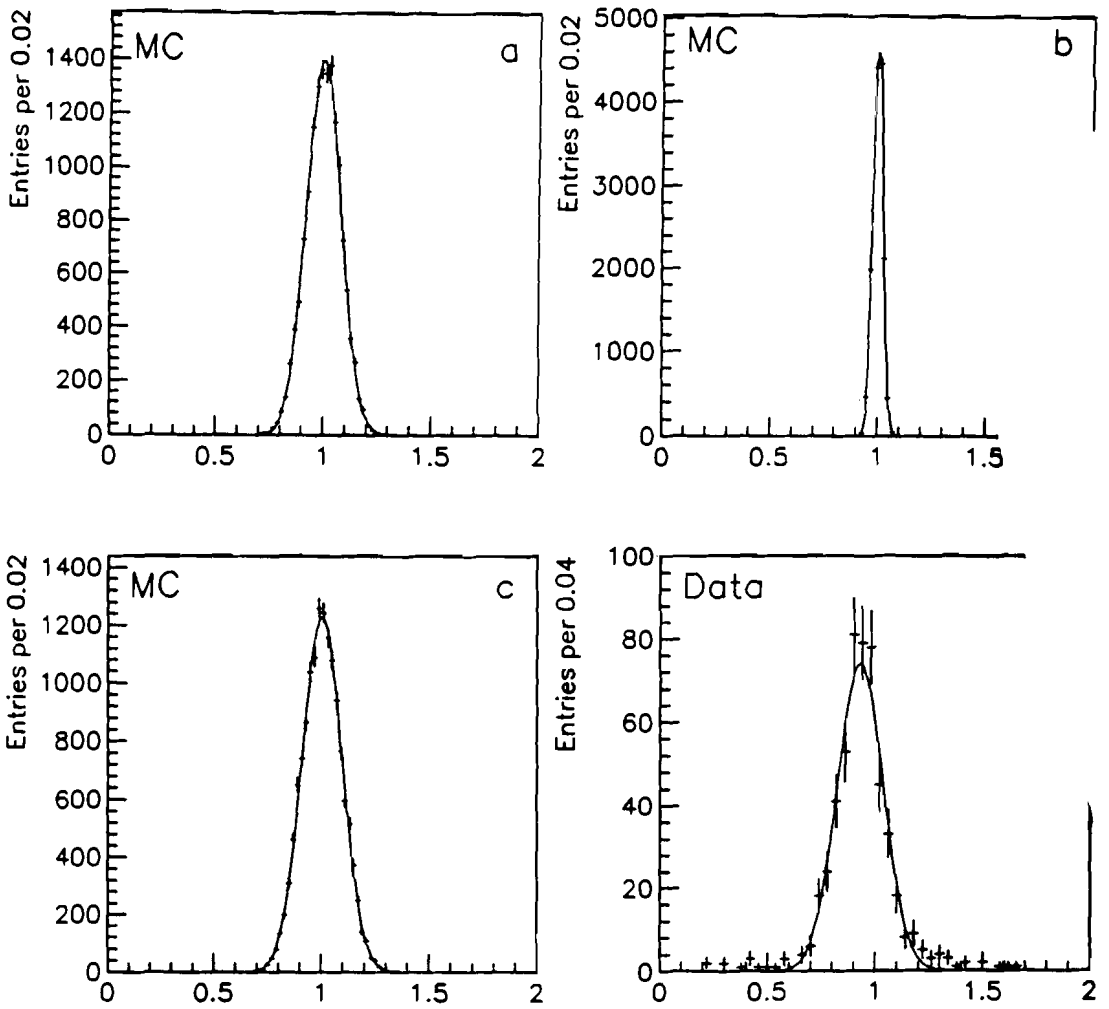


Figure 4.12: E/P for $22.5 \leq P \leq 27.5$ GeV. $\langle P \rangle$=24.5 GeV. (a) $E_1/E_{GEN}$ (Monte Carlo), (b) $E_{GEN}/P_1$ (Monte Carlo), (c) $E_1/P_1$ (Monte Carlo), (d) $E/P$ (Data).

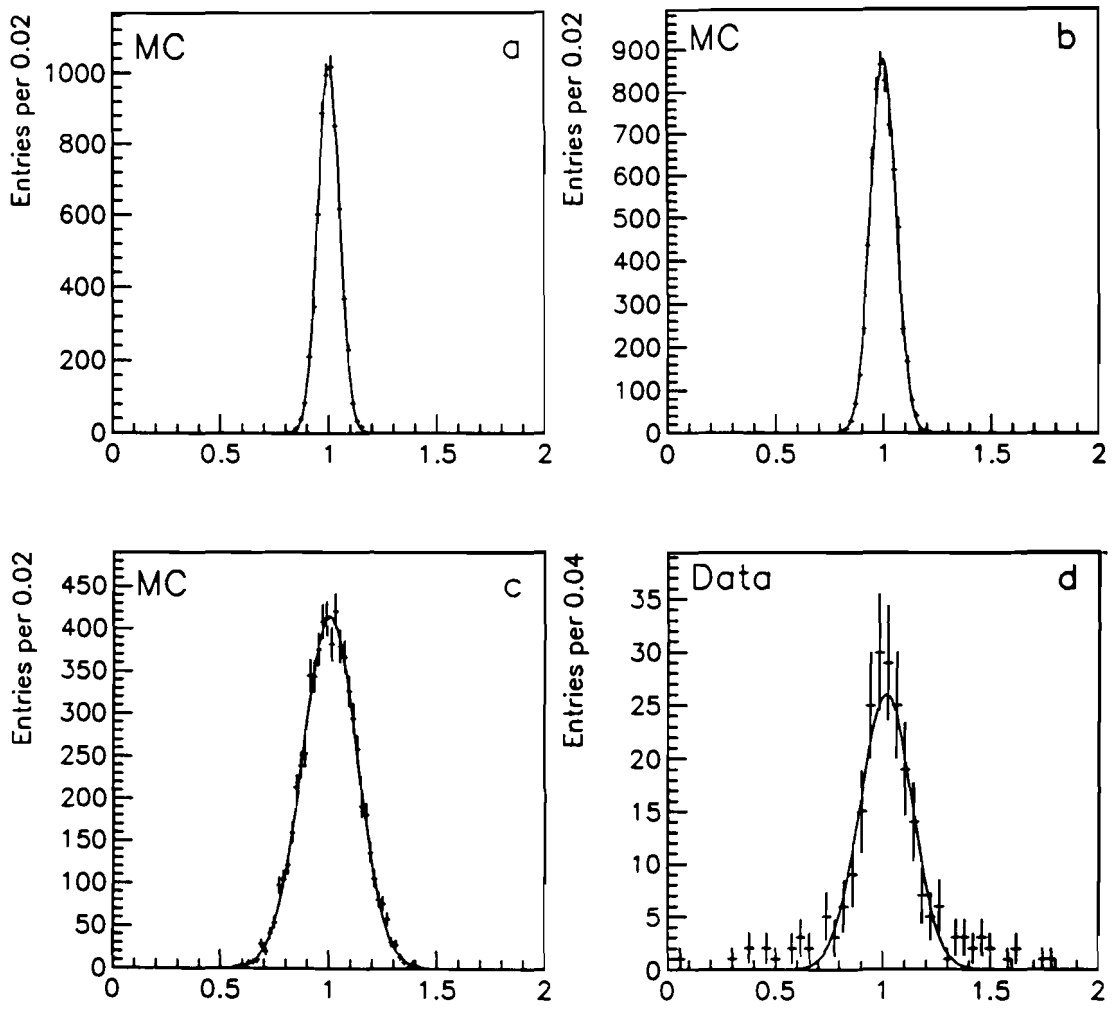


Figure 4.13: E/P for $60 \leq E \leq 70$ GeV. $\langle E \rangle$=64.7 GeV. (a) $E_1/E_{GEN}$ (Monte Carlo), (b) $E_{GEN}/P_1$ (Monte Carlo), (c) $E_1/P_1$ (Monte Carlo), (d) $E/P$ (Data).

a tracking resolution of $\sigma_P/P \simeq 0.18\% \times P$ and an EMLAC resolution of $\sigma_E/E \simeq 40\%\sqrt{E}$. In all three regions, the error on the mean of the fits to the Monte Carlo data is at the level of $0.1\% \times \sigma$.

### 4.4.2 E/P vs P

For the studies in this section, we take electrons from the sample of ZMPs in which both tracks match with showers. We will begin by discussing the low energy region of the E/P vs P plot.

In Figures 4.10, 4.11 and 4.12 we saw that the mean of the E/P distribution was less than 1.0. As mentioned, this is a result of energy being lost in the back section which has not been sufficiently accounted for in the shower reconstruction. It should be noted that since electrons begin their shower development sooner than photons, this effect may be less important for a photon-based analysis.

The deviation of the mean of the E/P distribution from 1.0 may be explained by any combination of the following situations: EMLAC energy scale, EMLAC energy loss, shower reconstruction or tracking momentum scale or tracking reconstruction problems.

The EMLAC energy scale has been tuned only to the $\pi^0$ mass (at the mean $\pi^0$ energy), which is a less than ideal situation. There is also the issue of energy loss; we will show that there are substantial problems of this nature in the low energy region.

Since the $K^o$, $\Lambda$ and $J/\psi$ masses are very close to their world average values, one has a certain degree of confidence in the scale of the tracking

system. The width of these mass distributions would give an indication of the resolution at specific track momenta. Unfortunately, we do not yet have sufficient statistics to divide the data into highly symmetric decay geometries which would be required to perform this analysis properly. We will show that this statement of confidence in the momentum scale has some qualifiers, especially in the high momentum region.

The mean of the E/P distribution varies in a uniform manner with momentum as shown in Figure 4.14a. Our resolution for low momentum tracks is very good so we may be quite confident in this quantity in the low-P region (see Figure 4.11b). As we increase the momentum, the mean approaches the expected value of 1.0. Figure 4.14b shows the same distribution for E/P extended out to 200 GeV.

The energy loss problems are evident out to around 30 GeV. Beyond about 100 GeV, we see the means of the E/P distributions begin to drop off again. The energy loss in the low momentum region may be described by showering before the EMLAC. The GEANT electrons follow the data rather well in the low momentum region.

The high momentum drop-off may be simulated completely by the simple Monte Carlo described in Section 4.4.1. Although this should be reproduced in the GEANT-based, full shower Monte Carlo, we have not yet generated enough events to investigate the high end of the spectrum. Nonetheless, the simple Monte Carlo follows the drop-off observed in the data at high momentum.

This bend-over at high momentum becomes intuitively obvious as fol-

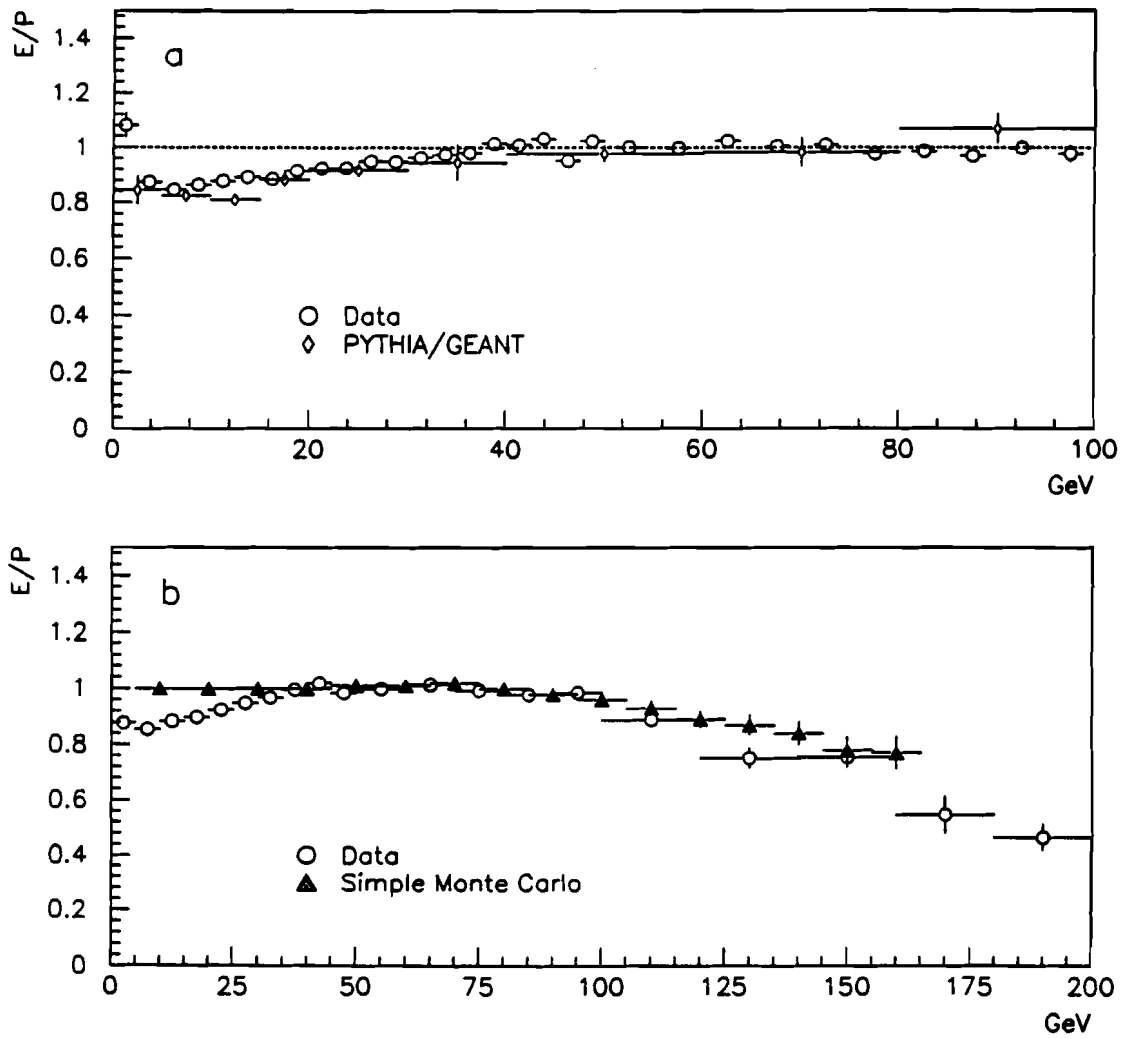


Figure 4.14: E/P vs P. (a) $0 \leq P \leq 100$ GeV; the Monte Carlo data are from full GEANT showers with PYTHIA generated high $p_T$ events. Due to the limited Monte Carlo statistics, we can compare only the low momentum region. (b) $0 \leq P \leq 200$ GeV; the Monte Carlo data are from the simple Monte Carlo described in the text. Since this scheme only accounts for intrinsic detector resolution, it is valid only in the high momentum region.

lows: an error in measurement which *decreases* the bend angle generates a *larger* momentum than an equivalent measurement error which *increases* the bend angle generates a *smaller* momentum. Perhaps a specific example is in order. Consider a 150 GeV track which corresponds to a bend angle of 3 mr. It is equally probable to measure this angle as 2 mr as it is to measure it 4 mr. But a bend angle of 2 mr corresponds to a calculated momentum of 225 GeV (+50% error) while 4 mr corresponds to a calculated momentum of 113 GeV (-25% error). This tends to flatten the energy spectrum and to produce tracks at momenta which are larger than the true values.

Another possible source for the high momentum drop-off is a falling spectrum. Any change in the real value of the momentum will make a more significant effect on less populated (higher momentum) bins. Alternatively, any change in the momentum which makes it smaller will have a less significant effect on the smaller bin.

This high momentum drop-off may also be explained by either an energy scale problem or by a momentum scale problem in which one or the other (or both) of these is energy or momentum dependent. Since we have some constraints (mass plots) on these quantities, we conclude that the explanation is resolution.

If we change the abscissa from P to E for the means of the E/P distributions. the problems at high energies disappear; see Figure 4.15. This is entirely consistent with the resolution problem conjecture while the other schemes. especially the scale explanations, fail to describe these plots.

An alternative view of the momentum dependence of $E/P$ is shown in

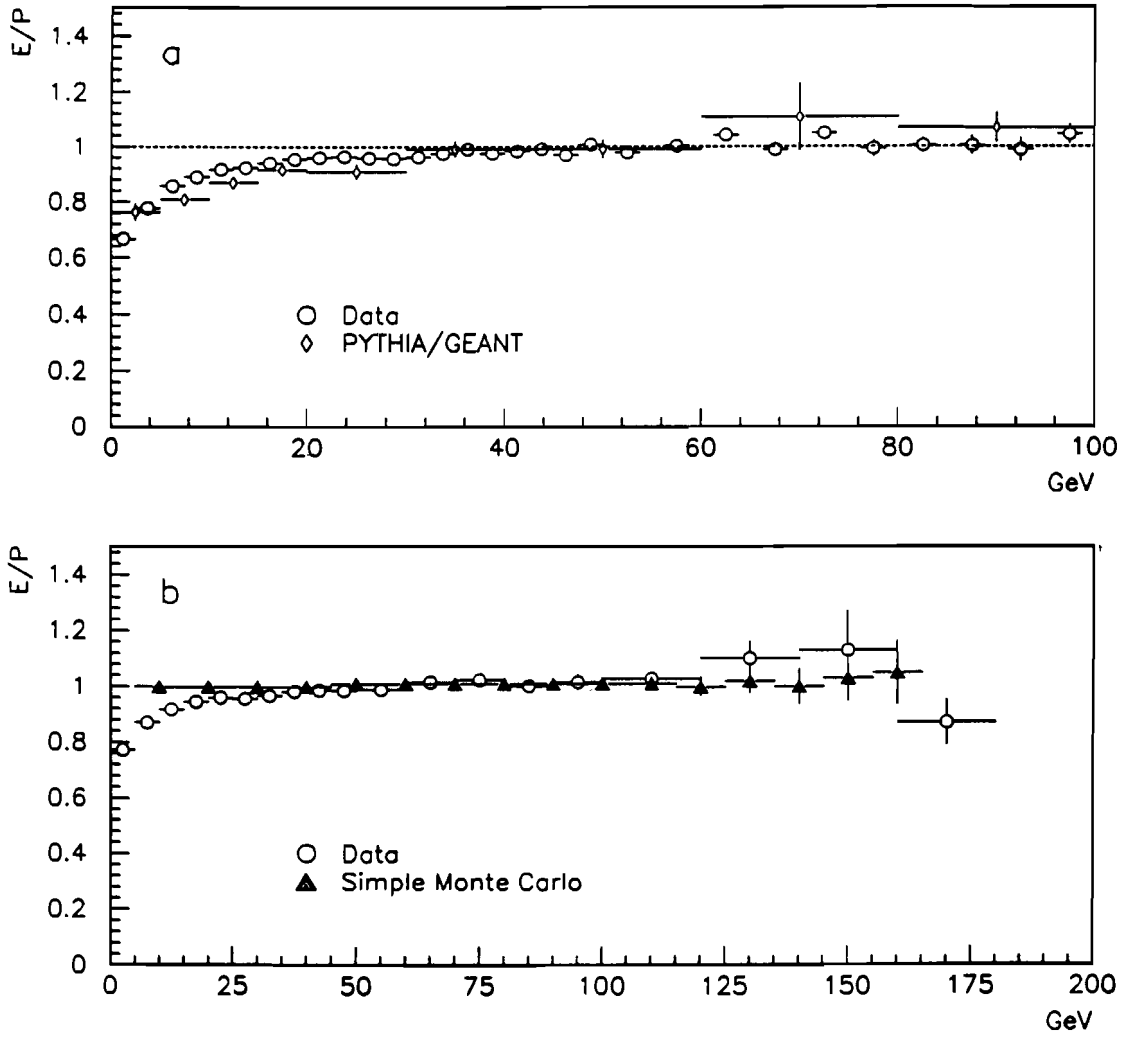


Figure 4.15: E/P vs E. (a) $0 \leq E \leq 100$ GeV; the Monte Carlo data are from full GEANT showers with PYTHIA generated high $p_T$ events. Due to the limited Monte Carlo statistics, we can compare only the low energy region. (b) $0 \leq E \leq 200$ GeV; the Monte Carlo data are from the simple Monte Carlo described in the text. Since this scheme only accounts for intrinsic detector resolution, it is valid only in the high energy region.

Figure 4.16 where the abscissa is now $1/P$ (often referred to as the *curvature*). The motivation for this lies in the fact that the variable $P$ is not truely Gaussian but the curvature is. In Figure 4.16 the momentum range extends from about 250 GeV to 40 GeV. We have used the same momentum resolution for the Monte Carlo as for the previous plots ($\sigma_P/P \simeq 0.18\% \times P$). These data imply that the simulated momentum resolution does not yet match the experimental data. Since the Monte Carlo resolution has to be degraded by about twice the design resolution. this result is still under active investigation. It is believed that the technique described here contains some as yet unobserved flaw.

## 4.5 EMLAC Efficiency

Beginning with a sample of ZMP electrons in which at least one of the tracks matches with a shower (control track), we may now ask how frequently the other (test track) matches with a shower. We will investigate this efficiency as a function of track momentum while applying cuts to both control and test tracking parameters and to the control-side shower parameters.

From our earlier discussion on energy loss due to pre-LAC showering. we may expect some inefficiency at low energies. Figure 4.17 shows the momentum dependent efficiency of finding a shower as defined by the following constraints:

- Require at least one match of the ZMP pair,
- Tight tracking ZMP cuts: $\Delta S_Y \leq 1.5$ mr and ZXI $= 199.3 \pm 5.0$ cm.

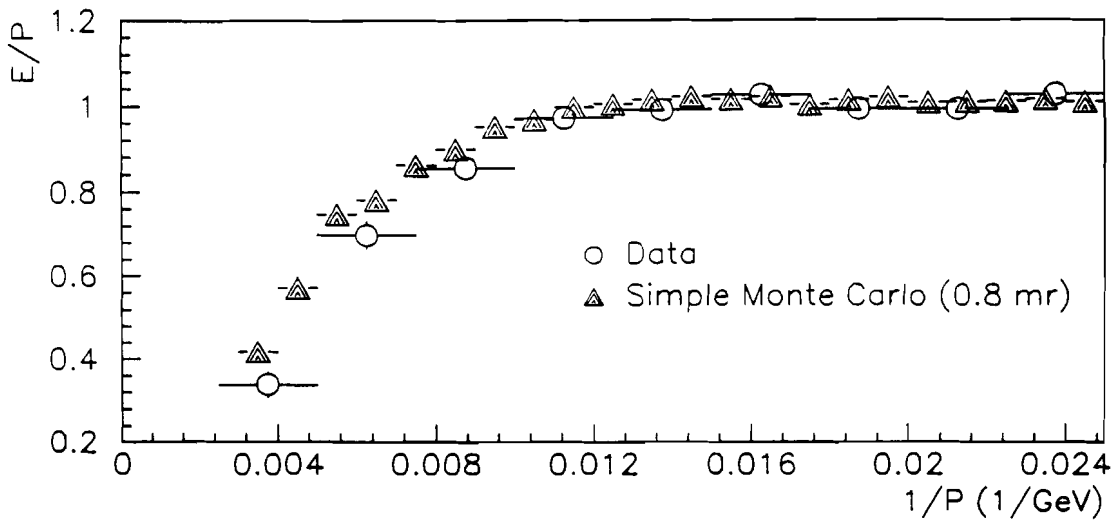


Figure 4.16: E/P vs 1/P. The true Gaussian variable in the momentum measurement is the bend angle, $\theta$, which is proportional to 1/P. Here we compare the E/P results of the simple Monte Carlo to data in the range 40 GeV and above. For the Monte Carlo tracking resolution we have used $\sigma_\theta$ = 0.8 mrad.

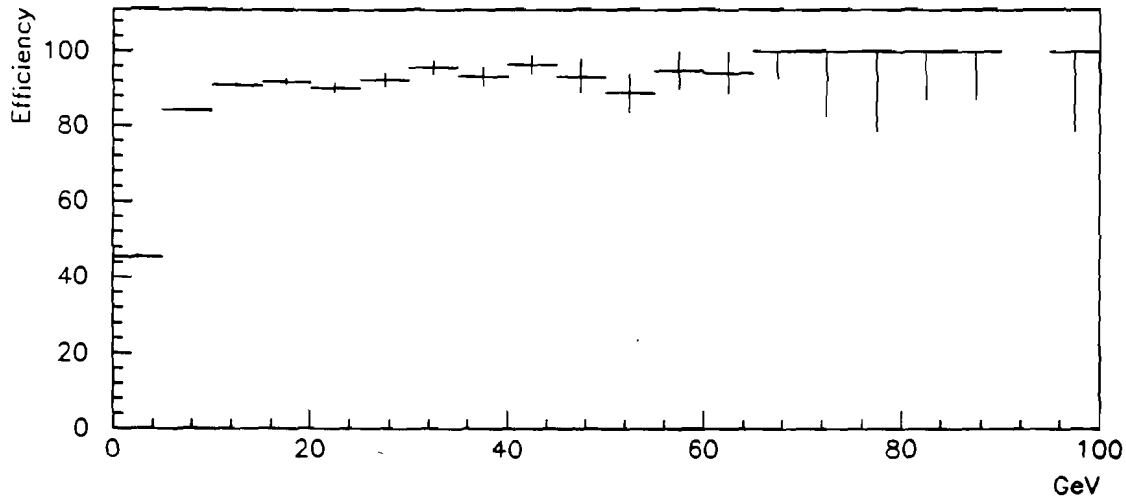


Figure 4.17: EMLAC Efficiency vs Momentum

- EM cuts on the control electron.

Although the nature of this efficiency distribution is not well understood, we will assume that its influence is small since most high $p_T$ showers have energies greater than 20 GeV.

# Chapter 5

# Analysis of the $\pi^o$ Pair Events

We will present the results of the $\pi^o$ pair triggered data in three parts. Beginning with a discussion of the general features of events of this nature, we will define the variables which we have chosen to use in the analysis and show the raw distributions of these quantities. In a section on event structure, we will present results from the tracking system which indicate a correlation between the $\pi^o$s and charged tracks. Having established that the $\pi^o$s leave the interaction region with a large fraction of the parton momentum, we will then move on to the section on $\pi^o$ pairs, in which we show the inclusive cross section for the production of such events. We will compare the cross section with other data in a scaled format and with leading-log QCD Monte Carlo predictions. We will end the chapter with evidence that $\pi^o$ pairs, as produced and detected in this experiment, are generated primarily from gluons in the incident beam.

## 5.1 General Features of the $\pi^o$ Pair Events

The plots in Figure 5.1 show the raw distributions for three quantities as produced in the two beams hitting the beryllium target (no $\pi^o$ pair cuts have been applied to these plots). The histograms on the left (Figure 5.1a, c and e) correspond to events generated by the negative beam ($\pi^- + Be \rightarrow \pi^o\pi^o + X$) and those on the right (Figure 5.1b, d and f) to the positive beam ($p + Be \rightarrow \pi^o\pi^o + X$ ). The primary variable of interest to us in this analysis is the invariant mass of the $\pi^o\pi^o$ system. These mass distributions are on the top (Figures 5.1a and 5.1b). Figures 5.1c and 5.1d show the transverse momentum of the $\pi^o$ pair system while Figures 5.1e and 5.1f show the distributions in rapidity (see Equation 5.2). We see that, at this level, the raw plots are quite similar and largely independent of beam type.

In Table 5.1 we show the raw number of $\pi^o$ pairs vs. mass after the cuts described in Section 5.3.4. Similarly, in Table 5.2 we show how the $\pi^o$ pairs were distributed in $p_T$.

In the frame of reference where the $\pi^o$ pairs have zero net longitudinal momentum, each $\pi^o$ makes an angle $\theta_i^*$ with respect to the beam (z) axis. We define a variable, $\cos\theta^*$, as the average of the absolute value of the cosines of the two $\pi^o$s as measured in this frame:

$$\cos\theta^* \equiv \frac{1}{2}(\mid \cos\theta_1^* \mid + \mid \cos\theta_2^* \mid). \tag{5.1}$$

Although we will be limited (by the detector acceptance) in our measurement of this scattering angle, we will apply cuts to the distribution for

Table 5.1: Number of Raw $\pi^0$ Pairs Distributed in Mass; these numbers are those events which remain after the cuts described in Section 5.3.4; no corrections have been applied.

| Mass Range (GeV) | 4–5 | 5–6 | 6–7 | 7–8 | 8–9 | $\geq 9$ |
|---|---|---|---|---|---|---|
| Positive Beam | 503 | 291 | 66 | 19 | 4 | 0 |
| Negative Beam | 293 | 178 | 58 | 17 | 5 | 5 |

Table 5.2: Number of Raw $\pi^0$ Pairs Distributed in $p_T$; these numbers are those events which remain after the cuts described in Section 5.3.4; no corrections have been applied.

| Positive Beam | | | | |
|---|---|---|---|---|
| $p_{T1}$ | 2–3 | 3–4 | 4–5 | $\geq 5$ |
| $p_{T2}$ | | | | |
| 2–3 | 641 | 188 | 24 | 2 |
| 3–3 | 0 | 17 | 10 | 1 |
| 4–3 | 0 | 0 | 0 | 0 |
| $\geq 5$ | 0 | 0 | 0 | 0 |

| Negative Beam | | | | |
|---|---|---|---|---|
| $p_{T1}$ | 2–3 | 3–4 | 4–5 | $\geq 5$ |
| $p_{T2}$ | | | | |
| 2–3 | 370 | 132 | 20 | 1 |
| 3–3 | 0 | 15 | 11 | 3 |
| 4–3 | 0 | 0 | 1 | 2 |
| $\geq 5$ | 0 | 0 | 0 | 1 |

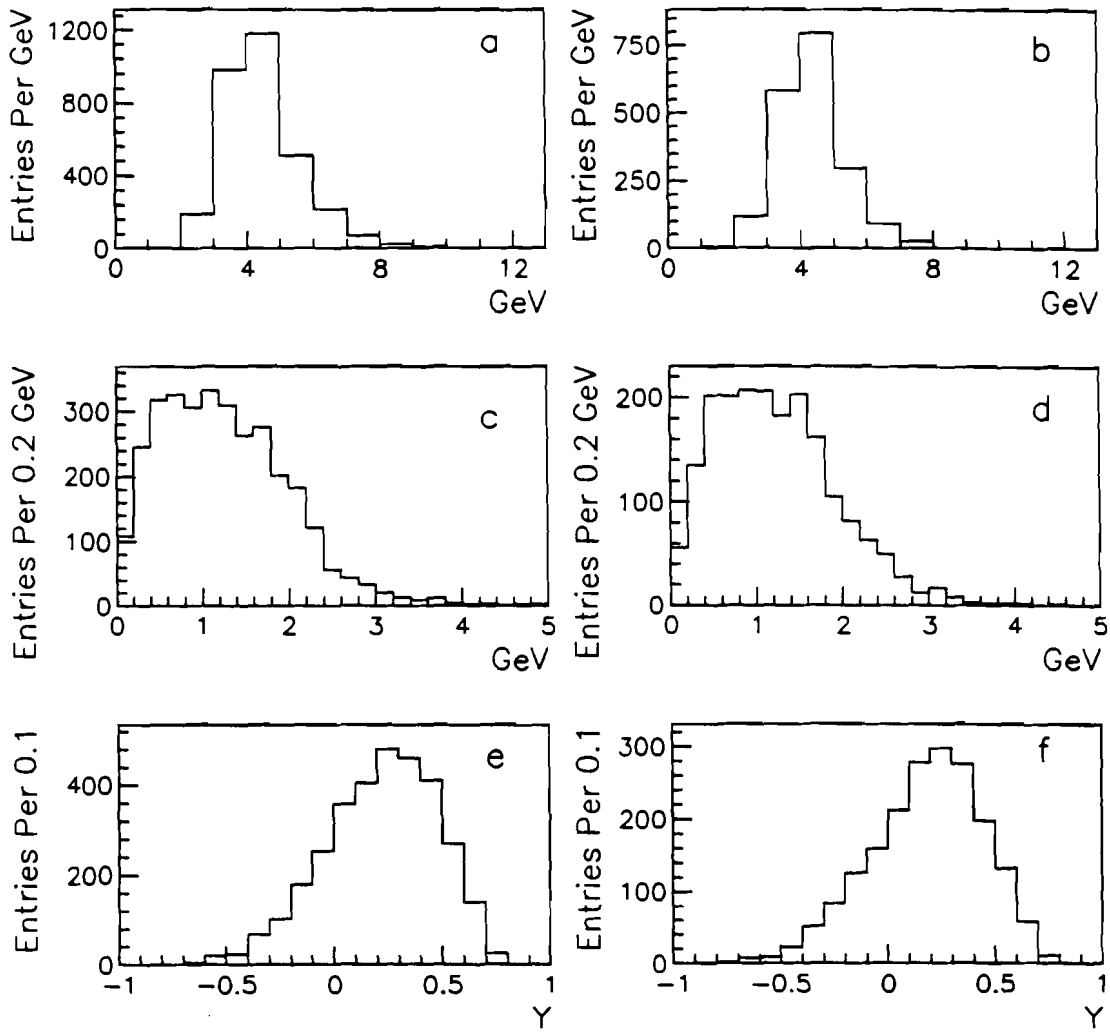


Figure 5.1: Raw Mass, $p_T$ and Rapidity Distributions for Observed $\pi^0$ Pair Events. (a and b) Mass, (c and d) $p_T$ and (e and f) Rapidity. The left side plots were produced by the negative beam and those on the right by the positive beam: all with the beryllium target.

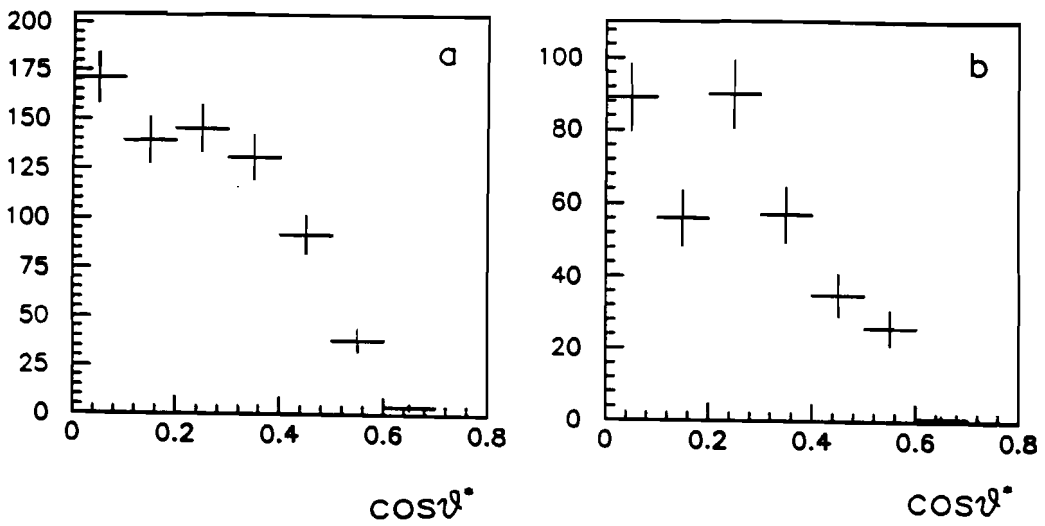


Figure 5.2: Raw $\cos\theta^*$ Distributions. (a) from the negative beam and (b) is from the positive beam.

comparison with other data. The raw distributions in $\cos\theta^*$ as generated by the negative and positive beams are shown in Figures 5.2a and 5.2b, respectively.

## 5.2 Event Structure

Defining jets at the energies available in fixed target experiments ($\sqrt{s} \simeq$ 30–40 GeV) tends to be a rather controversial endeavor. As many others have done before, we will show evidence for jet–like structure, see Figure 5.3. Unfortunately, the same evidence will be consistent with the kinematic constraint of conservation of momentum. Nonetheless, we will begin with correlations in azimuth and then move on to distributions in rapidity.

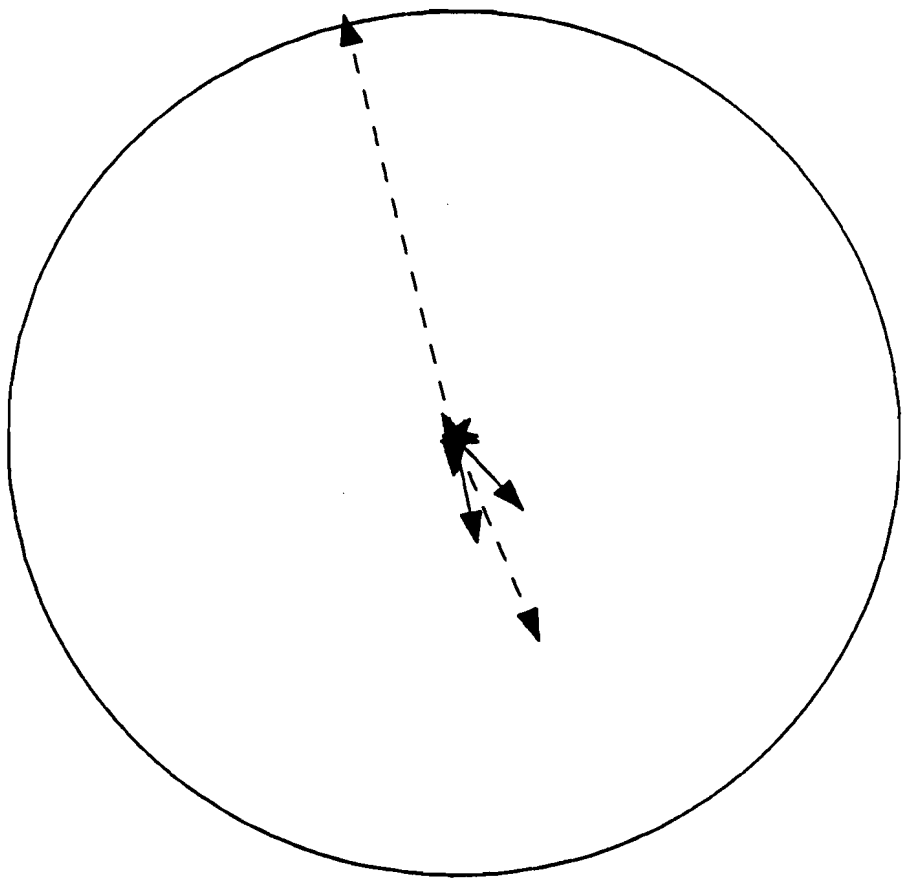

Figure 5.3: $\pi^0$ Pair Event and Associated Particles. The particle $p_T$ is proportional to the length of the arrows and the $\pi^0$s are indicated by the dashed lines where the highest $p_T = 7$ GeV. The away side $\pi^0$ has $p_T = 3.4$ GeV. The arrows with solid lines correspond to associated charged particles.

### 5.2.1 Azimuthal Correlations

Although not all events are as visually striking as that shown in Figure 5.3, the azimuthal correlations are consistent with this picture. Defining $\Delta\phi_i$ as that angle between the highest $p_T$ triggered $\pi^o$ and the ith track, we show the quantity, $\Delta\phi$, for all tracks with $p_T \leq 0.3$ GeV in Figure 5.4a. $\Delta\phi = 0^o$ corresponds to the direction of the highest $p_T$ $\pi^o$ while $\Delta\phi = 180^o$ is in the opposite direction. We see that this distribution is quite flat across the entire range: low $p_T$ charged tracks show very little correlation with the production of a high $p_T$ $\pi^o$.

In Figure 5.4b, we select only those tracks with $p_T \geq 0.3$ GeV. Not only do we see some correlation in the $\pi^o$ direction, we see that there tends to be a higher density of associated particles along the direction opposite the higher $p_T$ $\pi^o$ . This is completely consistent with and expected from a conservation of momentum argument; it is also consistent with a dynamical jet-production interpretation as described by QCD.

The histograms in Figure 5.4c and 5.4d show the same $\Delta\phi$ distributions with the associated particle $p_T \geq 1.0$ and 2.0 GeV, respectively. It is clear from these plots that there is a very strong correlation between particles produced in association with the high $p_T$ $\pi^o$s. It is also evident that as the transverse momentum of the charged particles increases, they are more likely to be associated with one of the $\pi^o$s. All of these plots are raw in the sense that they have not been corrected for detector inefficiencies. Since the $p_T$ spectrum for the $\pi^o$s is steeply falling (see Figure 3.10), these distributions

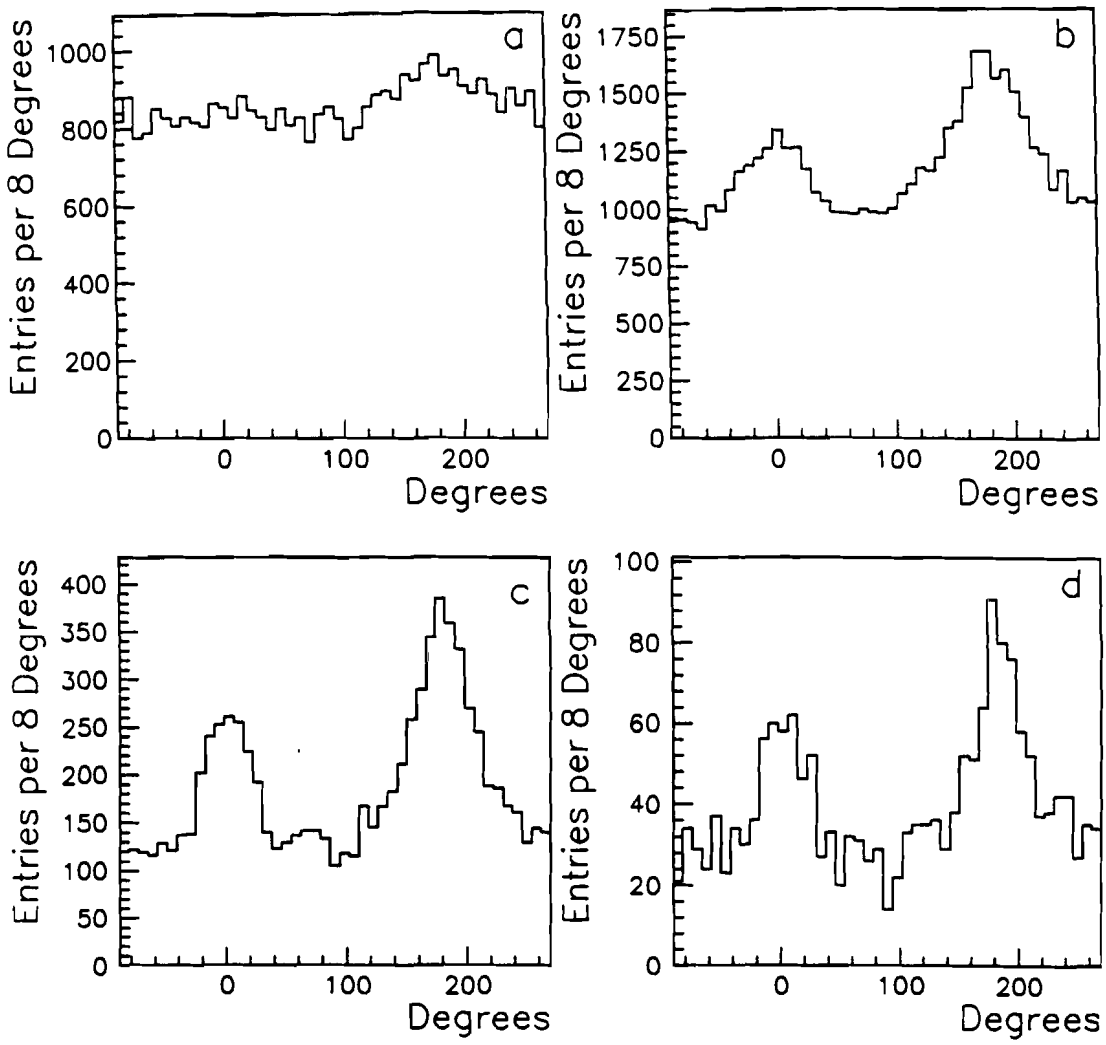


Figure 5.4: Azimuthal Correlations. $\Delta\phi$ is defined as the angle between the highest $p_T$ $\pi^0$ and the associated charged particles. (a) track $p_T \leq 0.3$ Gev, (b) track $p_T \geq 0.3$ Gev, (c) track $p_T \geq 1$ Gev, (d) track $p_T \geq 2$ Gev.

are dominated by the events with low $p_T$. This should be kept in mind for this and subsequent discussions of distributions in which integrations have been performed over the $p_T$ variable.

### 5.2.2 Rapidity Correlations

As opposed to the transverse variable, $\Delta\phi$, rapidity, Y, is a longitudinal quantity defined as

$$Y = \frac{1}{2}\ln\left(\frac{E + p_L}{E - p_L}\right) \tag{5.2}$$

where E is the particle energy and $p_L$ is the longitudinal component of momentum. For $p_T \gg m$, this reduces to

$$Y \simeq \eta \equiv -\ln\left(\tan(\theta/2)\right) \tag{5.3}$$

where $\theta$ is the polar angle as measured with respect to the beam axis. Equation 5.3 gives the definition of pseudo-rapidity and its form offers some intuition into the behaviour of rapidity.

The uncorrected rapidity distribution for the $\pi^o$s is shown in Figure 5.5a where the range is limited by the detector acceptance. This distribution is rather flat across the range $-0.3 \leq Y \leq +0.8$; in the backwards rapidity region ($Y \leq -0.3$), the shape is not as uniform as in the forward region. This is due to pre-trigger inefficiencies.

Figure 5.5b shows the raw rapidity distribution for all charged tracks observed in the $\pi^o$ pair events. This distribution is strongly peaked at

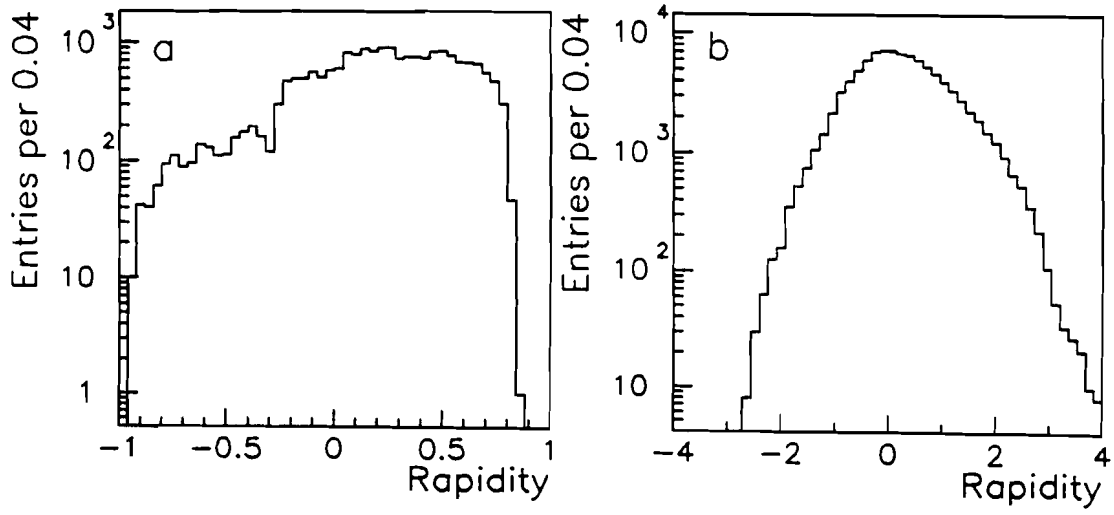


Figure 5.5: Rapidity Distributions for $\pi^o$s and Associated Particles. These plots have not been corrected for detector inefficiencies and the associated particles are limited to charged tracks; (a) $\pi^o$s and (b) associated particles.

$\theta \simeq 90^o(Y \simeq 0)$ relative to the beam. Similar to the scheme employed for looking at azimuthal correlations, we will look at the differences in rapidity between the highest $p_T$ $\pi^o$ and all tracks, $\Delta Y$.

Since the differences in rapidity are somewhat more subtle that those in azimuth, we will use a simple Monte Carlo to generate a background distribution to use for comparison. For the Monte Carlo, we use as input the observed $\pi^o$ and charged particle $p_T$ and rapidity distributions along with the charged particle multiplicity distribution. For the following $\Delta Y$ plots, we generated $10^5$ events. For each event, a pair of $\pi^o$s were generated each with $p_T$ and rapidity selected at random from the input histograms and the number of charged tracks was generated from the charged particle multiplicity histogram. For each track, a rapidity was selected and the $\Delta Y$ plots were created. We assume here that the events generated in this rather simple Monte Carlo are similar to a sample of unbiased associated particles.

Figure 5.6a displays the $\Delta Y$ distribution observed between the highest $p_T$ $\pi^o$ and all charged tracks with $p_T \geq 1$ GeV. The data are represented by the points with error bars and the overlying histogram is the Monte Carlo result (the Monte Carlo errors are about 1/10 that of the data). Both the data and the Monte Carlo distributions have been normalized to the number of events. A signal indicating that the produced charged particles tend to accompany the $\pi^o$s in rapidity is quite clear at $\Delta Y = 0$. Figure 5.6b is the difference between the data and the Monte Carlo. Similarly, Figure 5.6c and d show the plots for charged particle $p_T \geq 2$ GeV. The signal here is less

convincing than that for the particles with $p_T \geq 1$ GeV, as was also observed in the azimuthal plots of Figure 5.4c and d.

To further confirm that the associated charged particles tend to follow the high $p_T$ $\pi^o$s we present the *rapidity* (not $\Delta Y$) plots in Figure 5.7. For these plots we have used information obtained from Figure 5.4 and we select only those charged particles which are on the away-side of the higher $p_T$ $\pi^o$ of the pair defined as $\Delta\phi = 180^o \pm 30^o$. Again, we have normalized to the number of events and Figure 5.7a shows both the data (points with error bars) and the Monte Carlo (histogram). Figure 5.7b shows the data with the Monte Carlo histogram subtracted. The signal is substantial as compared to the background. Taking the exercise yet one step further, we now place a rapidity constraint on the *lower* $p_T$ $\pi^o$, requiring that it be in the range Y = (0.5,0.8). The result is shown in Figure 5.7c and d. We see that the distribution is skewed, relative to the generated background, to higher rapidities. We have chosen to look at tracks along the direction of the lower $p_T$ $\pi^o$ simply because there tends to be more tracks which accompany it; see Figure 5.4.

### 5.2.3 Y-$\phi$ Definition of Jets

It is now clear that in the symmetrically triggered events, we see strong correlations in both azimuth and rapidity between charged particles and the leading $\pi^o$s. We will now select charged particles in Y-$\phi$ space and and ask how much of the total transverse momentum in this cone is carried by the $\pi^o$.

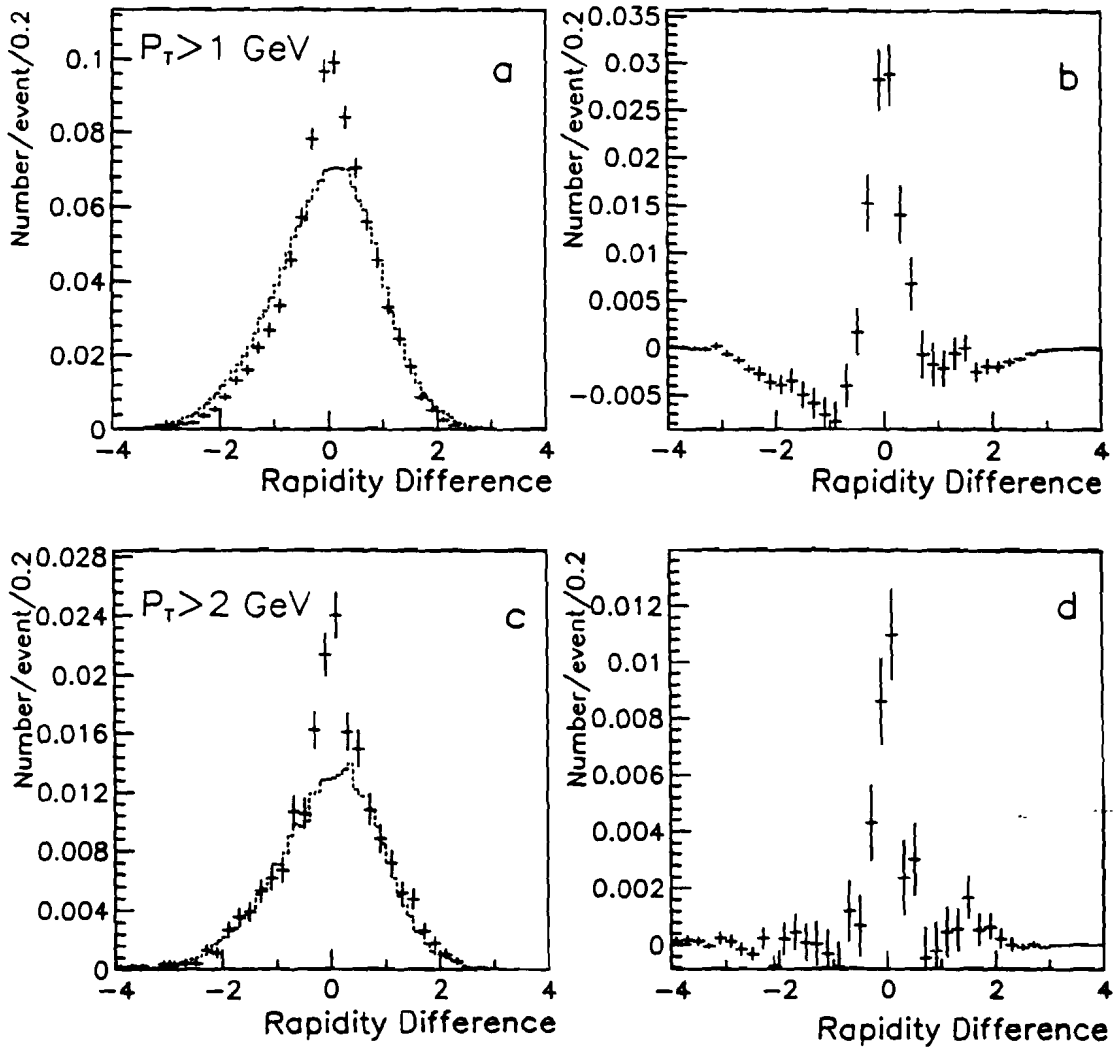


Figure 5.6: Rapidity Difference Correlations. Difference in Rapidity between the trigger $\pi^0$ and charged tracks. (a, b) $p_T$(track)$\geq$1 GeV and (c and d) $p_T$(track)$\geq$2 GeV. The dotted line is a Monte Carlo result for uncorrelated $\pi^0$s and tracks which is described in the text; the raw distributions (normalized to the number of events) are on the left (a, c) and the differences are on the right (b, d).

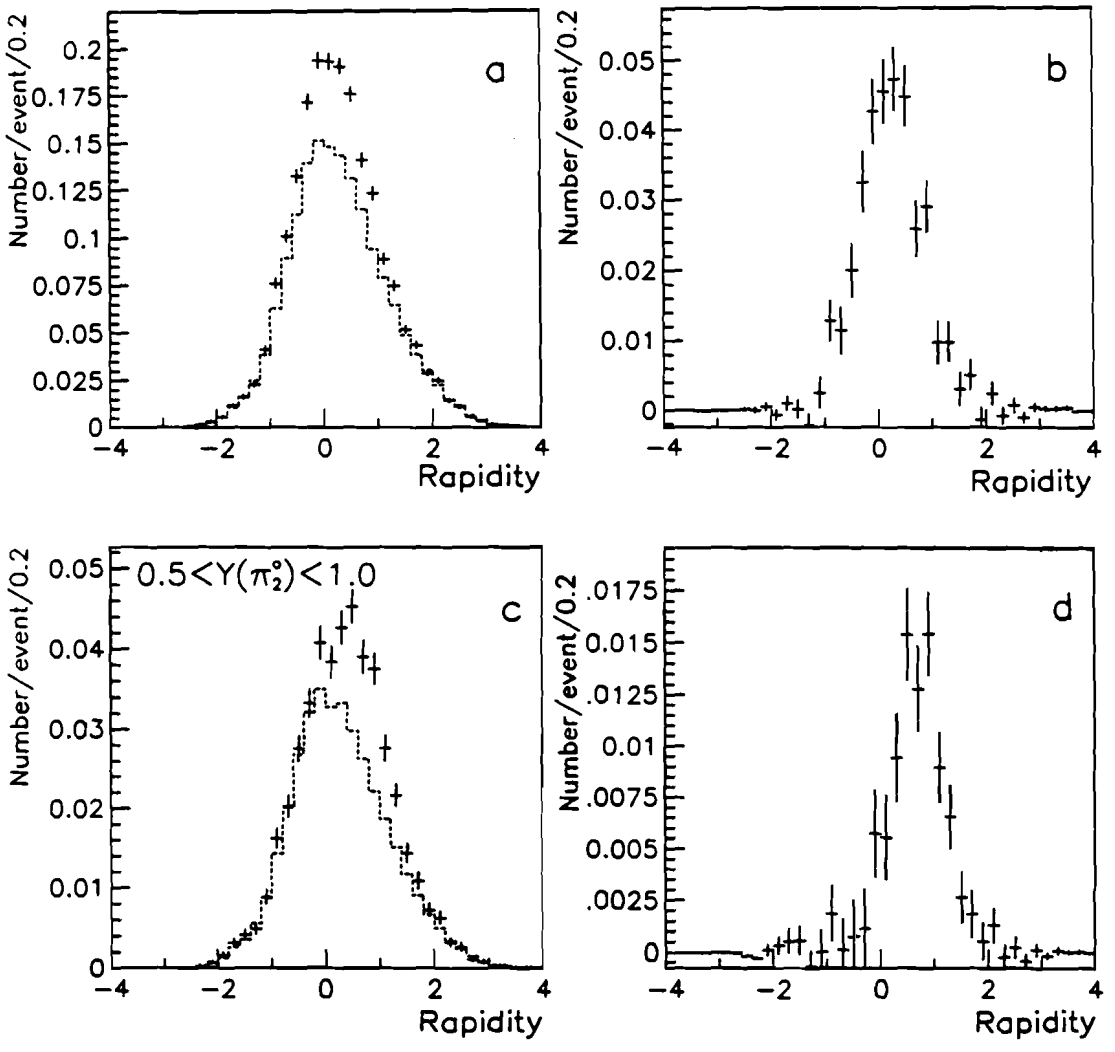


Figure 5.7: Rapidity Correlations. Rapidity distributions for tracks with $p_T \geq$ 300 MeV and within 30° in azimuth of the *lower* $p_T$ $\pi^o$. The dashed line is the Monte Carlo result for uncorrelated $\pi^o$s and tracks; the raw distributions are on the left (a, c) and the distribution differences are on the right (b, d). (a, b) no constraint on the $\pi^o$ rapidity. (c, d) $0.05 \leq Y(\pi^o) \leq 0.8$.

The scheme employed here is very simple. We define a variable, $R$, which is a radius in rapidity-$\phi$ space:

$$R \equiv \sqrt{(\Delta\phi)^2 - (\Delta Y)^2} \leq 1.0 \tag{5.4}$$

where $\Delta\phi$ and $\Delta Y$ are now measured relative to both $\pi^o$s. In this case, we measure $\Delta\phi$ in radians and define a jet as all charged tracks within the region where $R \leq 1.0$. Recalling that 1 radian $\simeq$ 57 degrees, we see that this includes the tracks in the peaks of Figure 5.4c, and Figures 5.6b and 5.6d.

We now define Z($\pi^o$) as the fraction of the jet transverse momentum carried by the $\pi^o$:

$$\begin{aligned} Z(\pi^o) &\equiv p_T(\pi^o)/p_T(JET) \\ &= \frac{p_T(\pi^o)}{p_T(\pi^o) + \sum p_x} \\ &= \frac{1}{1 + \sum x_e} \end{aligned} \tag{5.5}$$

where the sums are over all tracks within the cuts. The quantity $p_x$ is the component of track transverse momentum along the direction of the $\pi^o$, and $x_e = p_x/p_T(\pi^o)$. In Figure 5.8a, we show the dependence of the mean of this ratio, $\langle Z(\pi^o)\rangle$ , as a function of the $\pi^o$ $p_T$. It behaves largely as one would intuitively expect; the $\pi^o$ carries more of the jet transverse momentum as the $\pi^o$ $p_T$ increases. Also shown are the results from an ISR experiment[4] which was dedicated to studying high transverse momentum

phenomena through single $\pi^o$ and $\pi^o$ pair production at $\sqrt{s}$ = 31, 45 and 63 GeV. Although the data are similar, there are some differences. First of all, the jet definitions differ. The CCOR jet is defined as all tracks within 60° in azimuth with $p_T \geq$ 0.3 GeV and $|Y| \leq$ 0.7. The sum over $x_e$ was then multiplied by 1.5 to account for missing neutral energy. As a result, the CCOR data is expected to lie somewhat below our data, although the difference is small: at $p_T$= 5 GeV, the CCOR point is 3% lower than our data. This was determined by applying the CCOR cuts to our data.

An easier comparison is made when $p_T$ is scaled as

$$x_T \equiv \frac{2p_T}{\sqrt{s}} \tag{5.6}$$

as shown in Figure 5.8b. Two things are clear from these plots: the $\pi^o$s are a very good approximation to the jet direction and the data are relatively insensitive to the exact definition of the jet. At the same center of mass energy, we see behavior very similar to that observed in a collider-type experiment (ISR) and our data scale with the ISR data of different center of mass energies.

### 5.2.4 Charged Particle Multiplicity in the Jets

We saw in Figure 5.8 that the fraction of the jet's transverse momentum carried by the $\pi^o$ increased as the $\pi^o$ $p_T$ increased. The mean number of charged particles, $\langle n_{CH} \rangle$, in the jet which accompanies the higher $p_T$ $\pi^o$ of the pair is $\langle n_{CH} \rangle$ = 1.51 ± 0.02 while that for the lower $p_T$ $\pi^o$ is $\langle n_{CH} \rangle$ = 1.74 ± 0.02. This implies that, on average, when the $\pi^o$ $p_T$ is lower,

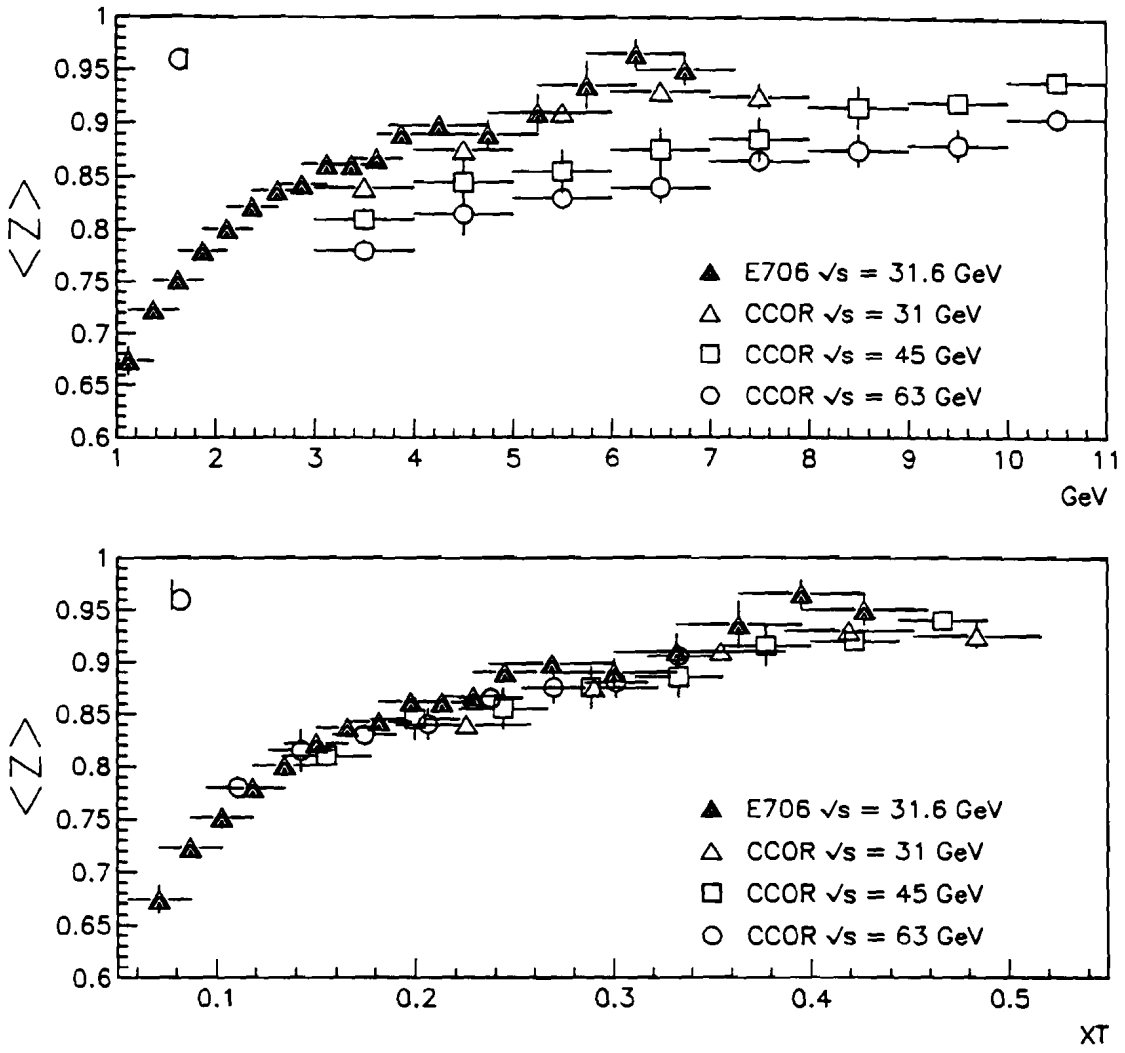


Figure 5.8: $\langle Z(\pi^o)\rangle$ vs $p_T$ and $x_T$. (a) $\langle Z(\pi^o)\rangle$ vs $p_T(\pi^o)$ and (b) $\langle Z(\pi^o)\rangle$ vs $x_T(\pi^o)$. The ISR data are taken from Figures 1 and 2 of reference [4].

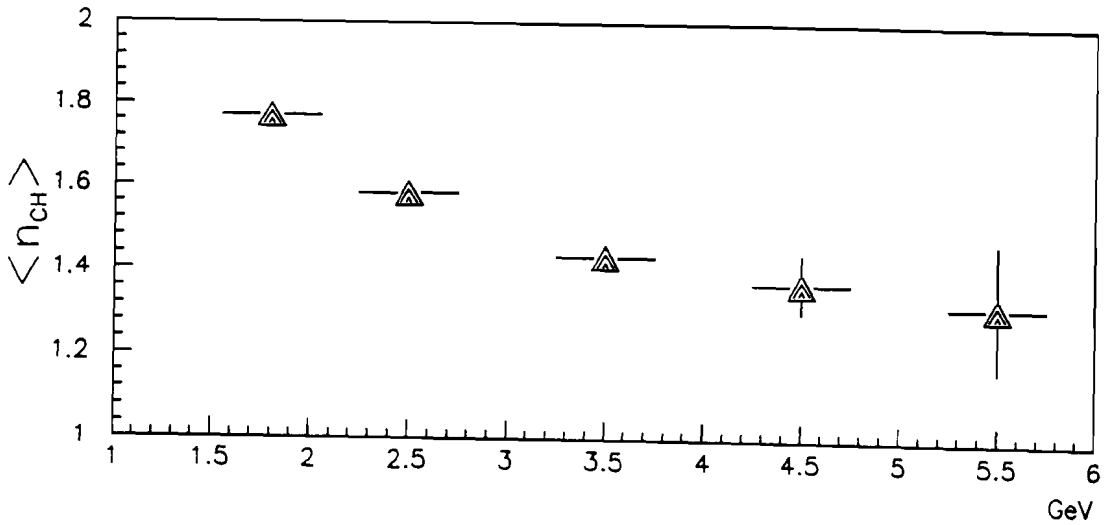


Figure 5.9: $\langle n_{CH} \rangle$ vs $p_T(\pi^o)$. As the $\pi^o$ $p_T$ increases, the number of accompanying charged particles decreases.

the number of accompanying charged tracks increases, and vice-versa. If we select events in bins of $\pi^o$ $p_T$, and look at the charged track multiplicity, we see that this trend continues, see Figure 5.9. One may interpret this as follows: we tend to trigger on jets of approximately constant transverse momentum and that this jet $p_T$ is being distributed amongst its products in such a manner that the charged particle multiplicity decreases with increasing $\pi^o$ $p_T$.

## 5.3 $\pi^o$ Pairs

In this section on $\pi^o$ pairs, we will begin by discussing the selection of and corrections to the data. We described the selection of single $\pi^o$s in Section 3.4.4; here we extend this discussion to the selection of pairs. We will follow this with the $\pi^o$ pair mass spectrum with the accompanying QCD predictions.

### 5.3.1 Selection of $\pi^o$ Pair Events

The second pass analysis proceeded from the sample of TWO GAMMA events written in the final data summary tape (DST) format. This corresponds to about 5% of all of the E706 events written to tape.

The vertex requirement reduced the DST sample by about 14%. With about 1% of an interaction length of material which could cause an interaction outside of the target material *and* pass our hardware definition of an interaction, this corresponds to a vertex reconstruction efficiency of about 87%.

### 5.3.2 Background Subtraction

A $\pi^o$ is defined as any $\gamma\gamma$ combination satisfying the cuts defined in Section 3.4.4 in which the effective mass falls in the range defined by region $A$ in Figure 3.12. For the purpose generating a background-free spectrum, the background is taken from the two ranges $B$ and $C$, also defined in Figure 3.12. The assumption is that the background events beneath the $\pi^o$

peak are very similar to the data in the two sideband regions.

In selecting a $\pi^o$ from one octant in an event. one is actually selecting $\gamma\gamma$ combinations which are part signal (i.e. a real $\pi^o$) and part background. We denote this situation as follows:

$$\gamma\gamma(1) = \pi^o{}_1 + \beta_1$$

for the first octant and similarly for the second octant,

$$\gamma\gamma(2) = \pi^o{}_2 + \beta_2.$$

In this notation, $\pi^o{}_i$ corresponds to the *signal* $\gamma\gamma$ combinations in octant $i$ and $\beta_i$ represents the *background* $\gamma\gamma$ combinations in octant $i$. For a pair of $\pi^o$s, then, we have

$$\gamma\gamma(1) * \gamma\gamma(2) = \pi^o{}_1\pi^o{}_2 - \pi^o{}_1\beta_2 - \beta_1\pi^o{}_2 - \beta_1\beta_2$$

Finally, for our background-free $\pi^o\pi^o$ distributions we have

$$\pi^o{}_1\pi^o{}_2 = \gamma\gamma(1) * \gamma\gamma(2) - \pi^o{}_1\beta_2 - \pi^o{}_2\beta_1 - \beta_1\beta_2 \qquad (5.7)$$

It may seem peculiar that the $\beta_1\beta_2$ is *added* to the $\pi^o{}_1\pi^o{}_2$ but these events are over subtracted in the other terms.

As evidence that we actually see pairs of $\pi^o$s in these events, we show in Figure 5.10, $\gamma\gamma$ combinations in the *second* (arbitrarily defined as that octant with the lower $p_T$ shower of the two trigger octants) octant of the TWO-GAMMA trigger. In the first octant we have required a $\gamma\gamma$ pair to be in either the $\pi^o$ region *or* in the sideband region. Figure 5.10a shows $\gamma\gamma$

combinations in the second octant while in the first octant, we have a $\gamma\gamma$ pair in the $\pi^o$ mass region. In Figure 5.10b we show the $\gamma\gamma$ combinations on the opposite side when the first side is in one of the sidebands.

All distributions exhibiting properties of $\pi^o$ pairs in subsequent sections will have the background subtracted as described above, unless otherwise indicated.

### 5.3.3 Distributions in $\cos\theta^*$

As described in Section 5.1, $\cos\theta^*$ is related to the dipion center of mass scattering angle as measured relative to the beam axis. In Figure 5.11, we show our $\cos\theta^*$ distribution which has been normalized to its value at $\theta^* = 90^o$ (first bin). Overlaying the data are the QCD predictions for the same quantity subject to the same cuts. Although the data are lacking of any striking features, the QCD points follow along quite well.

We will show that the shape of this distribution is very sensitive to the acceptance of the single $\pi^o$ rapidity. In Figure 5.12a we show the result of extending the single $\pi^o$ rapidity interval to the range: $|Y| \leq 1.0$, while in Figure 5.12b, we have extended the single $\pi^o$ rapidity range to $|Y| \leq 2.0$. Additionally, the range of $cos\theta^*$ which we can sample is limited by the lower $p_T$ cut which we were forced to place on the single $\pi^o$s.

### 5.3.4 Definition of the Cross Section

With a background free mass spectrum, we are now in position to calculate the cross section. We will begin with the definition as given by Richtmyer,

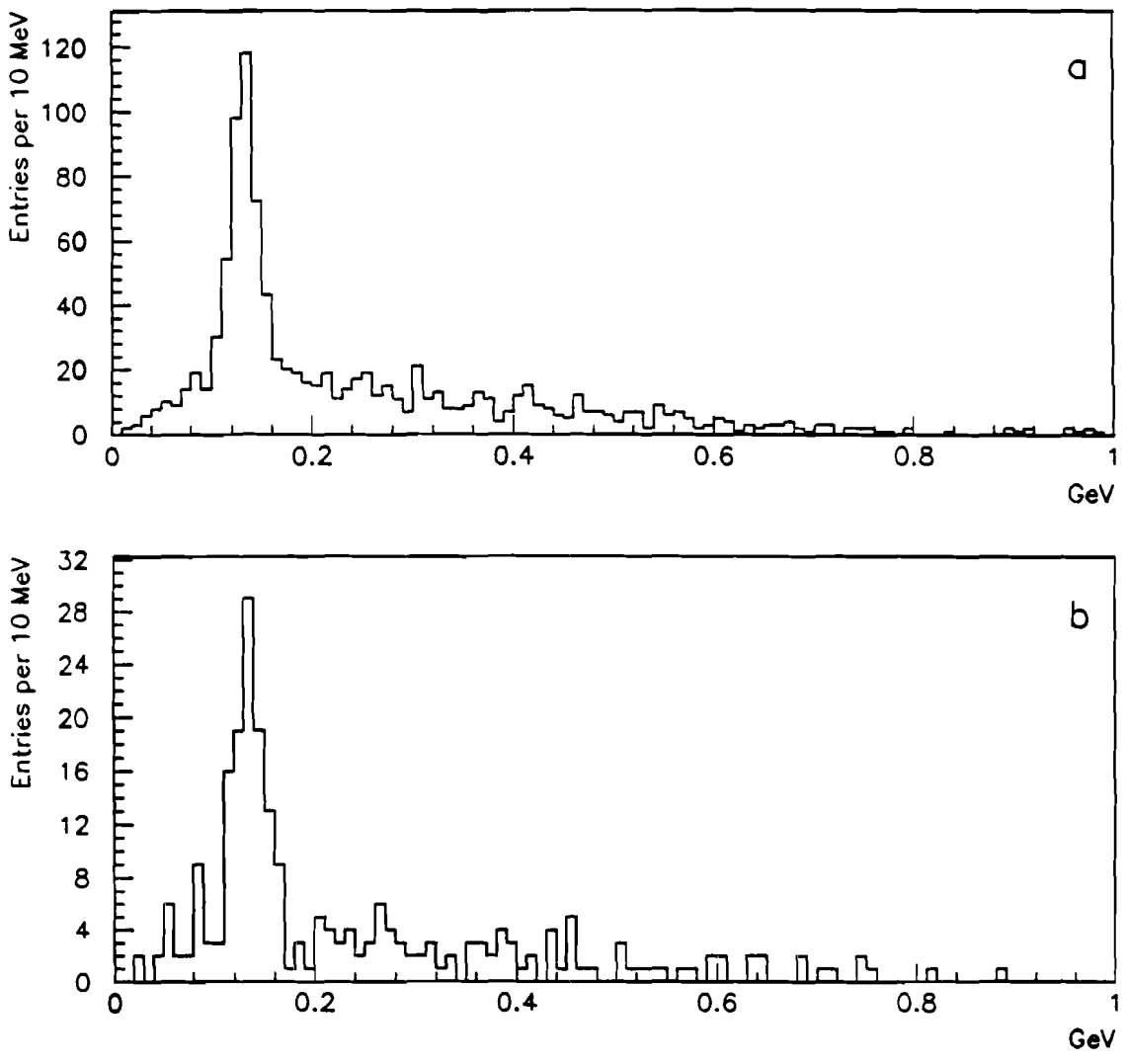


Figure 5.10: $\gamma\gamma$ Mass Plots for the *Opposite* Octant of the TWO-GAMMA Trigger. (a) a $\gamma\gamma$ combination was found in the $\pi^{o}$ mass region on the *other* side. (b) a $\gamma\gamma$ combination was found in the $\pi^{o}$ *sideband* region on the *other* side. The *other* side octant is arbitrarily defined here as that with the higher $p_T$ trigger-photon.

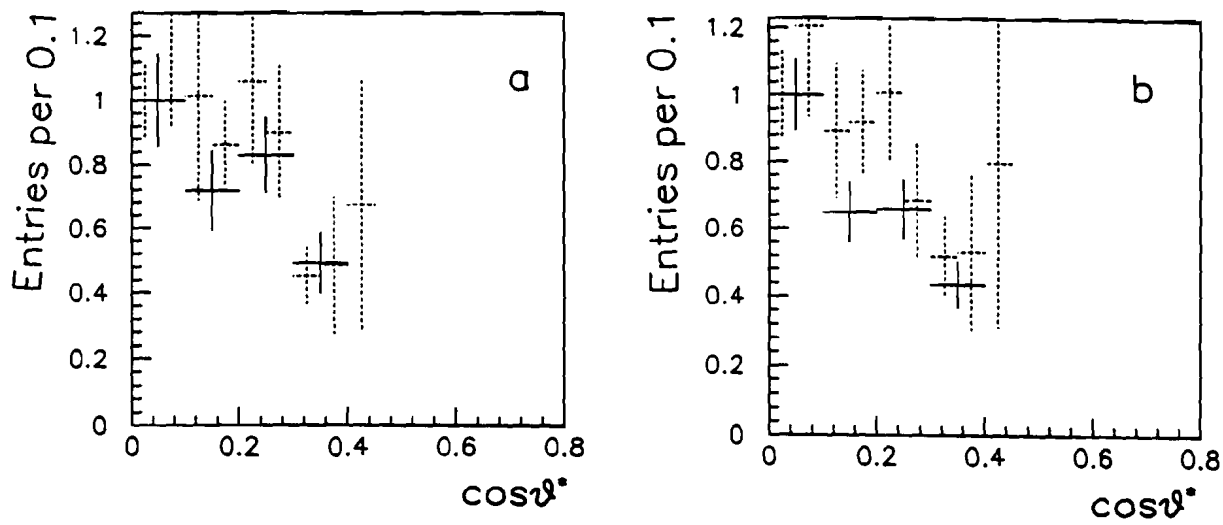


Figure 5.11: $\cos\theta^*$ Normalized to $\theta^* = 90^o$. (a) negative beam data and (b) positive beam data. The experimental data are indicated by the solid lines and the QCD predictions are shown with the dotted lines. Both the data and the QCD prediction have been subject to the same cuts.

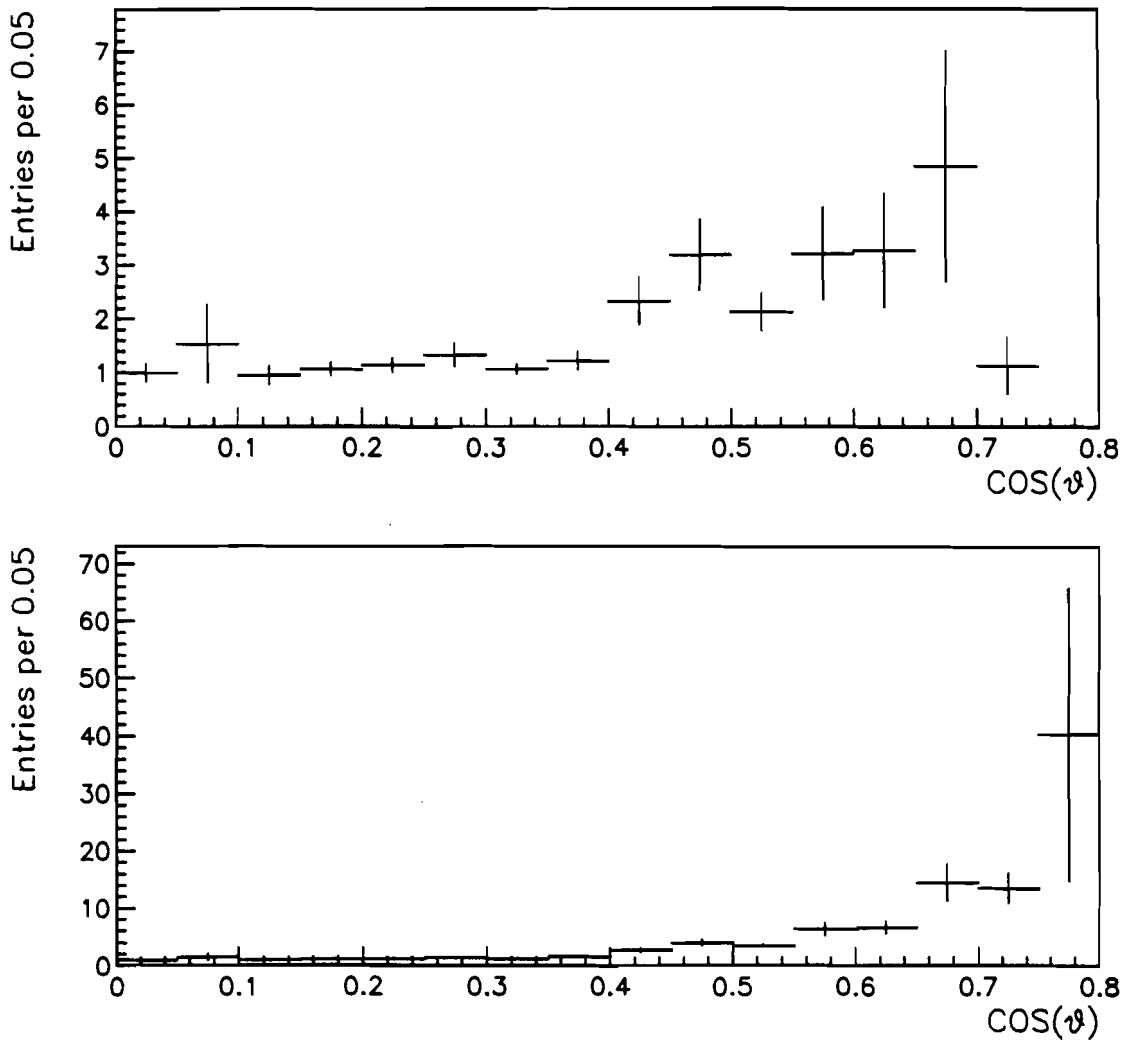


Figure 5.12: QCD $\cos\theta^*$ in Expanded $\pi^o$ Rapidity Range. (a) $|Y(\pi^o)| \leq 1.0$, (b) $|Y(\pi^o)| \leq 2.0$. Other than this, the cuts used in the QCD are identical to those used in Figure 5.11. The distributions have been normalized to $\theta^* = 90^o$

Kennard and Cooper [36] where we consider a beam of $N_B$ particles per second crossing an area $\Sigma$ in which there is a single target nucleus. Some number $i$, of the incident particles will interact with this target nucleus. The cross section for this process is defined as

$$\begin{aligned}\sigma &= \frac{number\ of\ interactions/target\ nucleus}{number\ of\ incident\ particles/unit\ area} \\ &= \frac{i}{N_B/\Sigma}.\end{aligned}$$

If a target contains n nuclei per unit area then

$$\sigma = \frac{i}{N_B}\frac{\Sigma}{n}$$

is the cross section per target nucleus. For a target of finite thickness, $L$, and containing $N$ nuclei per unit volume

$$\sigma = \frac{i}{N_B}\frac{1}{NL}.$$

The number of nuclei per unit volume is given by

$$N = \frac{N_A\rho}{A}$$

where $N_A$ is the Avogadro number (number of nuclei per mol), $\rho$ is the density of the target material ($gm/cm^3$) and $A$ is the atomic weight ($gm/mol$) of the target. Finally, we may write the cross section as

$$\sigma = \frac{i}{N_B}\frac{A}{N_A\rho L}.$$

In this thesis we will write the cross section in terms of the mass differential cross section per nucleon as

$$\frac{d\sigma}{dM} = \frac{1}{\Delta M}\frac{i}{N_B}\frac{C}{N_A \rho L} \tag{5.8}$$

where $i$ is now the number of interactions within the interval $\Delta M$ and we have introduced the factor, $C$, which represents all the corrections applied to the data.

For the analysis in this thesis the following cuts, applied to the $\pi^0$ pair system, will be implicit in the results except when stated otherwise:

- $-0.3 \leq Y \leq 0.7$
- $|\cos\theta^*| \leq 0.4$
- $p_T \leq 3.0$ GeV.

### 5.3.5 Corrections to the Data

The corrections applied to the data to account for the turn-on threshold for the TWO-GAMMA trigger were discussed in Section 3.4.2. In Section 3.4.3 we covered TWO-GAMMA trigger acceptance issues. In this section, we will discuss the acceptance for our detector to observe $\pi^0$ pair events.

We calculate the acceptance for the $\pi^0$ pair event topology in our detector using the data in the following scheme. For each event which was fully reconstructed, we generate one thousand new events, each of which has been rotated in a uniformly random azimuthal orientation in the range

$0 \leq \phi < 2\pi$. Each new $\pi^o$ pair is allowed to decay into photons with asymmetry in the range $0 < A \leq 0.75$. Photon energies and positions at the EMLAC are calculated. Two questions are asked: Does the pair of photons from each $\pi^o$ fall within a single octant? Do all four photons fall within the fiducial regions of the EMLAC? For each generated event for which the answers to both questions is positive, the numerator is incremented. The acceptance for the original event is defined as this numerator divided by one thousand.

Since the target consists of about 10% of a radiation length, some of the $\pi^o$ photons convert and the event is never observed. This is corrected for on an event-by-event basis and depends on the Z-position of the reconstructed vertex. The amount of target material which the four photons traverse is calculated and the probability that a single $\gamma$ does not convert is given by

$$P_\gamma(NC) = e^{-7X/9} \tag{5.9}$$

where x is the amount of target material downstream of the vertex in units of radiation lengths. The probability that none of the $\pi^o$ $\gamma$'s convert is given as $(P_\gamma(NC))^4$.

The efficiency for reconstructing a $\pi^o$ as a function of $p_T$ and rapidity was taken from Lanaro [25]. This was determined using Monte Carlo events with single $\pi^o$s and the scheme is fully described in this reference.

The $\gamma\gamma$ combinations we selected have an asymmetry in the range $0 < A \leq 0.75$. Since $\pi^o$s are produced with a flat asymmetry in this range, we

correct with the factor $16/9 = (1/0.75)^2$.

### 5.3.6 $\pi^o\pi^o$ Mass Spectra

We present in this section the mass dependence of the two processes: $\pi^- + Be \rightarrow \pi^o\pi^o + X$ and $p + Be \rightarrow \pi^o\pi^o + X$. The data are shown in Figures 5.13 and 5.14. The negative beam data extend out to higher masses than the positive beam data; we will discuss this in Section 5.3.7. In both plots, the data tend to flatten out at low mass. The minimum $p_T$ requirement ($p_T \geq 2$ GeV) placed on the single $\pi^o$s is responsible for this behavior. The vertical error bars indicate statistical errors only and the horizontal error bars indicate the mass bin. The horizontal position of the data point within a mass bin is the *center* not the *mean* of the bin.

Overlaying the data of Figures 5.13 and 5.14 we have included the QCD predictions of Owens [33] for this process at two values of $Q^2$ using the Set 2 fits to the structure and fragmentation functions. The choice $Q^2 = 2{p_T}^2$ seems to match our overall normalization best. With these parameters, the Monte Carlo approximates the data rather well over the entire mass spectra. Our decision to use the Set 2 fits to the structure and fragmentation functions in the QCD Monte Carlo is based on Figure 5.19 in Section 5.3.7.

We will now compare our data with that of the CCOR [4] group. Since this experiment was performed at the ISR, which consisted of intersecting beams of protons, we will compare their data with our positive beam results. In order to do this we have applied cuts to our data to match the CCOR

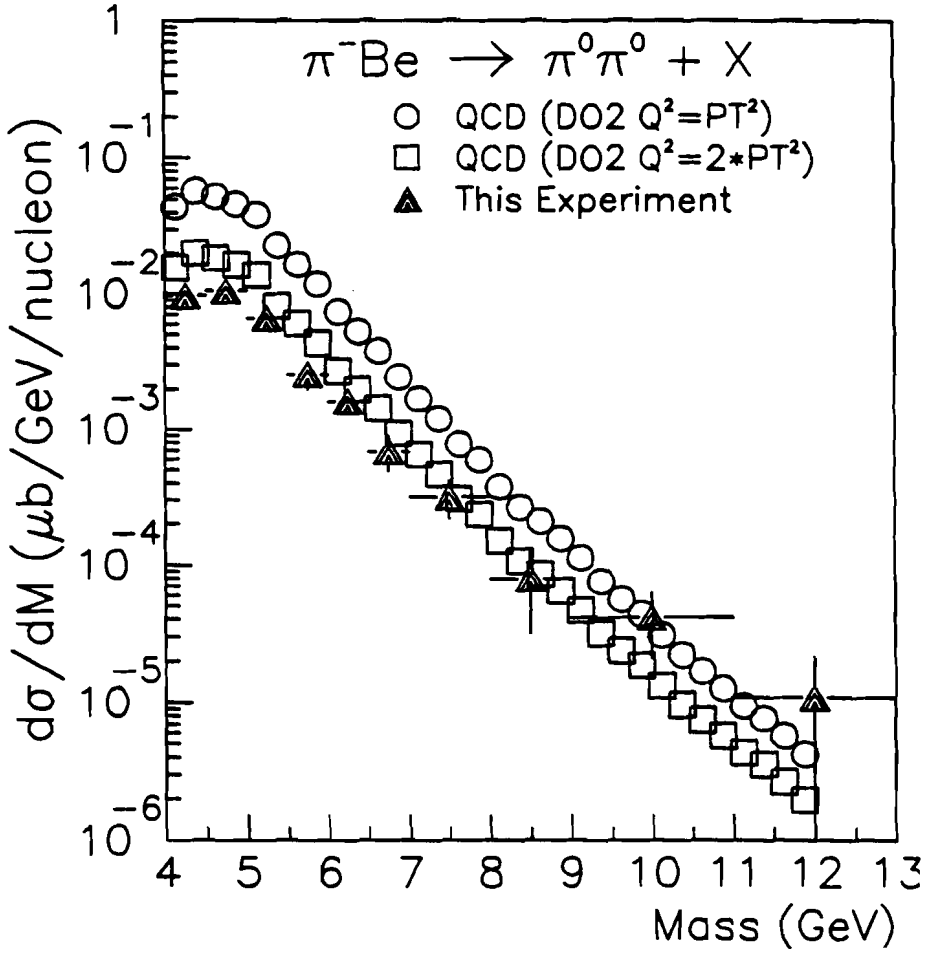


Figure 5.13: $\pi^o$ Pair Mass from the Negative Beam; the data compare well to the QCD leading log prediction. The same cuts were applied to both the QCD Monte Carlo and the data: $|\cos\theta^*| \leq 0.4$; $p_T(\pi^o\pi^o) \leq 3.0$ GeV; $-0.3 \leq Y(\pi^o\pi^o) \leq 0.7$

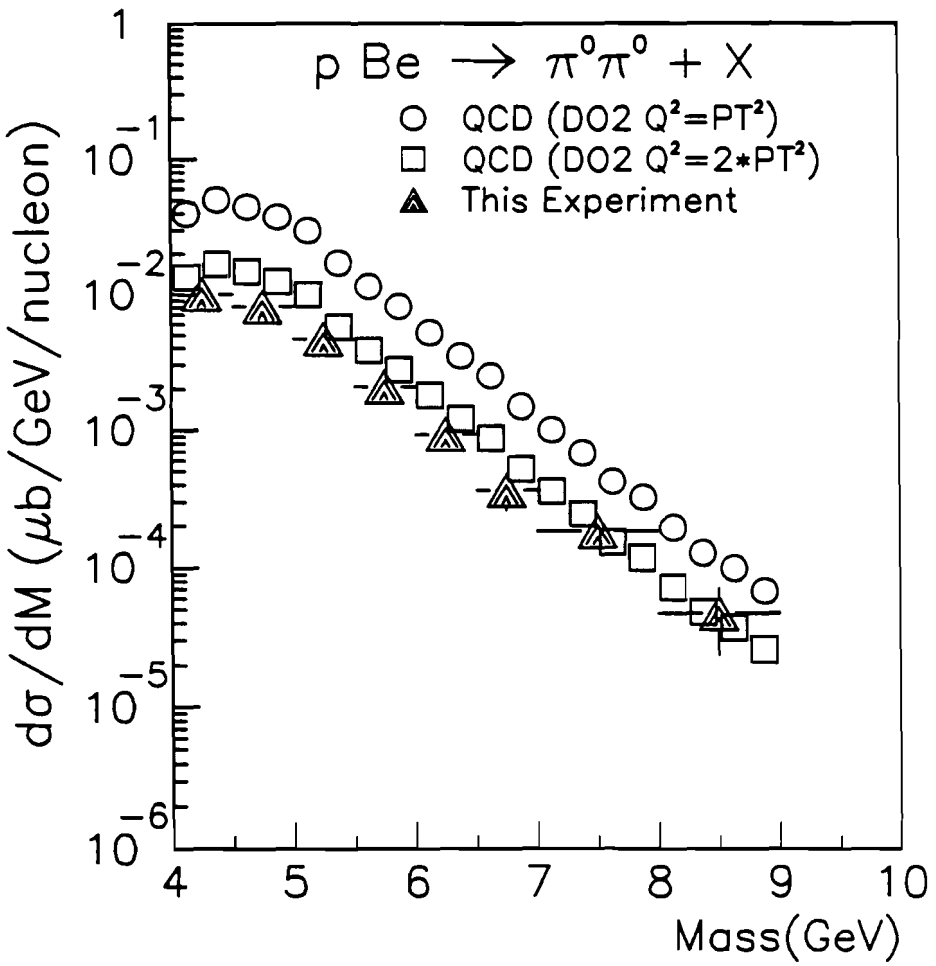


Figure 5.14: $\pi^o$ Pair Mass from the Positive Beam; the same cuts were applied to both the QCD Monte Carlo and the data: $|\cos\theta^*| \leq 0.4$; $p_T(\pi^o\pi^o) \leq 3.0$ GeV; $-0.3 \leq Y(\pi^o\pi^o) \leq 0.7$

cuts. The following cuts were applied to the $\pi^o$ pair:

- $|Y| \leq 0.3$
- $|cos\theta^*| \leq 0.4$
- $p_T \leq 1.0$ GeV.

Although the CCOR group actually cut their rapidity at $|Y| \leq 0.35$, we assume that the difference is small.

In Figure 5.15, we see the range in mass over which the restricted data set extends. Evident from this plot is the feature that as one increases in center of mass energy ($\sqrt{s}$), the cross section increases. The first data point in Figure 5.15 (from this experiment) is not very reliable as an indication of the trend of the spectrum at low mass since it is affected by the single $\pi^o$ $p_T$ cut. This behavior is also observed in Figures 5.13 and 5.14 where it is also reproduced in the Monte Carlo. Nonetheless, our mass spectrum appears roughly where one would expect it.

In Figure 5.16, we have plotted the QCD predictions for the CCOR data at $\sqrt{s} = 62$ GeV (subject to the above cuts) and for our $\sqrt{s} = 32$ GeV along with our experimental data. As with all Monte Carlo results presented here, we have used the Set 2 fits to the distribution and fragmentation functions. For the $Q^2$ definition we have used $Q^2 = 2{p_T}^2$.

When the data are presented in a scaled format (the mass is scaled such that $\tau \equiv M/\sqrt{s}$ and the cross section is redefined as $M^{6.5}\mathrm{d}\sigma/\mathrm{dM}$), as in Figure 5.17, we see that the CCOR data at the two different $\sqrt{s}$ values

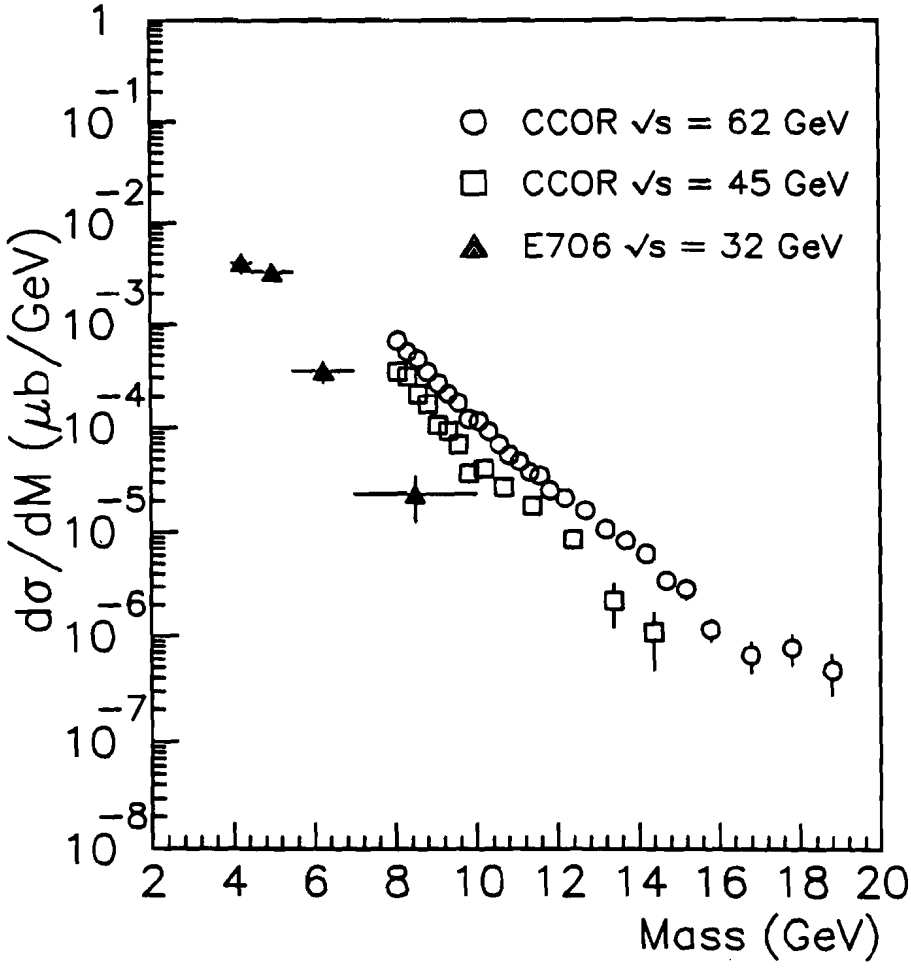


Figure 5.15: ISR and E706 $\pi^o\pi^o$ Mass Spectra; the same cuts were applied to all data: $|\cos\theta^*| \leq 0.4$; $p_T(\pi^o\pi^o) \leq 1.0$ GeV; $-0.3 \leq Y(\pi^o\pi^o) \leq 0.3$.

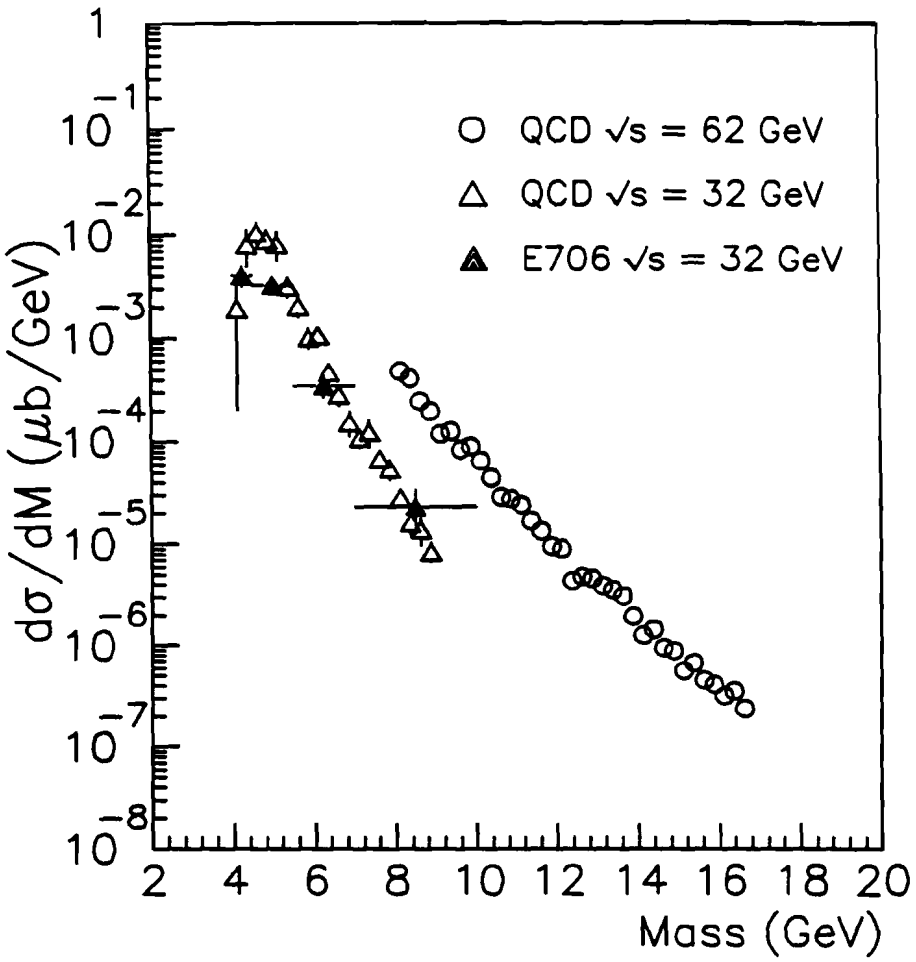


Figure 5.16: QCD Predictions for ISR and E706 Mass Spectra; the same cuts were applied to all data: $|\cos\theta^*| \leq 0.4$; $p_T(\pi^0\pi^0) \leq 1.0$ GeV; $-0.3 \leq Y(\pi^0\pi^0) \leq 0.3$.

overlap, that is these data *scale* while our data lie well below the CCOR data. The value of 6.5 for the power of the mass was determined by the CCOR group to provide the best scaling agreement with their data. The disagreement between our data and the CCOR data may be one of two things: 1) either the data do not scale or 2) there is some cut implicit to one set of data which we have not accounted for. We believe that the data do scale and that we have, in fact, not matched our cuts to the CCOR cuts.

We will support this line of reasoning by using the Owens' QCD Monte Carlo to calculate the cross sections using the cuts described above at the two $\sqrt{s}$ energies and test for scaling. We see in Figure 5.18 that the QCD data scale as suggested by the CCOR group. Furthermore, we see that our data agree rather well with the scaled QCD predictions.

Previous work [25] done with single $\pi^o$ production in this experiment has included an extensive study of systematic errors. We suggest that the problems with systematic uncertainties are at the same level for this study as for that work, in particular, about 20%.

### 5.3.7 Beam Ratio

In this section we will avoid problems with systematic errors in the data by presenting the mass spectra in the form of a beam ratio of the $\pi^o$ pair production cross sections. In addition to avoiding problems with systematics, beam ratios provide a useful scheme through which the structure of the beam particles may be investigated. Futhermore, since different $Q^2$ definitions primarily affect the overall normalization, uncertainties in the Monte

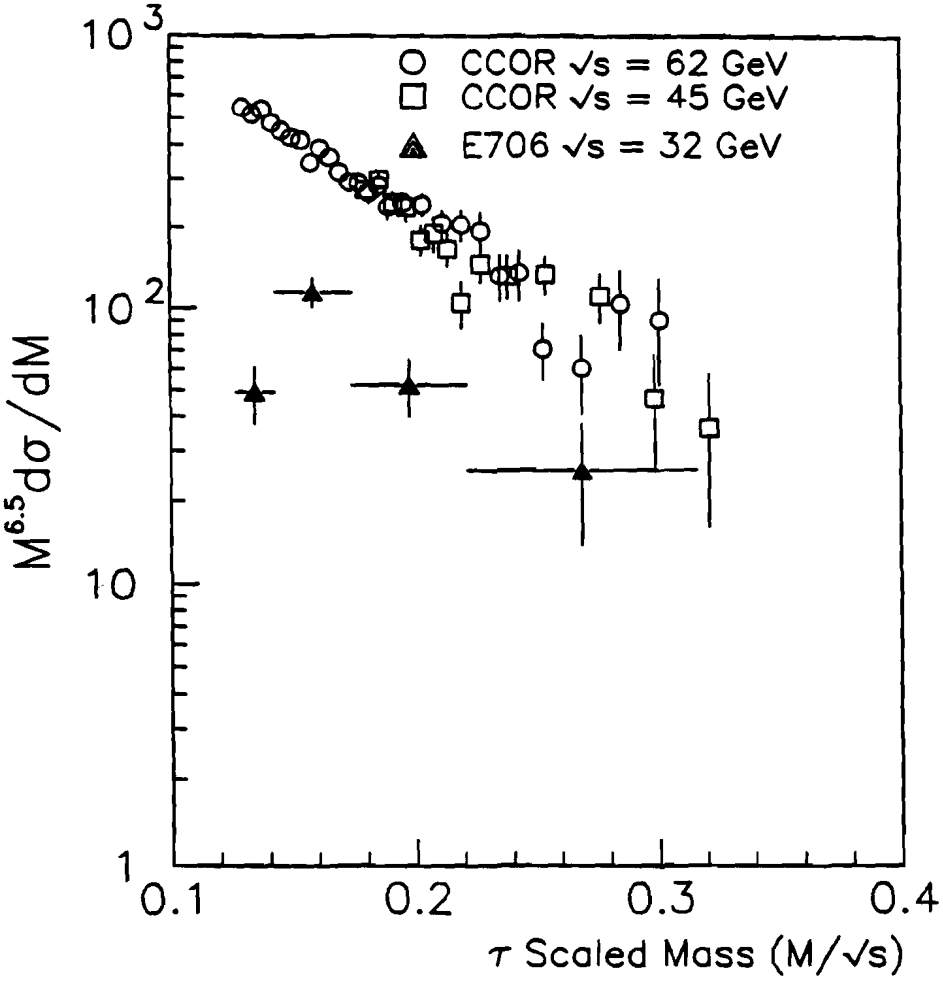


Figure 5.17: $\pi^0$ Pair Scaled Mass. Data are from this experiment and from the CCOR Collaboration [4].

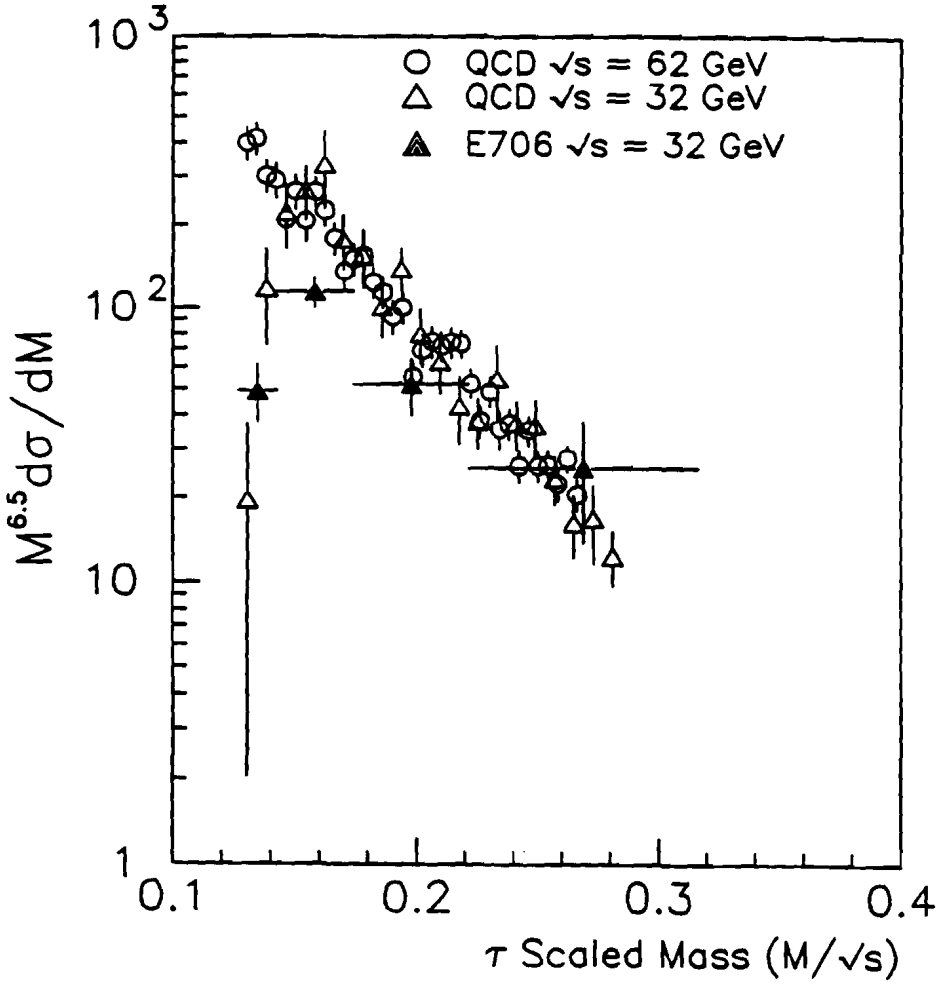


Figure 5.18: QCD Scaled Mass Spectra at ISR and E706 Energies.

Carlo are also reduced.

Figure 5.19 shows the ratio of $\pi^0$ pairs produced (as a function of mass) from the two beams in this experiment. In addition to the experimental data, we have included the predictions as calculated with Owens' QCD Monte Carlo for the two $\Lambda$ values in Sets 1 ($\Lambda$ = 200 MeV) and 2 ($\Lambda$ = 400 MeV). Although the fit to the data is consistent with both Set 1 and 2 (see Table 5.3), one may argue that there is preference for Set 2. For simplicity, we will restrict the Monte Carlo predictions to those using the Set 2 fits to the distribution functions.

Table 5.3: Beam Ratio Fit Parameters; the fits are plotted in Figure 5.19.

| | Slope | Intercept |
|---|---|---|
| Data | $0.27 \pm 0.13$ | $-0.12 \pm 0.63$ |
| MC Set 1 | $0.27 \pm 0.02$ | $0.15 \pm 0.15$ |
| MC Set 2 | $0.23 \pm 0.02$ | $0.04 \pm 0.13$ |

Clearly, the data and the Monte Carlo results in this plot tend to increase with mass; the slope is not consistent with zero. We will argue that this increase with mass is due to the following:

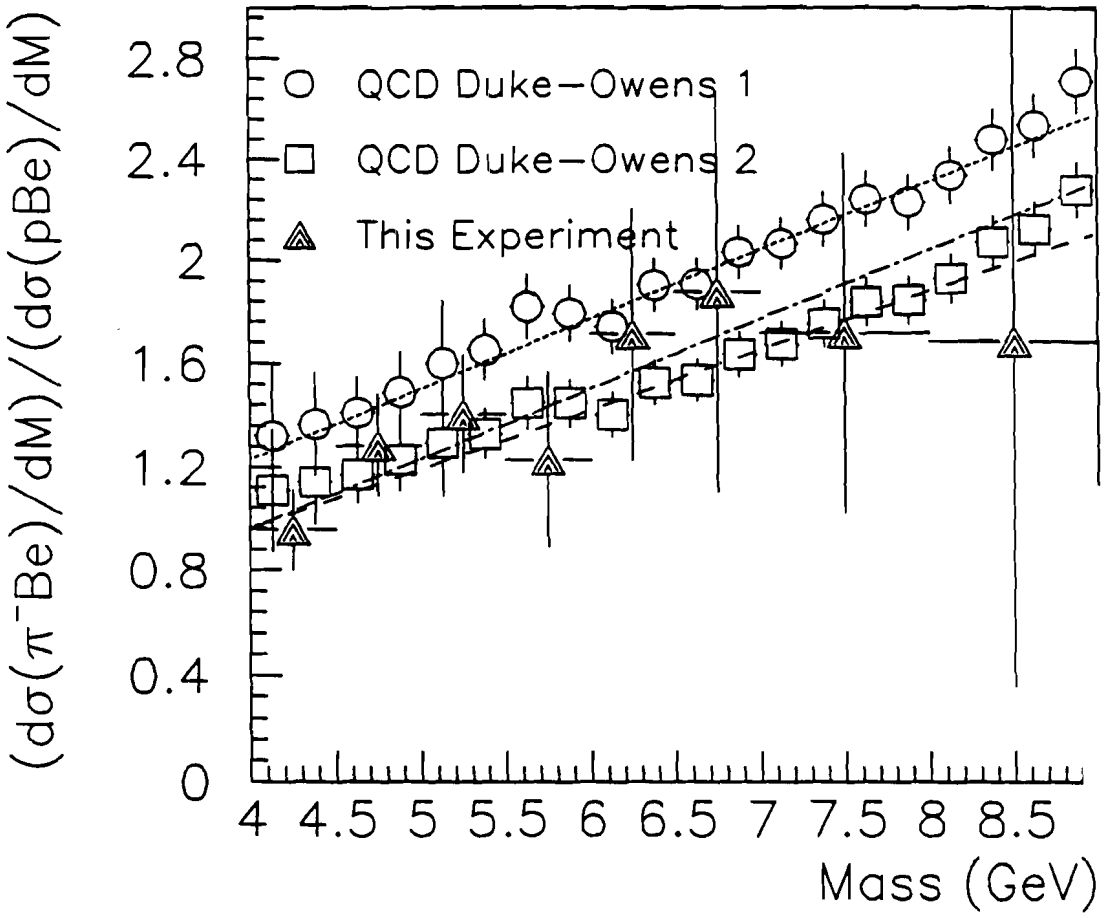


Figure 5.19: Cross Section Beam Ratio. The triangular points were generated with the QCD Monte Carlo described in Section 1.2. The upward pointing triangles correspond to Set 1 ($\Lambda$ = 200 MeV) while the downward pointing triangles correspond to Set 2 ($\Lambda$ = 400 MeV). The circles are data from this experiment. The lines are fits to each set of points; the fit parameters are given in Table 5.3.

- high mass $\pi^o$ pairs tend to be produced by high-$x$ partons,
- the partons within the pion tend to have a larger fraction of the momentum than do the partons within the nucleon,
- the beam partons tend to be gluons.

For jets produced with equal $p_T$ the expression for the fraction of momentum carried by the incident (beam) constituent parton is [33]:

$$x_a = p_T(e^{Y1} + e^{Y2})/\sqrt{s} \tag{5.10}$$

where $Y1$ and $Y2$ are the center of mass rapidities of the jets. We have argued that our triggered $\pi^o$s arise from the hard interaction with a large fraction of the scattered parton momenta (see Figure 5.8). Given this, we can use Equation 5.10 to approximate a distribution in $x$ for the pion and nucleon beams. The form of Equation 5.10 displays an explicit dependence on transverse momentum: $x$ increases with $p_T$. Since the mass of the $\pi^o$ pair system is closely related to $p_T$, we may also infer that $x$ increases with mass; interactions involving high $x$ partons result in high mass $\pi^o$ pairs.

We may demonstrate this from our data using Equation 5.10. In Figure 5.20 we have plotted the mean value of $x$ (within a bin) versus mass. It is clear that high $x$ interactions correspond to high mass $\pi^o$ pairs. In the calculation for $x$, we have used the highest $p_T$ of the pair and $Y1$ and $Y2$ are those as measured for the $\pi^o$s. Also, Figure 5.20 shows the data for the $\pi^-$ beam; the proton beam data are quite similar. Furthermore, it should

be emphasized that the relationship between $x$ and mass is not one-to-one. The distribution of $x$ within a mass bin is rather wide. In Figure 5.20 we have plotted the *mean* values of rather broad distributions with the intention of displaying the *tendency* of high $x$ constituent interactions to induce high mass hadron pairs.

The raw $x$ distributions using Equation 5.10 for both beams are shown in Figure 5.21a and b. Since we have no way to separate the quark distribution from the gluon distribution, Figure 5.21 represents an average of the beam parton distributions. The points with solid-lined error bars are the experimental data and the points with dashed errors are from the Monte Carlo. The data have been normalized to the number of beam particles and all known corrections have been applied. The cuts to the data and the Monte Carlo are identical. For the Monte Carlo, we have used the Set 2 fits to the structure and fragmentation functions and $Q^2 = {p_T}^2$. The agreement is very good.

Having established that the high-$x$ interactions tend to induce high mass $\pi^0$ pairs, we now turn to Figure 5.22 where we have plotted the ratio of the pion and nucleon distribution functions (from Figures 1.5 and 1.6) for both gluons and valence quarks. The gluon distribution ratio, Figure 5.22a, begins at about unity and steadily increases with $x$. This implies that the pion gluons are as likely to be involved in interactions as nucleon gluons at low $x$ and more likely at high $x$. The valence quark ratio, Figure 5.22b, begins at around 0.3 and and does not reach one until $x \simeq 0.6$. This implies that, at low $x$, the nucleon valence quarks are more likely to participate in

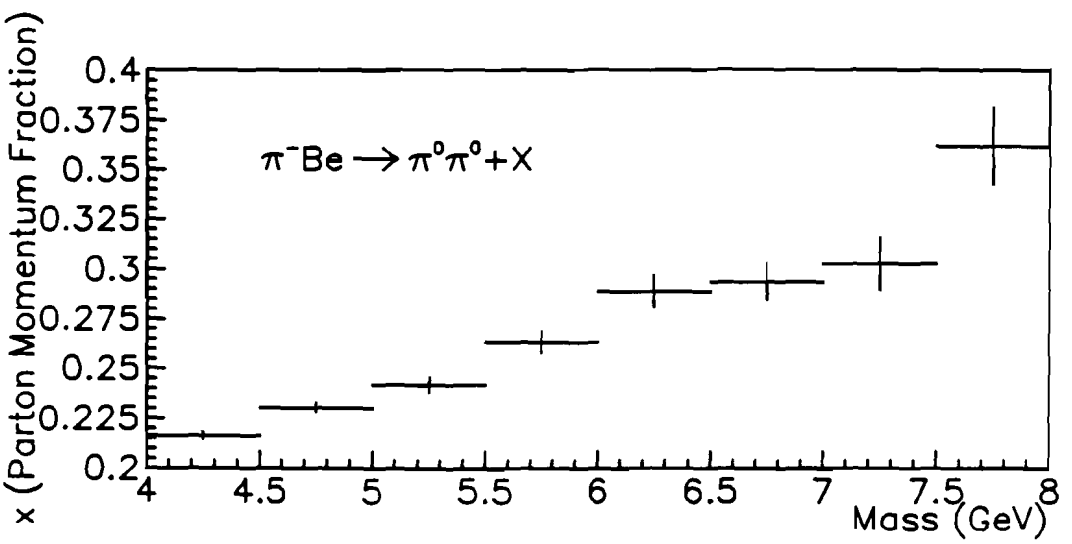


Figure 5.20: Beam $x$ vs Mass. The mass of the $\pi^0$ pair system increases with the beam parton momentum fraction. Shown is the pion beam data; the proton beam data are very similar.

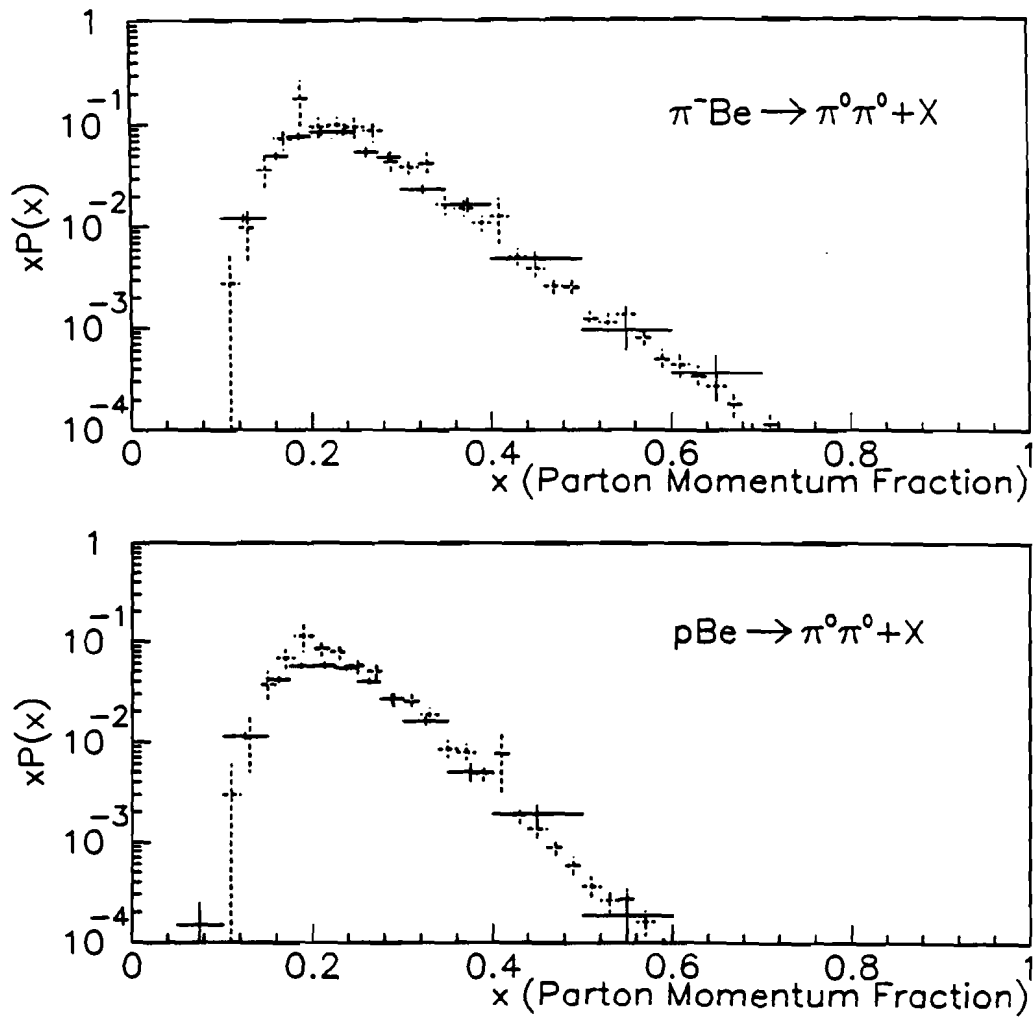


Figure 5.21: Beam $x$-Distributions; the points with solid error bars are the data from this experiment as calculated with Equation 5.10 and the points with dashed error bars are from the Monte Carlo.

interactions than their pion counterparts.

From Figure 5.21, we see that this experiment is sensitive to $x$-values in the range $x \simeq 0.1 - 0.6$. The slopes of the parton $x$-distributions as measured in the data and in the Monte Carlo (Figure 5.21) are substantially steeper than the gluon distributions of Figure 1.5. One explanation for this may be due to how we use Equation 5.10 to estimate the parton momentum fraction. This equation assumes that the quantities used in its calculation are well known from fully reconstructed jets. In the case at hand, our $\pi^o$ 4-vectors are somewhat removed from the jet 4-vectors, being products of the fragmentation. Since $x$ is proportional to $p_T$, and we have underestimated the jet $p_T$, we have underestimated $x$. Since the distribution is rather steeply falling, we will artificially enhance (a situation referred to as *slewing*) the steepness of the distribution. The shape of the distribution is faithfully reproduced by the Monte Carlo.

Another way of looking at the evidence for beam gluons is yet another ratio plot. Given that the slewing effect is systematic, we may be able to cancel it out by taking the beam ratio of our measured parton distributions. Having normalized each distribution in Figure 5.21 to the number of beam particles, we may look at more than just the shape of the plot. This ratio of measured distributions is shown in Figure 5.23. We have overlaid the $Q^2$ =100 GeV$^2$ distribution function ratios from Figure 5.22. These data support the previous suggestion that gluons dominate the production of $\pi^o$ pairs in this experiment.

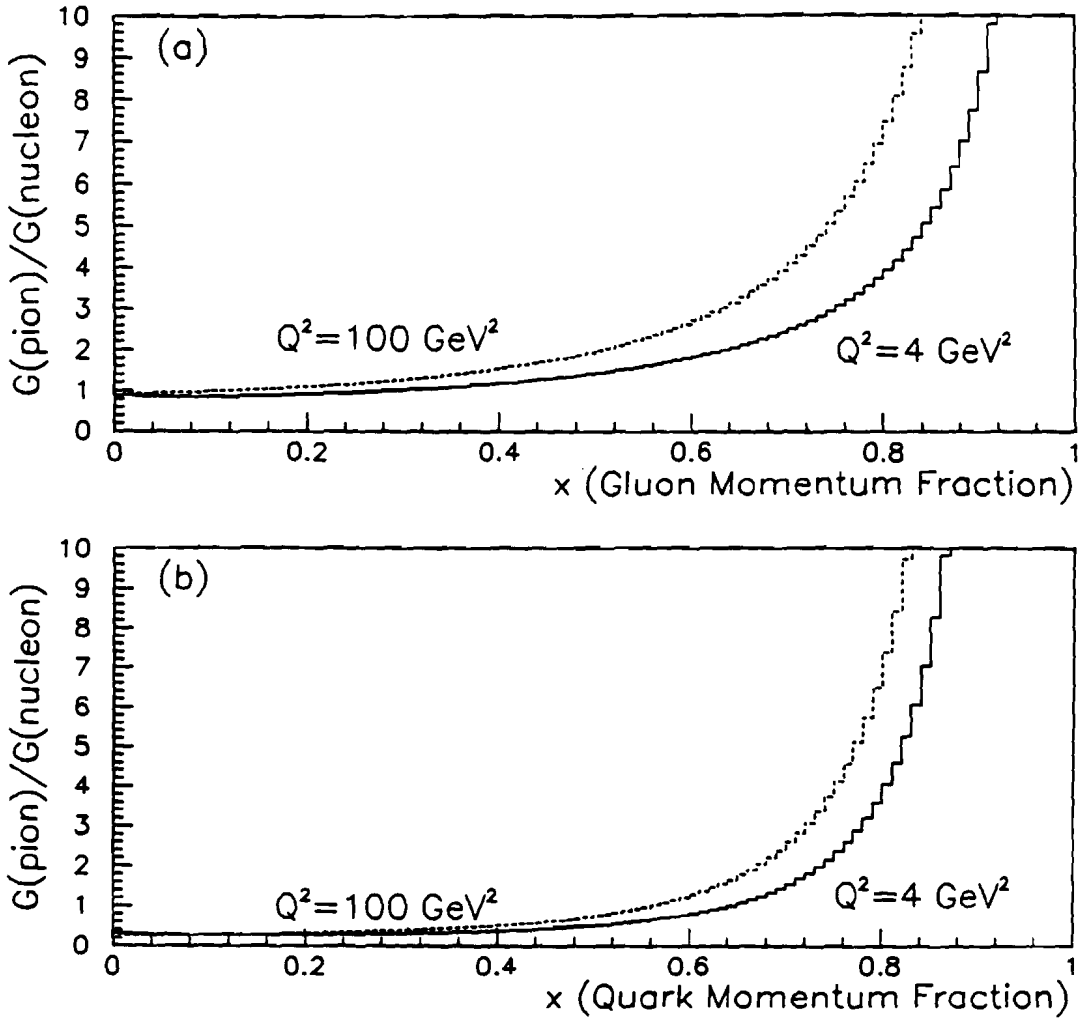


Figure 5.22: Distribution Function Ratios. The ratio of pion and nucleon distribution functions used in the QCD Monte Carlo calculated at two values of $Q^2$ (roughly corresponding to the range accessible in this experiment). (a) for gluons and (b) valence quarks.

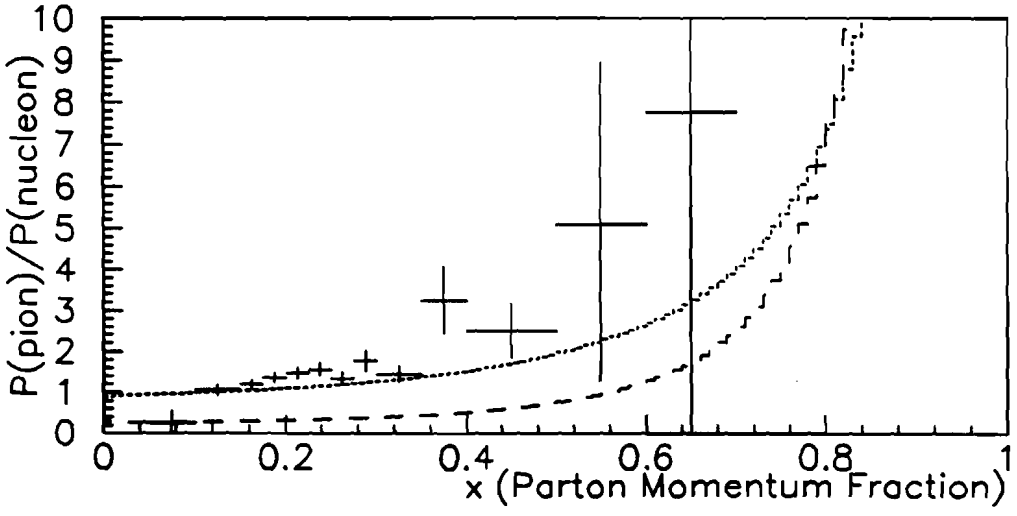


Figure 5.23: Beam $x$–Distribution Ratio. As a ratio of measured pion and nucleon parton distributions, we expect this to be some combination of the distribution function ratios of Figure 5.22. We have overlaid the gluon and valence quark ratios at $Q^2$ =100 GeV$^2$.

## 5.4 Conclusions

In studying the azimuthal and rapidity distributions of charged particles produced in association with $\pi^o$ pairs, we have shown evidence for a jet-like structure in these events. The charged particles tend to be produced in the same directions both azimuthally and longitudinally as the $\pi^o$s. Using a very simple jet algorithm, it was observed that the $\pi^o$s carry about 90% of the jet transverse momentum at the highest $p_T$. From a parton model viewpoint, we are able to conclude that the $\pi^o$s carry a large fraction of the scattered parton momentum.

Measurements of the inclusive hadronic production of $\pi^o$ pairs from $\pi^-$ and proton beams with a Beryillium target were made. A cross section differential in mass was defined and comparisons were made with the results of the CCOR [4] group and with a QCD Monte Carlo [33]. In both cases, good agreement was observed, and it was concluded that our data scale with higher energy data according to the CCOR prescription.

Finally, a ratio was made of the production of $\pi^o$ pairs from the $\pi^-$ and proton beams. This ratio was observed to increase with the mass of the $\pi^o$ pair system: $\pi^-$ beams produce more $\pi^o$ pairs at high mass than proton beams. Furthermore, the beam ratio suggests that the data prefer the Duke-Owens Set 2 [15]) fits to the structure and fragmentation functions. With a definition for $x_a$, the fraction of beam hadron momentum carried by the interacting parton, it was observed that the mass of the $\pi^o$ pair system increased with $x_a$. Intuitively, one expects this from the harder parton

distributions in the pions as compared with nucleons.

In summary, the data on symmetrically produced $\pi^0$ pairs (and associated charged particles) in $\pi^-$Be and $p$Be interactions agree rather well with the QCD picture of parton-parton collisions. Detailed comparisons with the QCD calculations of Owens are in excellent agreement and suggest that these events are induced by gluons in the beam hadrons.

## References and Notes


[1] Abe, F., *et al.*, *Phys. Rev. Lett.*, 1988, **61** 1819.

[2] Altarelli, G., and G. Parisi, 1977, *Nucl. Phys.*, **B126** 298.

[3] Alverson, G. O. and Pothier, E. L., E706 Software Note, **E706–0139**.

[4] Angelis, A. L. S., *et al.* 1982, *Nucl. Phys.*, **B209** 284.

[5] The Fermilab Advanced Computer Project consisted of a number of parallel processing hardware nodes with supporting software. E706 ran the reconstruction program MAGIC on an ACP multiprocessor systems with up to 68 nodes for three months. Details of this system may be found in the Fermilab Computing Department Notes #GA0001–GA0004.

[6] Baier, R., J. Engels and B. Peterson, 1979, *Z. Physik C*, Particles and Fields, **2** 265.

[7] Baker, W.F., *et al.*, 1988, Proceedings of the XXIV International Conference on High Energy Physics, Munich, Germany.

[8] Baker, W.F., *et al.*, 1981, Proposal to Measure Direct Photon Production at Tevatron Energies, E706 Fermilab Proposal.

[9] Balocchi, Giuseppe, 1989, *unpublished*, Ph.D. Thesis, University of Rochester, Rochester, New York;

[10] Benson, Richard, 1989, *unpublished*, Ph.D. Thesis, University of Minnesota, Minneapolis, Minnesota.

[11] Bonvin, E., *et al.*, 1990, WA–70 Collaboration, Phys. Lett. **B236**, 523, 1990.

[12] Brun, R., *et al.*, 1988, ZEBRA, A Fortran Based Dynamic Memory Management System, CERN write–up **Q100**, Geveva, Switzerland or Fermilab Software note **PU0046**, Fermilab, Batavia, Illinois.

[13] Brun, R., *et al.*, 1984, GEANT3 User's Guide, CERN DD/EE/84–1, Geneva, Switzerland, or Fermilab Software Note PM0062, Fermilab, Batavia, Illinois.

[14] Chadha S., C. Lam, and Y. Leung 1974, *Phys. Rev.*, **D10** 2917.

[15] Duke, D.W., and J. F. Owens, 1984, *Phys. Rev.* , **D30** 49.

[16] Easo, Sajan, 1989, Ph.D. Thesis, Penn State University, University Park, Pennsylvania.

[17] Fabjan, C., 1987, in Experimental Techniques in High Energy Physics, Thomas Ferbel, editor, Addison Wesley.

[18] Giacomelli, G., and Jacob, M., 1979, *Phys. Rep.*, **55C**, 1.

[19] Hossain, Sahadot, 1985, E706 Software Note **E706–011**.

[20] Kapoor, Vijay, *private communication.*

[21] Kourbannis, Ionnis, 1990, *unpublished*, Ph.D. Thesis, Northeastern University, Boston, Massechusetts.

[22] Jöstlein, R. J., *et al.* 1979, *Phys. Rev. Lett.*, **42** 146.

[23] Kemmer, J., 1980, *Nucl. Inst. and Meth.*, **169** 499.

[24] Kourkoumelis, C., *et al.* 1980, *Phys. Rev. Lett.*, **45** 966.

[25] Larnaro, Armando, 1989, *unpublished*, Ph.D. Thesis, University of Rochester, New York.

[26] Lukens, Patrick., *private communcation.*

[27] Mani, Sudhindra, 1982, *unpublished*, Ph.D. Thesis, The University of Pittsburgh, Pittsburgh, Pennsylvania.

[28] Mansour, John, 1990, *unpublished*, Ph.D. Thesis, University of Rochester, Rochester, New York.

[29] Nanometric Systems, Inc., *unpublished* **Multi Wire Proportional Chamber Readout System** Oak Park, Illinois.

[30] Owens, J. F., 1978, *Phys. Lett.* , **76B** 75.

[31] Owens, J. F., 1979, *Phys. Rev.* , **D19** 3279.

[32] Owens, J. F., 1984, *Phys. Rev.* , **D30** 943.

[33] Owens, J. F., 1987, *Rev. Mod. Phys.*, **59** 465.

[34] Press, W. H., B. Flannery, S. Teukolsky and W. Vetterling 1986, *Numerical Recipes*, Cambridge University Press.

[35] PYTHIA, Event Generator.

[36] Richtmyer, F. K., E. H. Kennard and John N. Cooper, 1969, *Introduction to Modern Physics*, 6th Edition, McGraw–Hill, Inc.

[37] Ritson, David M., 1961, *Techniques of High Energy Physics*, Interscience Publishers, Inc.

[38] Rossi, *et al.*, 1975, *Nucl. Phys. B* **84** 269.

[39] Sauli, F., 1977, *Principles of Operation of Multiwire Proportional and Drift Chambers*, CERN **77-09**.

[40] Skow, Dane, 1990, *unpublished*, Ph.D. Thesis, University of Rochester, Rochester, New York.

[41] White, V., *et al.*, 1985, *The* VAXONLINE *System at Fermilab*, Fermilab Computing Department note **PN318** and Berman, E., *et al.*, 1985, VAXONLINE *User's Guide*, Fermilab Computing Department note **PN252**, Fermilab, Batavia, Illinois.

[42] Va'Vra, J., 1986, *Nucl. Inst. and Meth.*, **A252** 547-563.

[43] Weerasundara, Dhammika, *private communication.*

[44] Yosef, Carlos, 1990, *unpublished*, Ph.D. Thesis, Northeastern University, Boston, Massechusetts.

## Vita

The author was born on December 27, 1954 at St. Joseph's Hospital, in Flint, Michigan. After a rather pleasant childhood, he graduated from Davison High School in 1973 with no particularly honorable distinctions. After high school, the author proceeded to sample the job market. A short summary of his employment record follows: Bouncer at the Sand Trap Lounge in Flint; Insurance Investigator in Flint; Worker at the Athenian Marble (Don't Take Us for Granite) Factory in Flint; Gardener at the Grand Hotel on Mackinac Island, Michigan; Wheel Painter and Tire Hanger at Buick Motor Division in Flint; Machine Repair Apprentice, also at Buick.

After a short period of time spent traveling in Europe and Africa, the author began attending classes at the C. S. Mott Community College in Flint. Some time later he declared himself a physics major at the University of Michigan at Flint, graduating in December of 1981. The next year was spent working at Argonne National Laboratory with John Miller. In the summer of 1983, the author put his high school drafting experience to use making drawings for the E706 multiwire proportional chambers. In the autumn of that year, he was enrolled in the graduate physics program at Penn State. After a semester of teaching undergraduate physics he joined the high energy group and he began building the chambers as a research assistant under the guidance of Jim Whitmore. In early 1986, the author arrived at Fermilab to begin preparations for the 1988 Fixed Target run.

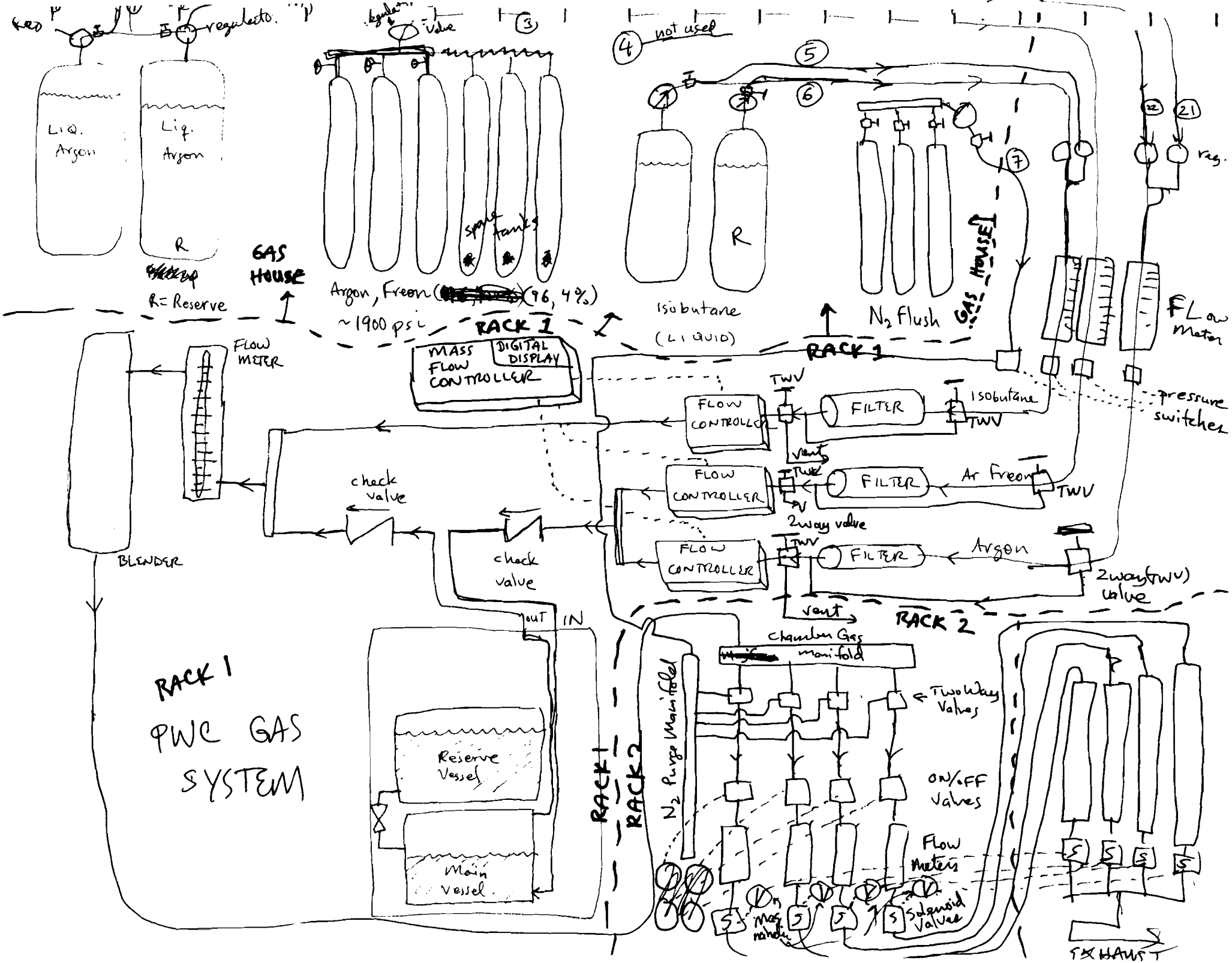
regulator
valve
not used
LIQ. Argon
Liq. Argon
R
R= Reserve
GAS HOUSE
Argon, Freon (96, 4%)
~1900 psi
spare tanks
RACK 1
MASS FLOW CONTROLLER
DIGITAL DISPLAY
FLOW METER
BLENDER
check valve
check valve
OUT
IN
Reserve Vessel
Main Vessel
RACK 1
PWC GAS SYSTEM
RACK 1
RACK 2
isobutane (LIQUID)
R
N2 Flush
GAS HOUSE
RACK 1
FLOW CONTROLLER
FLOW CONTROLLER
FLOW CONTROLLER
TWV
FILTER
isobutane
TWV
vent
TWV
FILTER
Ar Freon
TWV
2way valve
TWV
FILTER
Argon
2way(TWV) valve
vent
RACK 2
Chamber Gas manifold
Two Way Valves
ON/OFF Valves
Flow meters
Solenoid Valve
N2 Purge Manifold
Flow Meter
pressure switches
reg.
EXHAUST

$0.04 \times 60 = 0.4 \times 6 = 2.4$ l/hr

0.04 l/min

50 psi ≃ 120 l

$$\frac{2000\,psi}{50} \times 40 \times 50\,hr = \frac{2000\,hr}{24 \times 2} = 80 \text{ days}$$